Dissertation

submitted to the
Combined Faculties for the Natural Sciences and for Mathematics
of the Ruperto-Carola University of Heidelberg, Germany
for the degree of
Doctor of Natural Sciences

Put forward by
Steffen Joachim Sahl, BA MA MSci
born in Aalen (Württ.)

Oral examination: November 24th, 2010

Detection of fast-diffusing molecules in the membrane of living cells

Referees: Prof. Dr. Dr. h.c. Stefan W. Hell
Prof. Dr. Dirk Dubbers

Abstract

We present a novel optical scheme for the observation of the dynamics of single fluorescent molecules, with a flexible choice of high spatial localization accuracy (∼10–20 nm standard deviation or ∼20–40 nm full-width-at-half-maximum) and temporal resolution (<1 ms, <0.5 ms for much of a molecule trajectory). The fluorescence signal during individual passages of fluorescent molecules through a spot of excitation light allows the sequential localization and thus spatio-temporal tracking of the molecule if its fluorescence is collected on at least three separate point detectors arranged in close proximity. Time-correlated-single-photon-counting is shown to be a vital feature within this approach, allowing useful extensions in the analysis and improving signal-to-noise ratio in molecular tracking data. We show two-dimensional trajectories of individual, small organic dye labeled lipids diffusing in the plasma membrane of living cells and directly observe transient events of trapping on <20 nm spatial scales. The trapping is cholesterol-assisted and much more pronounced for a sphingo- than for a phosphoglycero-lipid, with average trapping times of ∼15 ms and <4 ms, respectively. The results support previous STED nanoscopy measurements and suggest that, at least for nontreated cells, the transient interaction of a single lipid is confined to macromolecular dimensions. Our experimental approach demonstrates that molecular movements up to diffusion coefficients $D \approx 0.1 - 1\,\mu\mathrm{m}^2/\mathrm{s}$ can be tracked with minimal invasion, which can reveal new important details of cellular nano-organization. This is further exemplified by uncovering subtle differences in the lateral diffusion of several membrane constituents of different chemical structure. The potential of single photon detection and counting for the rapidly developing field of far-field optical nanoscopy is discussed and proof-of-principle experiments are presented in which nanoscale images are reconstructed from molecular registrations based on their complete photon statistics.

Zusammenfassung

Eine neue optische Methode zur Beobachtung von Dynamiken einzelner fluoreszenter Moleküle wird vorgestellt. Der Ansatz erlaubt eine hohe Flexibilität zwischen räumlicher Lokalisierungsgenauigkeit (∼10–20 nm radiale Standardabweichung oder ∼20–40 nm Halbwertsbreite) und zeitlicher Auflösung (<1 ms, <0.5 ms für einen großen Teil einer Molekültrajektorie). Das Fluoreszenzsignal während einzelner Durchtritte von fluoreszierenden Molekülen durch einen Fokus von Anregungslicht erlaubt die sequenzielle Lokalisierung und damit das Verfolgen des jeweils einzelnen Moleküls in Raum und Zeit, wenn das Fluoreszenzlicht auf mindestens drei getrennten, jedoch nahe beieinanderliegenden, Punktdetektoren gesammelt wird. Die zeitkorrelierte Einzelphotonenzählung wird als ein zentrales Mittel in dieser Methode ausgemacht: ihr Einsatz erlaubt nützliche Erweiterungen in der Analyse und verbessert das Signal-zu-Rausch-Verhältnis in den molekularen Trajektoriendaten. Wir zeigen zwei-dimensionale Trajektorien von einzelnen mit kleinem organischen Farbstoff markierten Lipiden, die in der Plasmamembran lebender Zellen diffundieren. Hierbei beobachten wir direkt den Einfluss von transientem Verweilen der Lipide auf Längenskalen <20 nm. Dieses 'Trapping' ist cholesterolabhängig und für ein Sphingolipid viel markanter ausgeprägt als für ein Phosphoglycerolipid, mit mittleren Trapzeiten von ∼15 ms bzw. <4ms. Die Ergebnisse stimmen mit früheren Beobachtungen mittels STED-Nanoskopie überein und legen den Schluss nahe, dass die transiente Wechselwirkung eines einzelnen Lipids — zumindest in unbehandelten Zellmembranen — auf einen Bereich makromolekularer Größe begrenzt ist. Unser experimenteller Ansatz zeigt, dass es möglich ist, schnelle Molekülbewegungen ($D \approx 0.1 - 1\,\mu\mathrm{m}^2/\mathrm{s}$) minimalinvasiv zu verfolgen. Dies kann wichtige neue Details zellulärer Nanoorganisation sichtbar machen. Als wichtige Belege dafür werden Details des sich unterscheidenden Diffusionsverhaltens von Membranmolekülen unterschiedlicher chemischer Struktur aufgezeigt. Das Potenzial der Einzelphotonenzählung für die sich rapide entwickelnde fernfeldoptische Nanoskopie wird diskutiert. Wir präsentieren in diesem Zusammenhang Experimente, in denen Bilder mit Nanometerauflösung aus der Detektion einzelner Moleküle anhand ihrer vollständigen Photonenstatistik rekonstruiert werden.

Abbreviations

4Pi-microscopy	microscopy using two opposing lenses in a coherent way
2D	two-dimensional
Abs	absorption
cw	continuous wave
Det	detection
Eff	effective
Em	emission
Exc	excitation
FCS	fluorescence correlation spectroscopy
FRAP	fluorescence recovery after photobleaching
FWHM	full-width-at-half-maximum
GSD	ground state depletion
GSDIM	ground state depletion and individual molecule return
MLE	maximum likelihood estimation
MSD	mean-square displacement
NA	numerical aperture of a lens (NA$= n \sin \alpha$)
PDSD	probability distribution of square displacements
PSF	point spread function
RESOLFT	reversible saturable optical (fluorescence) transitions
SNR	signal-to-noise ratio
STED	stimulated emission depletion
TCSPC	time-correlated single photon counting
UV	ultraviolet (light)

Contents

Chapter 1

Introduction

The 21st century promises a major expansion at the interface of physics and the life sciences. This will comprise all aspects of the scientific endeavor and include model building, theoretical treatment and testing by simulation, but certainly, and as a starting point: careful measurement and observation. While there are still huge gaps in understanding at the systems level ("how does it all play together?"), progress in the study of the 'parts' has triggered new insight. New strategies for the direct investigation of the molecules of life have challenged long-held beliefs of what level of detail might be accessible to observation. They reveal just how much "room" there really is "at the bottom" (Feynman) [1], offering unprecedented insights into structure and function at smaller and smaller levels of organisation. Technological advances promote progress across many newly formed research fields – across the traditional boundaries of physics, chemistry, biology, medicine and new ones, such as nanotechnology – through, for example, the development of suitable light sources and more sensitive detection elements, tags of higher photostability and brightness for labeling molecules of interest, to name but a few directions of research. However, it is conceptual advances and insights of a fundamental kind which have allowed real progress in observation of the molecular architecture. An already well-known leap is the realization of optical 'nanoscopes' which overcome the resolution barrier dictated by diffraction of the light standing for over a century [2–10] and now achieve three-dimensional spatial resolution at the nanoscale with regular lenses for focused visible

light in the far-field. In these schemes, molecules as the smallest structural entities themselves take center stage: molecules can be distinguished within the diffraction-limited focal volume by judiciously exploiting their fluorescent properties to allow their sequential detection in time. This insight has been shown to facilitate non-invasive imaging with resolution at a spatial scale close to the molecules themselves. The accomplishment of light-based and thus non-invasive visualization at nanometer length scales reveals its full potential when applied to time-dependent processes, as meaningful experiments must attempt to capture the evolution of a system both at the appropriate spatial and temporal scale. Therefore combining both requirements remains a key motivation behind the work of an increasing number of practicing experimental physicists and engineers.

1.1 Single molecule spectroscopy in living systems

1.1.1 Why single-molecule measurements?

While the very first experiments were limited to the observation of single chromophores embedded in a crystalline matrix at low temperatures by absorption [11], single molecule studies based on fluorescence [12] enjoyed rapid growth. Imaging of single molecules under ambient conditions soon became possible [13–15], over time enabling numerous applications of single-molecule tools in biology. Many reviews have described the insights into complex biological processes provided by the observation and manipulation of single molecules (for recent review articles the reader may consult [16–23]). It is an interesting starting point for the discussion of the value of single-molecule measurements to note that, according to the ergodicity hypothesis, a sufficiently long time-average (or a sufficient number of observations) from a single molecule is equivalent to a standard population-averaged snapshot, suggesting that, in principle, a single-molecule experiment contains all information of the molecular ensemble.

What is the motivation for facing the challenges of making measurements at the single-molecule level? – after all, a major hurdle lies in the interference from the

massive excess of other molecules that contribute to the background, along with photophysical artifacts from the dye label. Besides providing a way to "just look at the thing" (Feynman, [1]) – seeing single-molecule behavior arguably is believing – single-molecule approaches reveal heterogeneity and disorder in a sample, albeit in a finite observation window (typically seconds to hours), which seem to contradict the ergodicity hypothesis but are commonplace in biological systems. Only a dedicated experiment enables precise localization (with nanometer accuracy) and counting of molecules in spatially distributed samples and can thus examine the local situation (environment) of the molcule rather than a bulk behavior. An individual molecule samples its surroundings within a very small volume, possibly just a few cubic nanometers, and can therefore probe its environment and relay chemical information with very high spatial resolution. The molecule therefore provides a valuable interface with the macroscopic world.

A single molecule measurement is the ultimate achievement of measurement sensitivity as it represents the ability to detect, by isolating it or making it otherwise distinguishable from all other identical molecules, 1.66×10^{-24} mole of the object of interest. 1.66 yoctomole – the inverse of Avogadro's number – has also been referred to as a 'guacamole'. By their nature, such measurements enable the quantitative measurement of the kinetics (microseconds to minutes) or statistics of complex biological processes without the need for a perturbing synchronization of molecules to reach a sufficient ensemble-averaged signal. Giving access to the full distribution of molecular behavior they inherently reveal rare and/or transient behavior (for example in biology) or species formed along a reaction pathway (physical chemistry), both of which are typically averaged out in ensemble measurements. In a biological context, it is worth noting that the single-molecule measurements operate at low numbers (typically 1-1000 molecules) that are actually observed for most specific biopolymers (proteins, nucleic acids, polysaccharides) in living cells. They therefore eliminate the need for artificial enrichment and, increasingly, allow the study of their dynamics where it matters: in their native environment, the living cell.

In their combination the described aspects account for the profound intellectual and scientific appeal of single-molecule tools and their imminent potential to revolu-

tionize many aspects of notably the biomedical sciences including, but by no means limited to, structural biology, enzymology or nanotechnology – as they serve to study and interface with natural (or human-built) nanoscale devices. A living system of great importance, the nanoscale structural dynamics of cellular plasma membranes, will be at the heart of this thesis.

1.1.2 Methods for translational dynamics

Many methods are available and are continuously being refined to allow biologists to probe the positions and distributions of particles in dynamic samples, with wide-field optical microscopy as the major workhorse. Figure 1.1 provides an overview of the firmly established kind of experiments on dynamics in artificial or living systems. While ensemble techniques permit only statements about average behavior (the effective mobility over a covered region) to be made, the tracing of the motion of individual particles or molecules contains information about the dynamics one-by-one. Often only such a study can reveal the full complexity such as the exact diffusion paths taken.

As will be described in Chapter 2, the localization of a molecular emitter *in isolation* is, in principle, possible with very high accuracy. For a fixed (immobilized) molecule and sufficient signal integration, a recent experiment with sophisticated checks demonstrated the localization of a single fluorescent molecule with sub-nanometer accuracy [24]. Living systems are *always* in motion. The small membrane-constrained molecules studied in this thesis have considerable lateral mobility. Beginning in the late 1980s, light microscopy of fluorescent beads and metallic nanoparticles attached to biological specimens allowed the localization and tracking of features with spatial resolutions of tens of nanometers and time resolutions of tens of milliseconds, resulting in related techniques such as nanovid microscopy [25], single-particle tracking [26] and tetheredparticle microscopy [27]. As early as 1996, tracking of diffusive motions of membrane-bound, dye-labeled single molecules was reported [28].

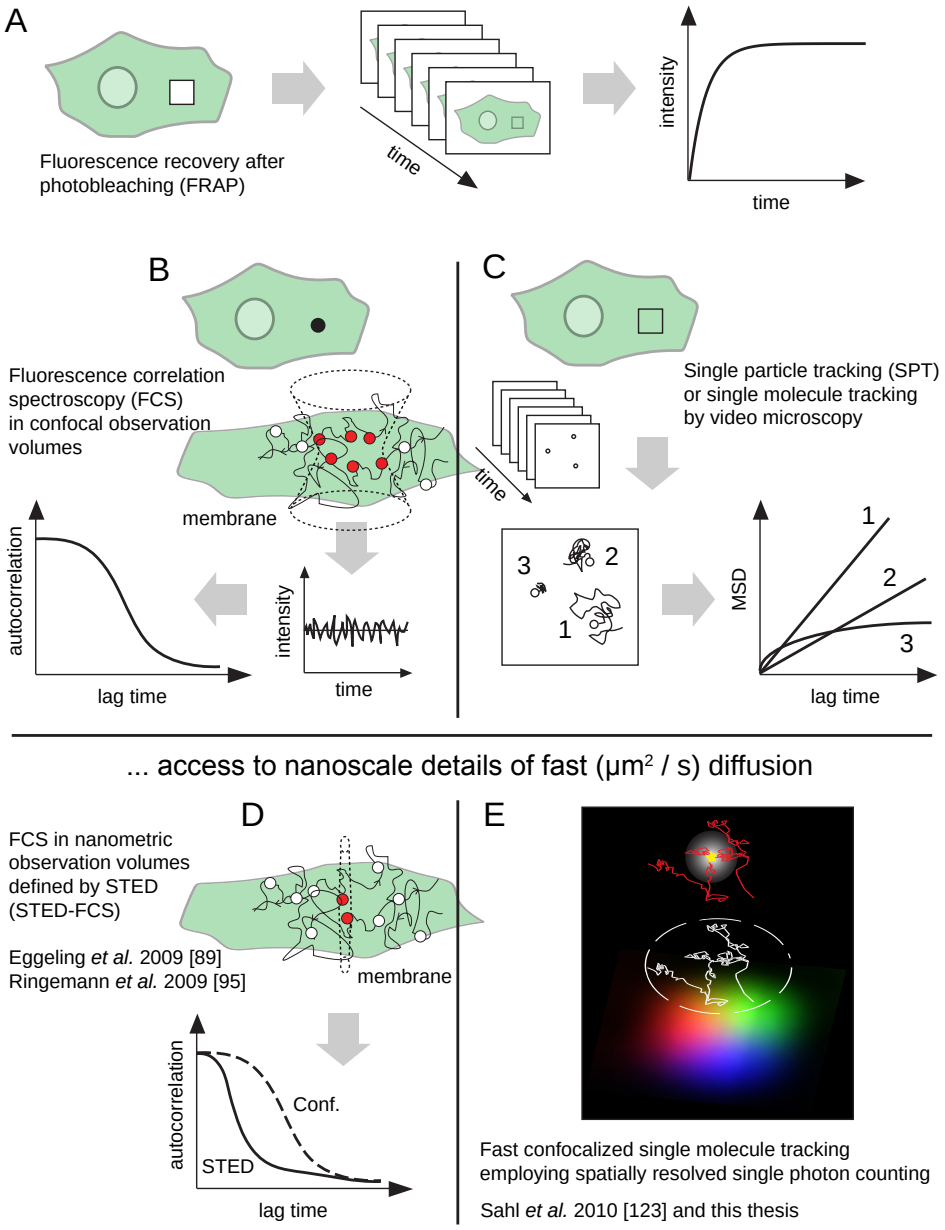

Figure 1.1: Single-molecule sensitivity is essential to reveal details of molecular diffusion in living systems. An ensemble measurement (for example by (**A**) fluorescence recovery after photobleaching (FRAP)) only provides averages for a large number of molecules over time and space of the diffusion in a large area. This method involves the selective photobleaching of fluorescent molecules in a given region (white square) with a high-intensity laser, followed by measuring the recovery of fluorescence intensity in the bleached region as a function of time. The recovery kinetics depend on the speed at which the fluorescent particles move from other regions of the sample to the photobleached area and thus provides information regarding the mobility of the labeled molecules. (**B**) Fluorescence correlation spectroscopy (FCS) measures fluctuations in fluorescence intensity in the femtoliter observation volume obtained in a confocal or two-photon microscope. These fluctuations are due to fluorescent molecules moving in and out of the observation volume. Quantitative analysis through calculation of the auto-correlation function provides information regarding the average residence time, and therefore the mobility of the labeled molecules in that volume. The actual motion of molecules, which is often heterogeneous and may involve complicated behavior such as lateral confinement, is only detectable on a single-molecule basis. This is the realm of (**C**) single-particle-tracking (SPT), or, increasingly, single molecule tracking, as presented in this thesis (**E**). Here, possible mechanisms of motion can be obtained by comparing experimental trajectories with predictions from theoretical motion models. (**D**) STED-FCS in nanometric (attoliter) observation volumes, combining high spatial and temporal resolution for the first time, has proven a powerful tool to dissect fast molecular motion at the nanoscale.

1.1.3 Colloidal particle tracking. Labels and challenges

Most existing single-molecule techniques thus share a range of limitations, especially in the accessible measurement accuracies (spatio-temporal resolution is directly proportional to the amount of signal), time resolutions and time windows. The main problem is posed by the weak molecular signal and potential for loss of the observed molecule. A frequent workaround is the use of colloidal particles as probes in single particle tracking (SPT) experiments by Nomarski (differential interference contrast) or bright-field video microscopy. Such 40 nm colloidal particles bound to molecules (or small groups of them) are very bright and could be observed with spatial localization accuracies of as good as $\sigma_r \approx 2$ nm standard deviation at video rate or $\sim$17 nm even at 40,000 frames/s (25-μs) resolution [29, 30]. While these experiments feature impressive spatio-temporal resolution, the large size of the gold probe (Figure 1.2A) has been shown in various studies (e.g. [31]) to cause crosslinking of the target molecules or steric hindrance effects. It also precludes potential application to intracellular molecules. This thesis sets out to realize experimentally the dynamical observation of a single small ('genuine') molecule (as opposed to a colloid of tens of nanometers) at the physical limits set by its signal. Fluorescent lipid analogs (Figure 1.2B) serve as an illustration of the immense practical value of the enhanced spatiotemporal resolution gained by a novel experimental strategy.

1.2 Overview of this thesis

Fast molecular dynamics by spatially resolved fluorescence photon counting

In this thesis we introduce an optical scheme for the observation of single molecules by a quasi-continuous read-out of their fluorescence photon stream. The approach taken allows single-molecule localization and in particular the recording of molecular trajectories with spatio-temporal resolution at the absolute photon shot noise limit. This translates to remarkable spatio-temporal resolutions for currently available bright organic dye labels and it affords a flexible choice of high spatial accuracy

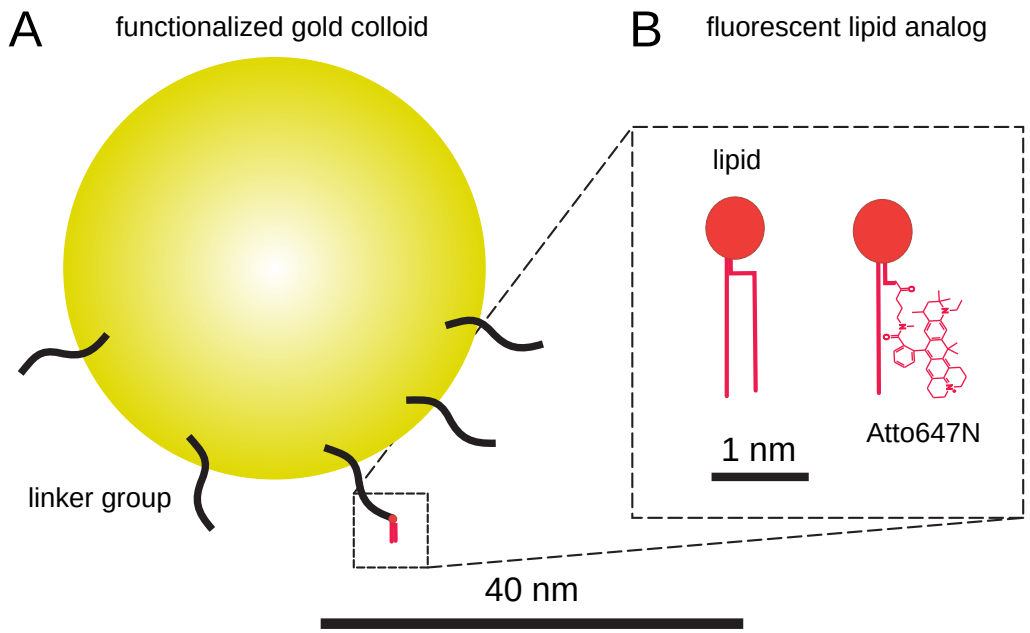

Figure 1.2: Colloidal particle tracking achieves high temporal resolution due to high photon fluxes of scattering signal. (**A**) A 40 nm gold colloid attached by a chemical linker group to a lipid (1–2 nm) features a considerable size mismatch. The heavy and rather large particle may alter the diffusion behavior. In particular, crosslinking by its linkers to several target molecules has been described. The unspecific interaction with other membrane constituents may also critically limit its value as a non-invasive probe reporting on nanoscale lipid diffusion. (**B**) Fluorescent lipid analog created by replacement of one acyl chain by the lipophilic dye Atto647N. Comprehensive controls in our experiments (Chapter 3) show that head-labeled variants (dye at the lipid-water interface) display the same diffusion behavior, which is determined by the chemical nature of the host molecule. The analog is thus an excellent approximation to the native cargo-free lipid.

(∼10-20 nm standard deviation) with simultaneous sub-ms temporal resolution. This level of spatio-temporal accuracy and the ultimate sensitivity (signal-to-background ratio of >200 under typical conditions) of our measurement apparatus open up the possibility to address prominent questions in membrane dynamics of living cells. Details of nanoscale diffusion at the single-molecule level are obtained for lipids and other small molecules. Remarkable differences between different molecules are observed, correlating with their chemical nature. We directly observe transient events of trapping on <20 nm spatial scales. The trapping is cholesterol-assisted and much more pronounced for a sphingo- than for a phosphoglycero-lipid, with average trapping times of ∼15 ms and <4 ms, respectively. The results support previous STED nanoscopy measurements and suggest that, at least for nontreated cells, the transient interaction of a single lipid is confined to macromolecular dimensions. Our experimental approach demonstrates that fast molecular movements can be tracked with minimal invasion, which can reveal new important details of cellular nano-organization. Here, we outline the contents of this thesis.

Chapter 2 describes the principle of fast confocalized molecular tracking, along with considerations of its accuracy and best technical implementation. Position sampling from a continuous photon stream is discussed, facilitating the detection of short-term lateral confinement, that is, an arrest from Brownian diffusion for a duration of the order of just several sampling time steps. Other beneficial aspects of employing time-correlated single photon counting for molecule tracking are described, such as photon count integration on a moving-average basis and the concomitant increased statistical basis of the step histograms, or a superior burst selection capability from photon-binned time-traces.

Chapter 3 then describes the application to fast-diffusing lipid and other small membrane molecules in the plasma membrane of mammalian cells. The nanoscale inhomogeneities in the diffusion are assessed in light of previous measurements by STED-FCS, the only other optical far-field approach to date for investigating molecular diffusion with exceeding spatial and temporal resolution. The emerging picture based on functional chemical groups responsible for specific trapping behavior is discussed. Monte Carlo simulations of lipid-trap kinematics along with the resulting

photon traces consolidate this discussion and provide a consistent explanation of the STED-FCS and molecular tracking data. All data is also discussed in the context of a model of molecular hop diffusion among partially permeable membrane compartments, which fails to explain the observed prolonged stays in a fixed location.

Complete photon statistics in fluorescence nanoscopy

The capability to localize molecules with very high accuracy and precision is desirable in a new class of far-field fluorescence microscopy schemes with resolution better than the diffraction limit. On-off control of the molecules by mechanisms as for example photoswitching is the central element in all these schemes. Chapter 4 describes such 'nanoscopy' with our single-photon-counting setup, and highlights resulting advantages such as access to the full photon statistics, accurate molecule identification and describes why there should be the potential of a slightly enhanced resolution compared to a strictly time-binned acquisition (such as a camera with fixed frame rate).

The thesis is concluded in Chapter 5 with an outlook and potential applications, including the extension to two-color colocalized measurements in fast confocalized molecular tracking. This may allow studying molecular interactions of several species and clarifying the role of protein-lipid interactions in nanoscale molecular complexes.

Chapter 2

Fast molecular tracking by spatially resolved single-photon-counting

Many open questions in biology can be tackled only if the dynamics of individual molecules can be observed noninvasively in vivo and at the appropriate spatial and temporal scale [19, 32–35]. Over the years, specific labeling of the cell's constituent parts with fluorescent markers has enabled deeper understanding in many areas of cell biology and allowed, for example, the spatiotemporal tracking of single particles [25, 29]. However, to reach the desired spatial and temporal accuracy, single-particle tracking often applies bright but large and clumsy signal markers, which potentially influence the system under study. By contrast, small molecules can be attached, using well-established conjugation protocols, to a large variety of biomolecules. Their small molecular weight warrants that their attachment to bigger molecules would be expected to have a negligible effect on the biofunctionality of the molecule. But irreversible photobleaching upon repetitive excitation-emission cycles imposes a limitation for tracing applications with typical fluorophores, as it restricts the time interval over which the target molecule can be tracked optically. In this Chapter, we describe a methodological advance in single molecule tracking. Our experimental strategy is targeted at the non-invasive observation of small and, by

comparison with scattering signals of a gold colloid or fluorescence from a quantum dot, comparatively dim fluorophore molecules. Organic fluorophores have extinction coefficients of 1–20 $\times 10^4 \mathrm{M}^{-1}\mathrm{cm}^{-1}$, which is a factor of 10–1000 lower than for quantum dots. Quantum dots have become popular labels in tracking applications because they do not photobleach.

The method combines principles from confocal microscopy [36] and state-of-the-art single-photon detection in a very effective way. As will become clear, the described experiments (Chapter 3) herald the possibility of a shift of thinking about tracking technology (Figure 2.1), from

step-wise signal integration over fixed time intervals Δt on a camera (with current technology $\geq$ 2 ms, but usually 5–40 ms for better noise reduction, see below) leading to averaged molecule positions over Δt

$\Downarrow$

uninterrupted read-out of the photon-stream with nanosecond time resolution for each photon by time-correlated single-photon counting (TCSPC). Photons may be grouped at leisure for localizations to sample the molecular dynamics as appropriate.

Combined with the excellent signal-to-background ratio of fluorescence detection in our confocal microscope geometry, this provides for an experiment that is ideally suited to capture nanoscale details of diffusion of small molecules.

Optical localization of an isolated point emitter

As early as 1930 Heisenberg was the first to point out that by calculating the center of mass of the diffraction-limited image of a single emitter its position can be determined with an accuracy $\Delta r'$ that is given by

$$\Delta r' = \frac{\Delta r}{\sqrt{N}}, \tag{2.1}$$

where Δr is the full width at half maximum (FWHM) of the diffraction limited point spread function (PSF) of the detection optics and N is the number of detected

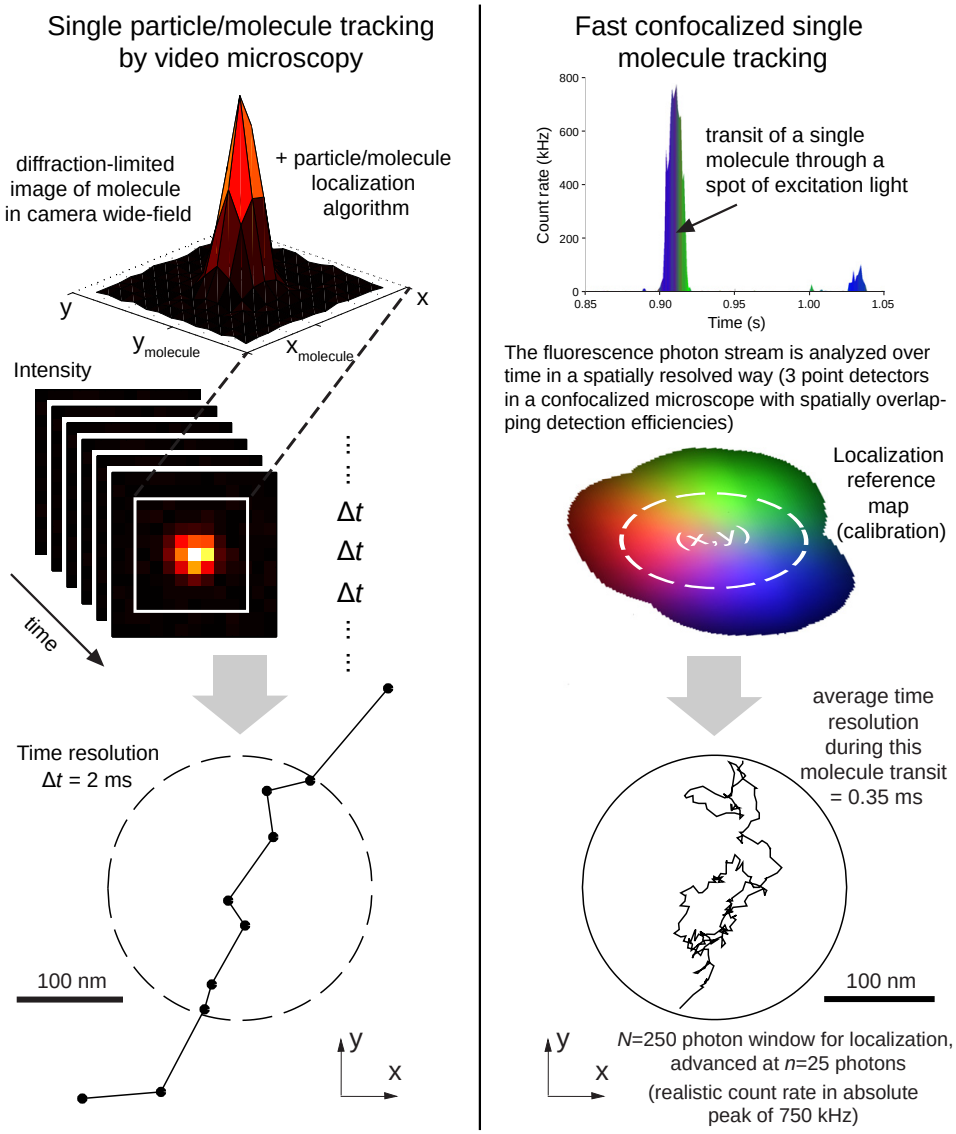

Figure 2.1: Tracking in a confocal microscope by spatially resolved fluorescence photon counting, in contrast to tracking by camera-based video microscopy. (**A**) In single particle or molecule tracking by video microscopy, the region of interest is imaged in a wide-field microscope onto a camera. The contrast-giving mechanism is typically either scattering (from colloids) or fluorescence in the case of single molecules. From the image-stack with delay between images $\Delta t = \Delta t_{exposure} + \Delta t_{readout}$, a trajectory may be constructed by recovering the particle position in each image frame from the observed intensity distribution. (**B**) Fast confocalized tracking enables single molecule observation with high sensitivity. The elicited quasi-continuous stream of fluorescence photons from an individual molecule passing through the fcous is recorded on spatially distinct detectors (fibers connected to single-photon-counting avalanche diodes). The molecule may be localized in quick succession with high flexibility as to the exact signal integration, as signal is available at the single-photon level. The approach achieves excellent signal-to-background ratios (>200) for small dye-labeled molecules in membranes of live cells and exceeds other published experiments by a factor of five to ten in spatio-temporal resolution, at the expense of a smaller observation area. Trajectories as obtained with both methods are shown (compare Figure 2.10).

photons [37]. The origin of localization error in the purely photon (shot) noise-limited case is conceptually simple. Each photon collected in the image plane of the optical instrument gives a measure of the position of the emitter, and the position error of each measurement is the same as the standard deviation of the detection PSF of the microscope. The best estimate of the position is then given by the average of the positions of the individual detected photons, with the error given by the well-known expression for the standard error in the mean

$$\langle (\Delta r')^2 \rangle = \frac{\sigma_{PSF}^2}{N}, \tag{2.2}$$

where $\Delta r'$ is the error in the localization, σ_{PSF} is the standard deviation of the PSF (Gaussian or otherwise), and N the number of photons collected. On pixelated detectors and under influence of background noise, further considerations apply for optimal results [38].

2.1 The concept: Continuous photon counting on separate point detectors

Detection elements – a limiting factor in fast single molecule observation?

For the detection of single molecules in a wide-field microscope, a specialized charge-coupled device (CCD) has become the detector of choice. A CCD camera does not count single photons per se but integrates photoelectrons over time with good quantum efficiency. The noise in each pixel of a cooled CCD chip does not notably increase with integration time, so longer integration leads to improved signal-to-noise ratio. Modern CCD cameras reach single-fluorophore detection sensitivity with ∼2-100 ms integration times and use either image intensifier tubes with a photocathode, microchannel plate and phosphor screen (in an intensified CCD), or on-chip multiplication of photoelectrons (in an electron-multiplied CCD). The CCD imaging of the diffraction-limited spot of a single fluorescent molecule has recently become very popular in many imaging and tracking applications [19, 38–41]. While nowadays featuring high quantum yield, the detection by a CCD is limited by the frame readout

rate and its noise characteristics. In present camera technology, additional sources of noise are related to the charge movement during the read-out process. Especially for larger fields of view and therefore charge shuffling over more pixels, this contribution may become significant. As a consequence, more signal is required to attain comparable SNR as in a 'single-point measurement' performed by confocal fluorescence microscopy. The latter usually relies on single photon counting with avalanche photodiodes (SPADs or APDs) [42] of nanosecond response time [43]. A photomultiplier tube would have a larger detection area, but offers lower quantum efficiency and requires higher operating voltage, which produces noticeable dark counts even when cooled [42]. The time resolution of a single fluorescent molecule detected by an APD is mostly limited by the photon count rate, which can be enhanced up to the excitation saturation level of the fluorophore at the expense of faster photobleaching, as outlined later.

The experimental approach

We modify far-field epi-illumination confocal micoscopy to allow localization at the nanoscale. Such an experiment no longer is a mere 'single-point measurement', as it will have the potential to differentiate photons originating at different points in the focal area.

We apply a confocal microscope in conjunction with single-photon counting detectors. Fast sequential localization and thus spatio-temporal tracking of individual molecules is realized by collecting the fluorescence on at least three separate point detectors arranged in close proximity (Figure 2.2A).

By choosing the concentration of the fluorescent molecules low enough, we ensure that within our focal area of observation at most one single fluorescent molecule is found at any time, which diffuses and thus explores its surroundings. If the molecule passes through the stationary focal area of our confocalized microscope, a burst of fluorescence photons is elicited by continuous-wave laser excitation and imaged onto the input faces of three optical fibers, each coupled to a different detector. The fibers are arranged in closest packing such that their projection back into sample space

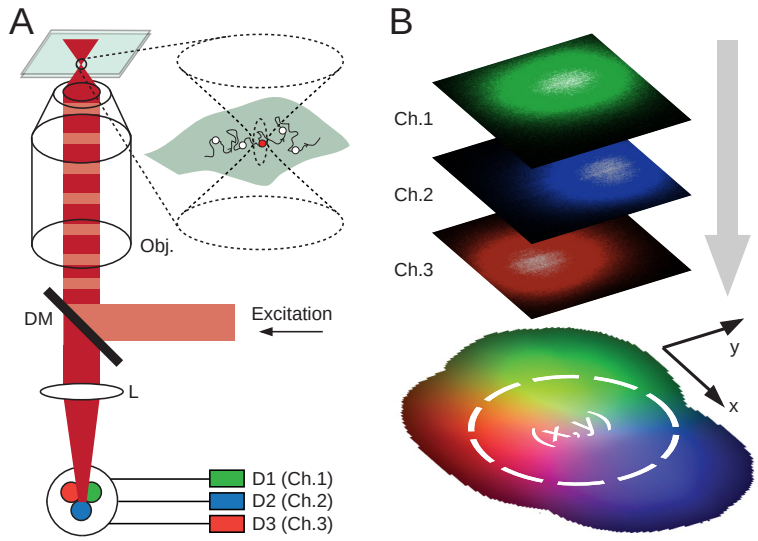

Figure 2.2: (**A**) Principle of fast confocalized single-molecule tracking. Optical arrangement. Fluorescence excited in the focal region is imaged onto a quasi-confocal detection area of three densely packed fibers. Signals from the connected three avalanche photodiodes (APDs) are recorded in a single-photon counting mode. (**B**) Reference map encoding the relative distribution of photon counts on the three detectors for a fluorescent object as a function of position (x, y). This map was obtained by scanning a 40 nm fluorescent bead over a 500 nm $\times$ 500 nm observation region and combining the count information on all three channels. Colors denote detector affiliations.

forms a triangle with overlapping detection pointspread functions (PSFs). The use of several distinct detection pinholes to obtain localizations was suggested [44, 45] and also demonstrated [46, 47] with individual quantum dot probes in conjunction with fast translational feedback motion of the sample.

Other sophisticated instruments can track particles "on-the-fly" in 3D by scanning one or several laser spots in elliptical or circular orbits using feedback loops to keep the particle at the center of the observation field [48, 49]. While these schemes have enabled extended observation times of tens of milliseconds to seconds, the rather large labels (quantum dots) may potentially influence the system under study. By contrast, our approach is equally well suited for small dye labels. As neither scanning nor feedback is required, our setup is rather simple, just using multiple pinholes, represented by the fibers, instead of a single one. Because of the limited observation

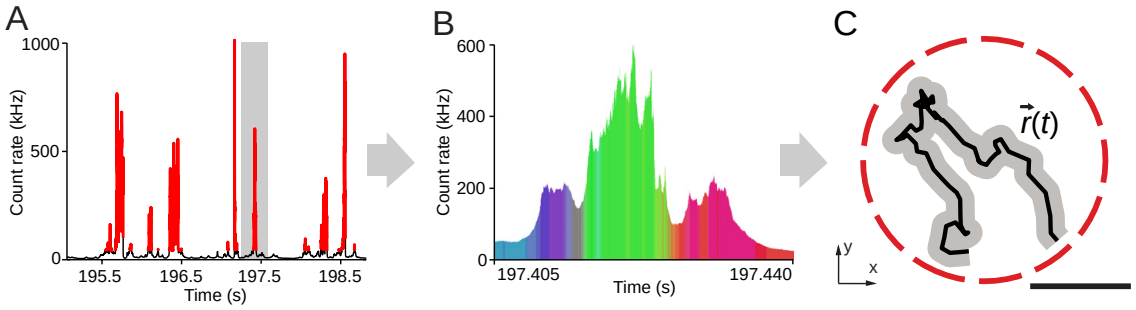

Figure 2.3: Spatio-temporal information on fast-diffusing individual molecules. (**A**) The fluorescence signal over time is detected on all three detectors. Molecular transits through the observation spot are identified and selected as bursts (red) in fluorescence signal. (**B**) Comparison of the signal values (S_1, S_2, S_3) of a selected burst with the reference map $\{(R_1, R_2, R_3)\}$ by a maximum likelihood scheme (colors denote detector affiliations) yields (**C**) the lateral position (x, y) and, by repetitive localization, a molecule trajectory $\vec{r}(t) = (x(t), y(t))$. (Scale bar, 100 nm.)

area (diameter ∼250 nm), the trajectories in our scheme are short, yet we collect many hundreds of these trajectories in a measurement because single molecules quickly enter and leave the focal area.

2.2 Optical design: the confocalized microscope and localization

2.2.1 Experimental setup

A confocal microscope was set up (Figure 2.4B) using an oil immersion lens (100×, NA = 1.40, Leica) to focus the circularly polarized laser light into the sample (by overfilling the lens back aperture). The dyes were excited with a 633 nm continuous-wave (cw) Helium-Neon laser (Melles Griot) at a power $P \approx 5 - 20$ μW, i.e., focal peak intensities of ∼5–20 kW/cm^2 set by a power controller unit (LPC; Brockton Electronics). The collected fluorescence passed through a dichroic mirror and filters and was imaged with a magnification of 200× onto the input faces of three optical fibers, each coupled to a single-photon avalanche photodiode (APD; SPCM-AQR-13-

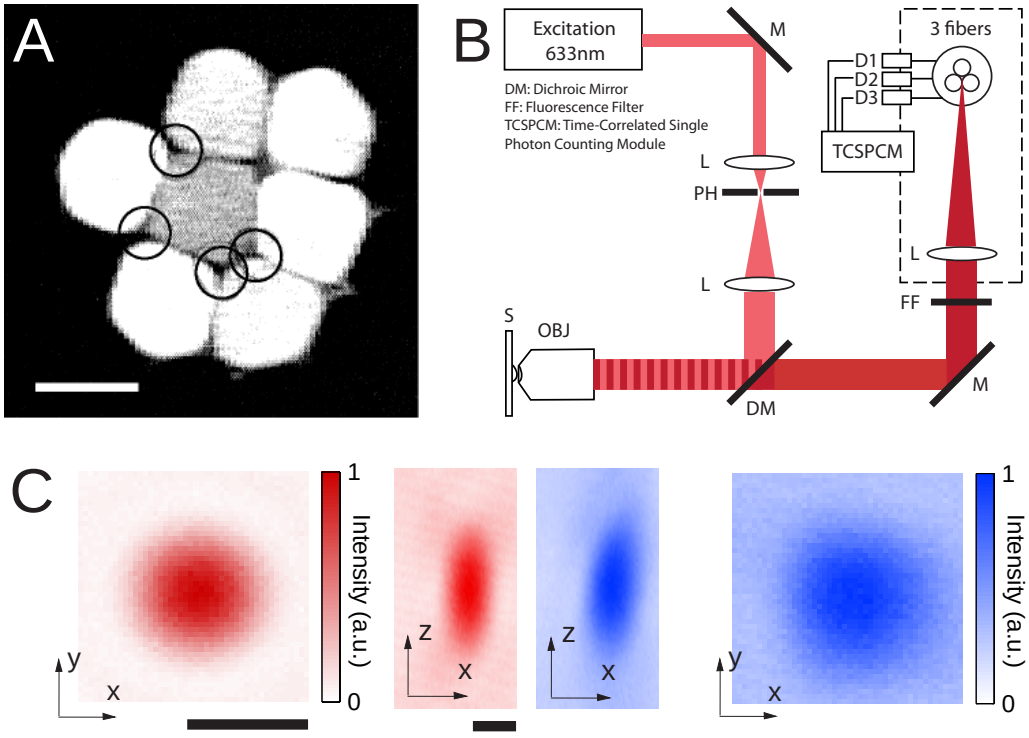

Figure 2.4: The experimental setup for fast molecular tracking. (**A**) Micrograph of fused fiber bundle. The central fiber is used in combination with two adjacent fibers. The small circles indicate some possible combinations. We highlight that our concept of the localization reference map, i.e., the encoding of the relative detection efficiencies as a function of the emitter position, readily deals with point-like detectors in almost arbitrary configurations. The fibers need not be equidistant from each other, although this is advantageous for a uniform localization accuracy. (Scale bar, 125 μm.) (**B**) Details of optical arrangement. (**C**) Near-diffraction-limited excitation point spread function (PSF) at $\lambda = 633$ nm measured on a 80 nm gold bead in reflection mode. A blue ($\lambda = 473$ or 491 nm) PSF (of spherical abrration and thus larger extent) was overlapped in some experiments for visualization of complementary labels in a separate color channel. (Scale bars, 300 nm.)

FC, PerkinElmer). The optical fibers were arranged in closest packing such that their backprojection into the sample formed a triangle with overlapping detection PSFs. We used multimode step-index fibers with 100 μm core diameter (CeramOptec) that were fused together at the common end, allowing an effective center-to-center detector separation of $\sim$125 μm. The central fiber was used in combination with two adjacent fibers (Figure 2.4A). The APD signals were recorded by a time-correlated single-photon counting module (SPC-830; Becker & Hickl). The channel information (1, 2, or 3) was preserved by a router (HRT-82; Becker & Hickl). All experiments were performed with a stationary focus and the sample stage at rest. We used a closed-loop piezostage (NanoMax; Melles Griot, or Tritor 102; Piezosystem Jena) for the recording of reference images and maps and for alignment procedures.

2.3 Localization Analysis and Calibration

2.3.1 The position reference map

Knowing the relative detection efficiencies of the three detector channels for objects placed at different points in the focal plane, the position of the fluorescent molecule can be traced from the signal distribution on the three detectors. To this end, we established a reference map (Figure 2.2B) by scanning a fluorescent bead through the focus and recording the three detector signals as a function of the bead position. The single-molecule experiments were then performed as follows (see Chapter 3 for a detailed description of the data analysis at the single-photon level): Traces of photon data with information on single-photon arrival times and identification of the corresponding detector channel (1, 2, or 3) were recorded during typically 5–10 minutes. Individual molecular transits were identified (Figure 2.3A) as the fluorescence bursts exceeding a threshold level of fivefold the background signal (offset) during the measurement. Binning photons, either in fixed time-steps or in groups of a fixed total photon number N per localization step, yields three count values S_1, S_2 and S_3 in channels 1 to 3, respectively. This triple (S_1, S_2, S_3) is compared to the reference map to find the coordinates (x, y) where it best matches the reference triple

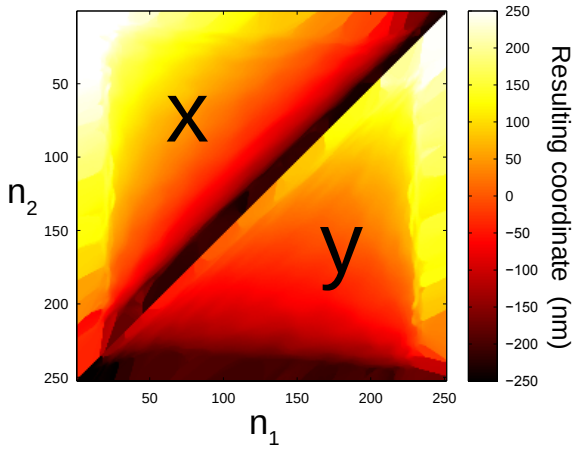

Figure 2.5: Maximum likelihood estimation (MLE) of position for fixed number of total photons. (**A**) Look-up table holding the results of all possible localization outcomes for $N = 250$ photons. The configuration space for N photons on three detectors is dramatically reduced and all possible combinations $\{(n_1, n_2, n_3 = N - n_1 - n_2)\}$ can be saved in a 2D matrix of dimensions $(N + 1) \times (N + 2)$ storing the most likely positions (x, y). The trajectory is then immediately found by looking up the positions at the corresponding count values. This makes the matching process very fast.

$\{(R_1, R_2, R_3)\}$ encoding the relative detection efficiencies. The best agreements of all recorded positions yield the trajectory

$$\{(x, y)\} = \vec{r}(t)$$

of the molecule (Figure 2.3C). Employing a single-photon counter instead of a time-binned detector allows grouping the detected photons into sets of a desired number N, which allows a more reliable estimate of the accuracy of each localization.

Maximum likelihood estimation of position

We discuss the process of matching count rates during a time interval to the experimental reference map (calibration). This is realized by an estimator for the maximum likelihood that the triple (S_1, S_2, S_3) corresponds to $\{(R_1, R_2, R_3)\}$ and resulting assignment of spatial coordinates (x, y) in the focal plane.

The likelihood of detecting n events for $\langle n \rangle$ events on average is given by the

Poissonian probability density function

$$\mathrm{p}(n, \langle n \rangle) = \exp(n \cdot \ln(\langle n \rangle) - \mathrm{gammaln}(n+1) - \langle n \rangle) \tag{2.3}$$

The likelihood of detecting (n_1, n_2, n_3) events at a position with $(\langle n_1 \rangle, \langle n_2 \rangle, \langle n_3 \rangle)$ events on average is given by the product of the probabilities

$$\mathcal{L}\left(\vec{n}, \langle \vec{n} \rangle\right) = \prod_{i=1}^{3} \mathrm{p}\left(n_i, \langle n_i \rangle\right) \tag{2.4}$$

The most likely position for a given (n_1, n_2, n_3) triple is then the location where this probability is maximum, which is equivalent to finding the maximum of the sum

$$\ln\left(\mathcal{L}\right) = \sum_{i=1}^{3} \ln\left(\mathrm{p}\left(n_i, \langle n_i \rangle\right)\right) \tag{2.5}$$

where the average $\langle n_1 \rangle + \langle n_2 \rangle + \langle n_3 \rangle \stackrel{!}{=} n_1 + n_2 + n_3$, that is the number of detected events N. This yields the logarithm of the likelihood

$$\ln\left(\mathcal{L}\right) = \vec{n} \cdot \ln\left(\langle \vec{n} \rangle\right) - \sum_{i=1}^{3} \mathrm{gammaln}\left(n_i + 1\right) - N. \tag{2.6}$$

The last two terms are invariant with the position. The scaling of the average triples is skipped, as this would lead to an additive term $N \ln(N)$, which is again invariant with the position. Finally, the scalar product

$$\vec{n} \cdot \ln\left(\langle \vec{n} \rangle\right)$$

is calculated using a matrix product, that is

$$\vec{S} \cdot \ln\left(\vec{R}(x, y)\right)$$

is searched for the maximum to yield the most likely position. Note that the maximum likelihood estimate by maximizing $\ln(\mathcal{L})$ is the same as maximizing $\mathcal{L}$ since the logarithm is a monotone transformation.

For a sequence of localizations with a known photon number N (as results when partitioning the photon stream during a fluorescence burst into windows of N consecutive photons), the maximum likelihood estimation takes an especially simple form:

counts in two channels (n_1, n_2) determine the triple and thus localization, because the third value is given by $n_3 = N - n_1 - n_2$. The resulting position from maximizing the likelihood may be compactly saved in a $(N+1) \times (N+2)$ matrix (Figure 2.5) and the position for count triples (n_1, n_2, n_3) (satisfying $n_1 + n_2 + n_3 \stackrel{!}{=} N$) read out instantly, making the analysis very fast computationally.

2.3.2 The experimental limits of localization accuracy

Localization Performance

Tests were performed to ensure that the localized position by our method, i.e., the allocated x and y coordinates based on photon data, is reliable and solely subject to the known error. Depending on the number of photons utilized in a single localization, the accuracy will vary. To demonstrate this, isolated 24 nm-sized fluorescent beads at rest were localized repeatedly utilizing a varying number of photons, and the spread of 10,000 independent localizations in each case was examined (Figure 2.6). The radial standard deviation

$$\sigma_r = (\sigma_x \cdot \sigma_y)^{1/2} \approx \sigma_x \approx \sigma_y$$

of the cloud of localized positions is a measure of the localization accuracy and was found to be $\sigma_r = 12.2$ nm for $N = 250$ photons, scaling with $N^{-1/2}$ as expected. Fluorescent beads scanned linearly through the observation region were adequately localized (Figure 2.7). The entirely background-free measurements of immobilized beads represent the absolute lower bound on the localization accuracy attainable with our instrument.

We verified that the localization procedure does not introduce any bias or inconsistency. The data triple (R_1, R_2, R_3) of each point in the reference map was scaled to N photons. These scaled triplets were used as signal $\{(S_1, S_2, S_3)\}$ to be localized with the same reference map. In the central region, the localized positions deviated only by $\sim$3 nm or less from the known points (Figure 2.8). These deviations $|\Delta|$ were thus insignificant compared with the photon-limited position accuracy $\sigma_r \approx 10$ nm of our experiments. An examination of >70,000 localizations from single-molecule

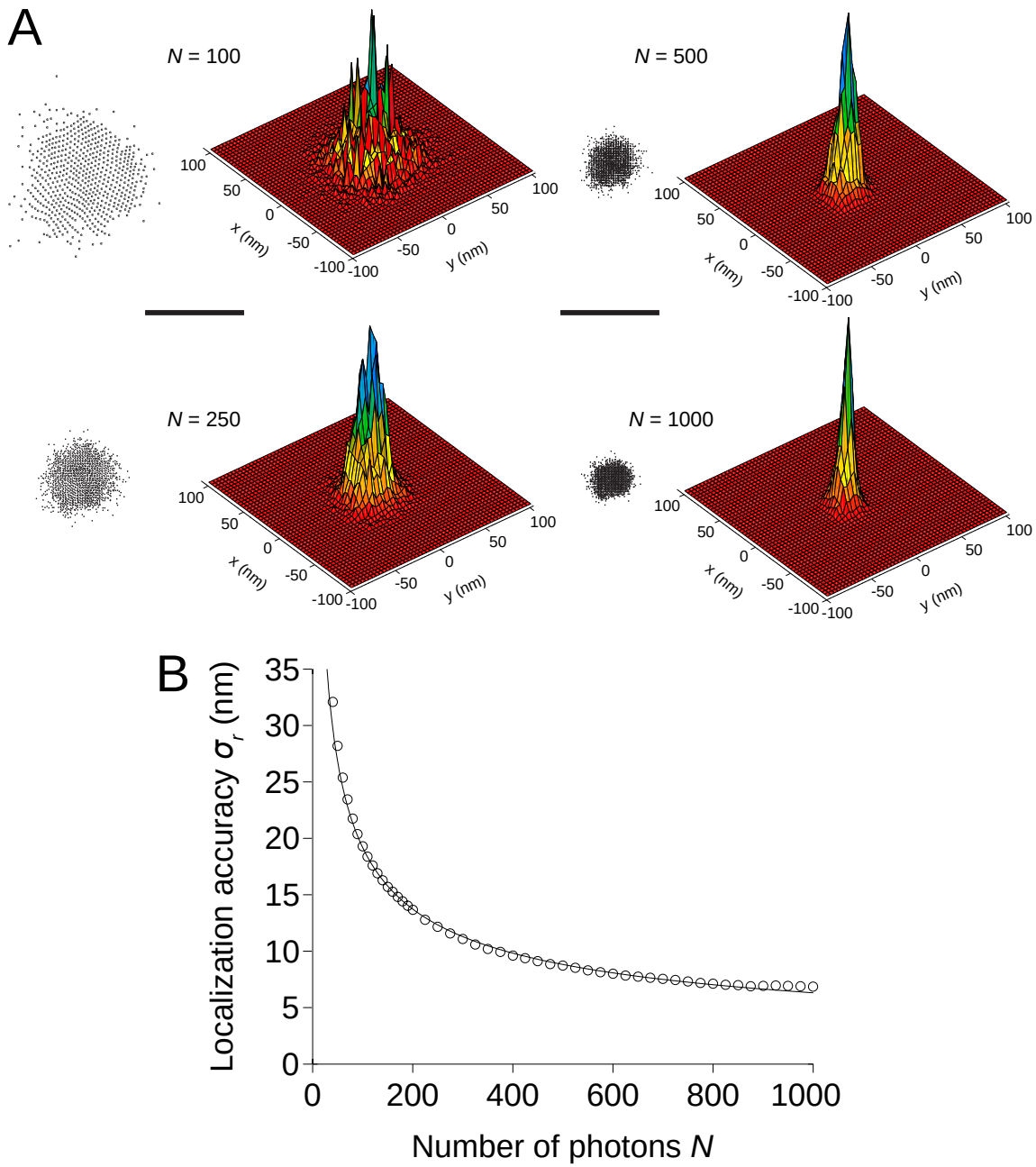

Figure 2.6: Shot-noise limited localization accuracy. Localization accuracy σ_r versus photon number N. An isolated 24 nm fluorescent bead was localized repeatedly for a varying number of total photons N. The spread of 10,000 independent localizations in each case was examined (Scale bar, 100 nm). The radial standard deviation $\sigma_r = (\sigma_x \cdot \sigma_y)^{1/2}$ was found to scale with $N^{-1/2}$ as expected.

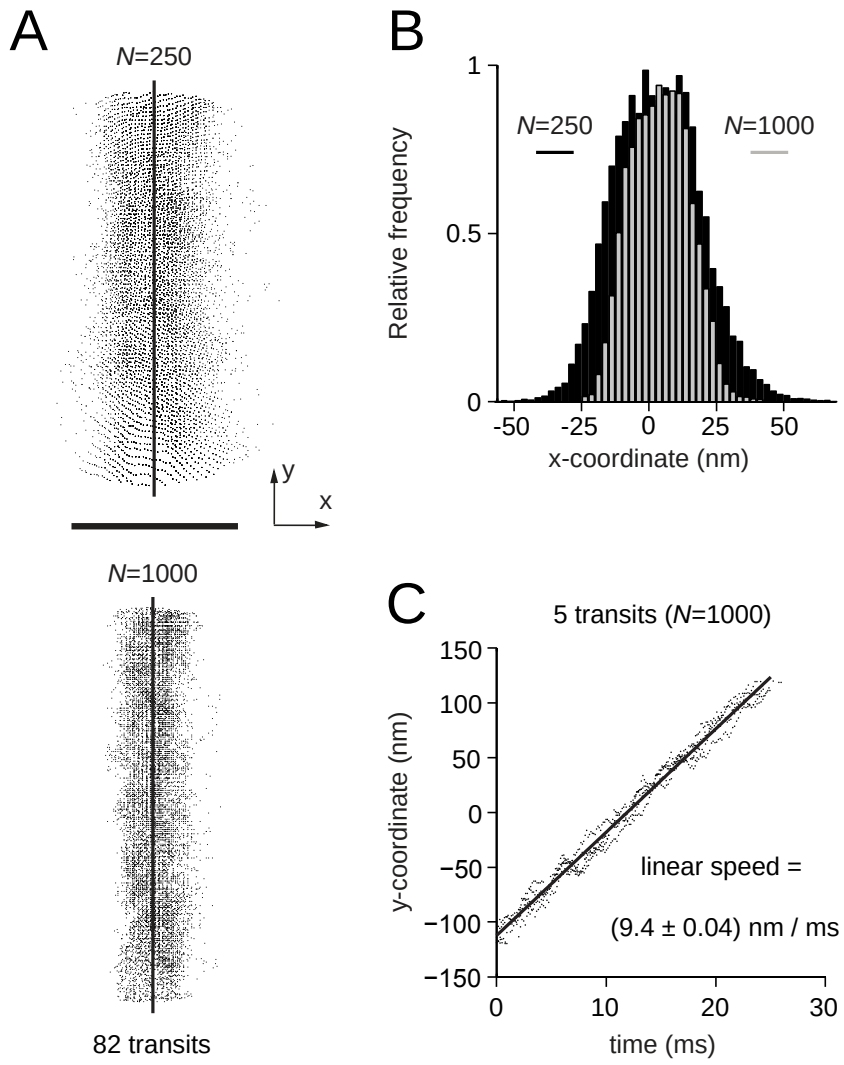

Figure 2.7: Tracking moving fluorescent beads (**A**) Single 24 nm fluorescent beads scanned on a straight line through the observation region (82 transits) are adequately localized. (Scale bar, 100 nm.) (**B**) The spread in the direction orthogonal to the transit is slightly higher than predicted from the stationary determination of the localization accuracy σ_r (Figure 2.6), presumably as a result of small transverse oscillations induced by the scanning stage. (**C**) The set linear scan speed of $\sim$10 nm/ms is reproduced with a relative error of -6 % (settings: 100 pixels at dwell time 1 ms for a distance of 1 μm).

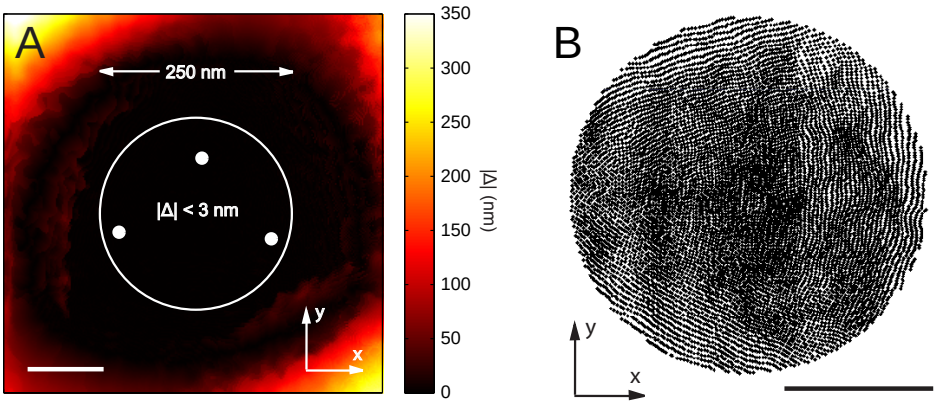

Figure 2.8: Properties of the localization process. (**A**) Self-consistency of the localization map. By successively localizing each pixel element of the reference map through the maximum-likelihood scheme onto the identical map, followed by examining the displacement induced by this process, it became evident that the localization procedure has near-perfect fidelity. The systematic deviations $|\Delta|$ in the central region of observation, to which analysis was limited, were $\sim$3 nm or less (for $N = 250$ photon maps). The white circles indicate the central positions of the three detection channels. (**B**) Example of >70,000 localizations from lipid (PE) transits in living mammalian cells (Chapter 3). The distribution on the map shows no discernible structure. Detailed analysis revealed that the probability of finding a lipid in a given area element is roughly uniform over the whole observation region, with deviations following a Poisson distribution. (Scale bars, 100 nm.)

transits shows that their distribution on the map exhibits no discernible structure and is deemed uniform (Figure 2.8).

2.3.3 Position information is in the gradients of detection efficiencies. Optimization of parameters

The physical separation of the detectors, the lateral magnification of the microscope and thus the back-projected separation of their centers in the excitation focus (sample space) determine the sensitivity of the relative signals (i.e., the signal ratios between the three detectors) to changes in lateral position of the point emitter (Figure 2.9). Fast focus field calculations based on [50] allowed us to study this effect and optimize the magnification. The gradients in signals tend to be highest near the center of the detector arrangement. If the magnification is either too small or too large, the usable area for accurate localization is substantially reduced. In the case of $M < M_{good\,match}$, the fibers are too far apart and respond mostly if the emitter is at the outside close to one of the fibers. For $M > M_{good\,match}$, the detectors respond too much in accord with each other (their detection efficiencies overlap too much), rendering the area of distinguishable count combinations small. A lateral magnification of ∼200–250 yielded an adequate coverage of the central 250 nm at high localization accuracy. The combinations of expected counts from a molecule in this region are unique, which is key for an accurate localization.

2.4 Advantages of quasi-continuous fluorescence sampling

The state-of-the-art detection and recording have allowed us to push molecule localization to the shot noise limit: Low levels of background fluorescence assumed (as are found in our extremely sparsely labeled cell membranes), we are only limited by the number of photons detected from the emitting molecule.

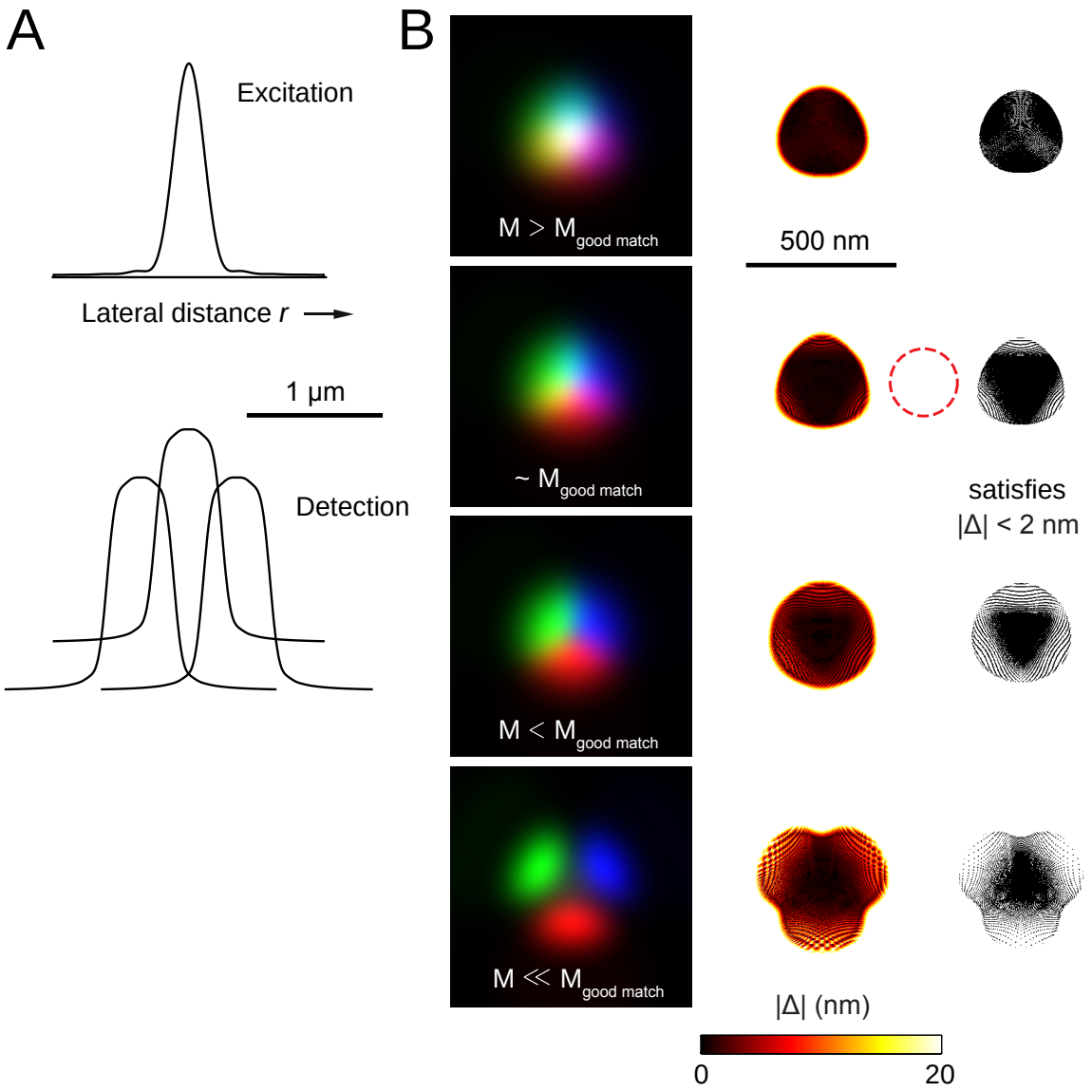

Figure 2.9: Optimization of spatial gradients in the *relative* detected photon numbers on detectors 1–3. (**A**) Projection of the three fiber input faces (detection elements) with collection efficiencies $Q_i(x, y)$ back into the sample space, which features an intensity distribution of excitation light given by $I_{exc}(x, y)$ — the diffraction-limited PSF. (**B**) The lateral magnification factor M of the imaging onto the fibers determines how well the projected detector separation is matched with respect to the excitation PSF (see text). A condition of reasonable confocality must also be fulfilled, allowing both high collection efficiencies and sufficient optical sectioning. A lateral magnification of ∼200–250 is a useful compromise, permitting high localization accuracy over a ∼250 nm region.

Enhanced statistical basis of trajectories

Experimental realizations of single molecule tracking always represent an incomplete sampling of the true trajectory taken by the observed molecule. Figure 2.10 illustrates this point. Panel (A) shows a molecule trajectoy resulting from a random walk at a diffusion constant $D = 0.3\mu\text{m}^2/\text{s}$, simulated with a time increment of 1 μs. The position is plotted every 50 μs. In the following we assume illumination conditions concomitant with a peak count rate from the molecule of 750 kHz. Figure 2.10C gives an indication of the trajectories that would be obtained with camera-based tracking at various integration times Δt. Camera exposures over 5, 2 or 1 milliseconds (the fastest reported experiments have reached 1 millisecond for small dyes) lead to a significant loss of information. While enough signal is collected during this time window, time-averaging of the proper motion of the molecule leads to a measured average position during Δt. The camera trajectories above were thus obtained by computing the center of mass of the true molecule positions during each interval.

The phenomenon of time averaging cannot be avoided in our single-photon-counting approach. However, the intervals over which we average can be chosen much shorter. From a technical viewpoint, we are given this opportunity as a result of the high base time resolution of our photon-counting electronics of 50 nanoseconds. But it also is physically sound to do so because the count rate from the single molecule in our setup is high enough (750 kHz is realistic) to achieve a concomitant high spatial localization accuracy given by the shot-noise-dominated σ_r (Figure 2.6). This is because a good fluorophore is intrinsically bright enough to allow – as our experimental scheme shows – more detailed sampling of its path than is achieved by wide-field camera experiments. The result is shown in Figure 2.10B, computed under our typical conditions with an experimental reference map. The obtained trajectory features better sampling than those in (C) and reproduces the central looping path taken by the molecule. At the periphery of the observation region, spatio-temporal resolution is lower (see below) and some detail in the motion is lost.

In addition to a true bandwidth (spatio-temporal resolution) gain owing to the

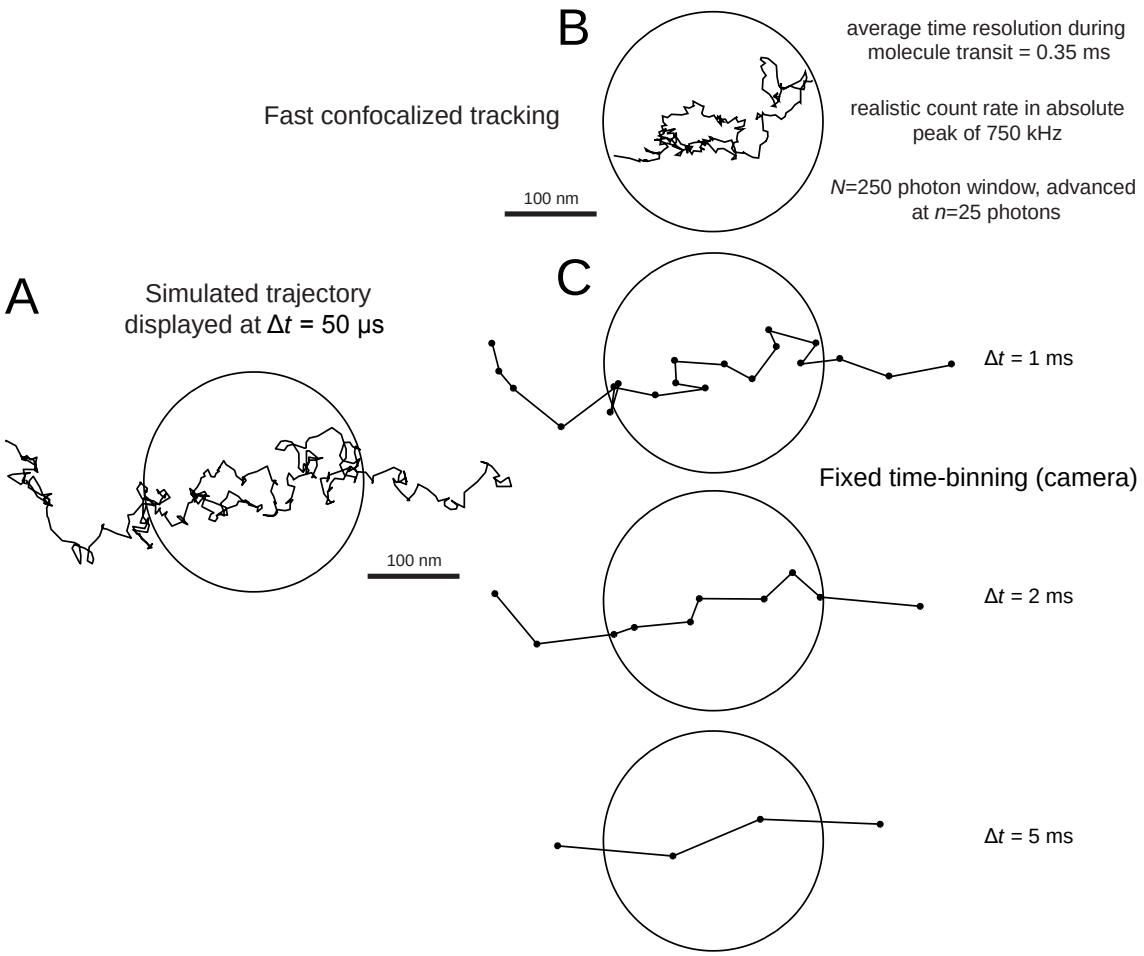

Figure 2.10: Sampling of molecular position at finite spatio-temporal resolution. (**A**) Simulated molecule trajectory (**B**) Trajectory obtained by fast confocalized tracking, employing the full photon stream. A realistic peak count rate of 750 kHz and an experimental reference map was used in the calculation. (**C**) Measured trajectories by camera-based tracking at fixed frame time. Photon collection during the whole frame is assumed. See text for details and discussion.

detection arrangement, the photon stream readily allows continuous sliding of the window of N photons yielding a localization in smaller increments (moving average). The displayed trajectory was obtained by shifting a $N = 250$ window in increments of $N/10 = 25$. Indeed, one may rationalize the moving average performed as being simply ten independent assessments of the identical trajectory, each shifted by a tenth of the effective time resolution. This enhanced mode will allow the assembly of histograms of steplength-vs-time statistics which feature a higher population than would be found in trajectories sampled 'only once' (no moving average). The obtained histograms (compare Figure 3.9B) thus exhibit lower noise (an enhanced statistical basis), while leaving extracted model parameters unaffected (Chapter 3). Naturally, only statistically independent photon windows may be compared in producing the histograms.

Detection of short-term lateral confinement

A focus of this thesis is the demonstration of nanoscale inhomogeneities in the diffusion of membrane-constrained molecules. While the causes of anomalous diffusion may be complex, and indeed there may be more than one responsible mechanism, such anomaly may include unambiguous instances of temporary arrest of lateral diffusion. That is, we would like to diagnose instances when the molecule undergoes confinement on the molecular scale, solely on the basis of spatiotemporal trajectories $(x(t), y(t))$. The sliding-scale (moving average) analysis provides better sampling of the start- and end-points of such traps. This is beneficial when trying to identify nanoscale confinement directly from the spatio-temporal trajectories (Chapter 3).

Excellent burst-selection

Binning groups of photons rather than photons during a fixed time interval also leads to a marked improvement in fluorescence burst recognition. As described in Chapter 3, the fluorescence intensity over time can be calculated on a sliding basis by combining N photons and determining their average arrival time as well as the average count rate during this interval. Such an analysis effectively flattens the periods of

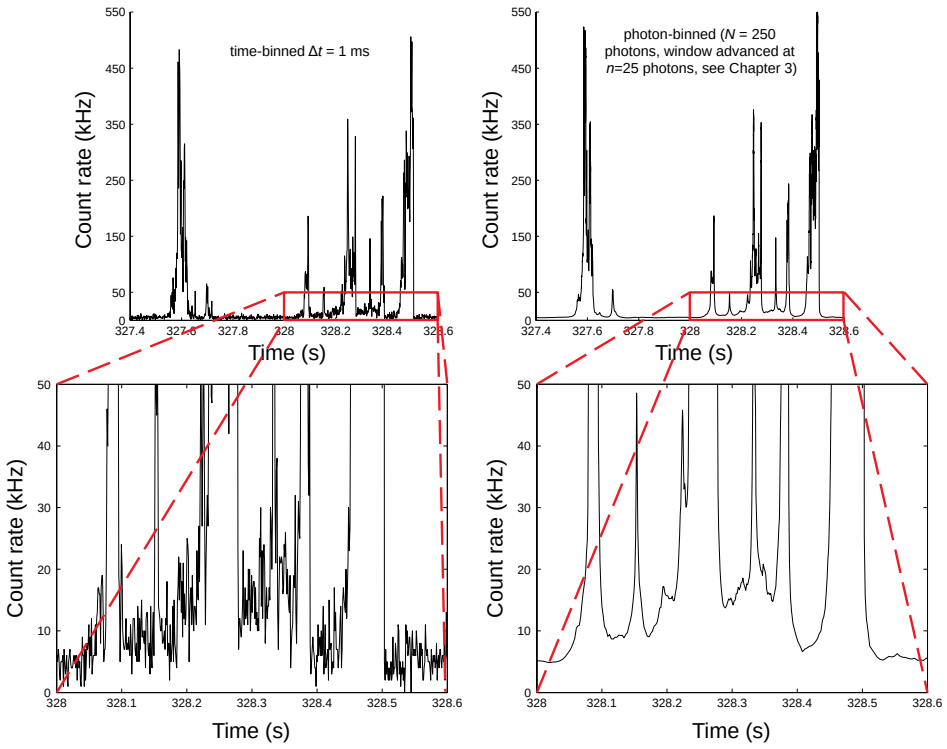

Figure 2.11: The photon-binned reconstruction of the signal intensity trace (right) features less noise than a trace of the same data binned in fixed time intervals $\Delta t =$ 1 ms (left). This allows a better identification of the start and end times of individual photon bursts. The photon-binned trace was constructed as described in Chapter 3, advancing a window of $N = 250$ photons by steps of $n = 25$ photons and computing the set $\{t_j, I_j\}$ for each window j.

background, as can be seen in Figure 2.11. This is advantageous, as bursts are identified by a thresholding criterion from this noise-freer trace (Figure 2.11).

General considerations of spatial vs. temporal accuracy

Our method offers flexibility when it comes to choosing appropriate spatial and temporal accuracies to track the molecular motion of interest. Evidently, there are limits to achieving both equally well. In-depth treatments of static and dynamic errors and their consequences in particle tracking experiments may be found in [51,52]. We note for our approach that, when using groups of N photons from our photon stream to yield positions, the effective temporal resolution Δt, i.e., the time between

two consecutive localizations, is given by $\Delta t \approx N/Q$, with Q the count rate. The localization is subject to a similar uncertainty of $\Delta A \approx A_{PSF}/N$, where A_{PSF} is the area of the detection PSF. It follows that

$$\Delta A \cdot \Delta t \approx \frac{A_{PSF}}{Q}, \tag{2.7}$$

i.e., the product of spatial localization accuracy and temporal resolution, is roughly constant in the experiment. $\Delta A \cdot \Delta t$ varies slightly over the observation area as the count rate from the molecule is highest at the center of our excitation profile. It is interesting to note that similar considerations apply to single-molecule-switching-based far-field optical nanoscopy schemes. By choosing an appropriate N, it is thus possible to balance the spatial and the temporal resolution as required. Fixing N prioritizes similarity in spatial accuracy amongst localizations and yields varying time separations, while a fixed integration time Δt leads to a variable localization accuracy depending on instantaneous count rate. Both approaches must converge to showing essentially the same diffusion properties. However, control over the spatial accuracy (by fixing N) has its advantages when studying portions of trajectories where little movement occurs, such as during 'trapping' (Chapter 3). In this particular case, time-averaging is only a negligible contributor.

Chapter 3

Membrane dynamics on the millisecond timescale: Lipids and proteins

A prominent problem that has benefitted from fast nanoscale tracking of single molecules is the dynamics of proteins and lipids in cellular membranes such as their organization into nanodomains, so-called "lipid rafts" [53–57]. Since their proposal, the question of the existence and functional role of such cholesterol-mediated lipid assemblies has caused much controversy [58–61]. Owing to the lack of suitable noninvasive techniques to detect these nanodomains in living cells, their spatial extent has been estimated at somewhere in the range of 5–200 nm [62], that is between molecular dimensions and the resolution limit of conventional fluorescence microscopy. Camera-based tracking of single lipids could provide more detailed insight [30,63,64]. However, so far it either lacked temporal resolution or it made use of rather large gold beads as lipid labels, implying that the measurements may not give comprehensive answers to the raised questions. Our experimental approach introduced in Chapter 2 is capable of following the fast lipid movements with minimal invasion. Therewith, nanoscale trapping of fluorescent lipid analogs in the plasma membrane of living cells was revealed. The area in which a single lipid dwells during trapping was shown to be smaller in diameter than 20 nm. The observed trapping took place on macromolecular scales

and was much more pronounced for a sphingo- than for a phosphoglycero-lipid, with average trapping times of about 15 ms and less than 4 ms, respectively. In contrast to camera-based lipid tracking experiments, our approach allows a flexible choice of spatial and temporal resolution and gives straight access to spectroscopic parameters. It may further reveal new details of biological problems where dynamical molecular nano-organization is crucial.

3.1 Organization of the cellular plasma membrane

3.1.1 The main players in the membrane

The plasma membrane of eukaryotic cells contains a large variety of different lipid species, which can be sorted into three different classes: glycero-phospholipids, sphingolipids and sterols. The first two classes, while consisting of a range of different lipids with saturated or unsaturated chains, differ mainly in the headgroups to which the two fatty acid chains are attached. Glycerophospholipids are based on glycerin, whereas sphingolipids are based on a ceramide backbone and have either a phosphocholine (Sphingomyelin, SM) or a complex carbohydrate structure headgroup (Glycosphingolipids, e.g. GM1). The ceramide backbone enables the sphingolipids to function as hydrogen bond acceptors and donors, whereas the glycerin is only a hydrogen bond donor [65,66]. The third class, the sterols, have a completely different structure, formed by a rigid four ring system. Cholesterol is the most abundant sterol in the cell membrane. The exact amount of these lipid classes can differ remarkably from cell to cell, but cholesterol is usually in the range of 30–40 mol % [67,68]. Sphingomyelin is present at 10–20 mol % and glycosphingolipids are found only in a few specialized cells in a significant amount [69]. Phosphoglycerolipids, gangliosides and proteins add up to a highly heterogeneous mixture. Independent of the exact lipid contents, cellular plasma membranes always form a bilayer structure, with an inner and an outer leaflet, serving as barriers to protect the interior environment from uncontrolled exterior influences. Both leaflets differ in their lipid composition: the outer leaflet contains most of the sphingolipids whereas the inner leaflet is enriched in the

phospholipids PI (phospatidylinositol) and PS (phosphatidylserine) [70]. This asymmetry is sustained by specific membrane proteins actively flipping the lipids from one leaflet to the other [71]. Cholesterol seems to be equally distributed in both leaflets due to its high rate of spontaneous flipping between the two leaflets (on the order of 1/s) [72].

3.1.2 Dynamical molecular complexes and 'lipid rafts'

Since this high degree of complexity in the organization of the plasma membrane is not a prerequisite for the formation of a stable bilayer, whose formation is already observed with just a single amphiphilic lipid, it has long been proposed that the complexity of the composition of the membrane is reflected in a structured lateral organization of the membrane by macro- and microdomains [53, 70, 73]. Examples for such domains are clathrin-coated pits, caveolae, cilia and microvilli, all containing a specific set of proteins and lipids [55]. Putative 'rafts' are a special kind of microdomains, supposedly enriched in sphingolipids and cholesterol, as first argued by Simons et. al. [53] (Figure 3.1). It is assumed that they are distributed over the whole outer leaflet of the plasma membrane, playing a vital role in various important cellular functions such as signalling, cell apoptosis, cell adhesion and migration and synaptic transmission. One proposed way by which 'rafts' succeed in influencing biological processes is by separating the cell membrane into small sub-areas, thereby providing an environment to assemble special proteins in such areas ('assemblage potential'). A prominent and widely studied example are glycosyl-phosphatidylinositol (GPI) anchored proteins, which have been found to be associated with sphingolipid-enriched domains [55, 74]. Although intensively studied in a large body of work (see [56, 58, 75] for discussion and review), there is still a controversy as to whether 'rafts' indeed exist and, if so, as to what exact role they play in the organization and function of the eukaryotic cell. Two of the major obstacles for the direct investigation of 'rafts' in living cells are the highly dynamic nature of the plasma membrane with lipid diffusion coefficients on the order of $D \approx 1\mu\mathrm{m}^2/\mathrm{s}$, which results in observation times of $\sim$10–30 ms for a confocal fluorescence microscope as well as the subdiffraction size

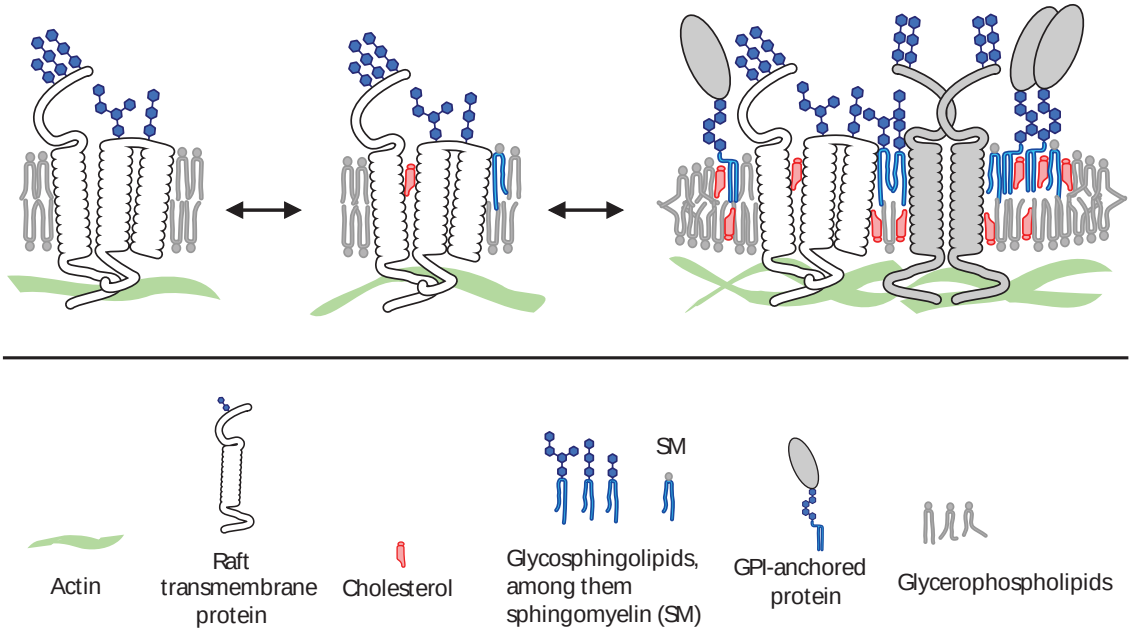

Figure 3.1: Nanoscale assemblies of certain lipids and proteins mediated by cholesterol ('lipid rafts') are thought to play a functional role in many membrane-associated processes. Membrane proteins bind and/or enrich certain lipids through chemical and physical specificities. These lipids may themselves exhibit sphingolipid/sterol assemblage potential. In this scheme, a TM raft protein (white) specifically interacts with cholesterol and sphingomyelin (SM), an interaction that lubricates its inclusion to and the assembly of functionalized (coalesced) raft membrane (constituents shown in gray). Figure adapted from [75].

of those microdomains (certainly <200 nm) [56]. These 'raft' properties place great demands on the experimental setup and method used for their investigation, since they have to provide a high spatial and temporal resolution while simultaneously being live-cell-compatible. This calls for novel measurement instrumentation of the kind introduced in this thesis.

Since the initial proposal of 'rafts' [53], a whole range of biochemical and biophysical methods have been applied to native as well as artificial model membranes to prove their existence and investigate their properties. The most widely used method for 'raft'-studies is based on the fact that parts of the plasma membrane are resistant to the membrane dissolving detergent triton X-100 at 4 degrees centigrade and that those parts are enriched in cholesterol and sphingolipids, while phospholipids show no preference. This has led to the conclusion that those resistant parts form small

domains in the cellular plasma membrane [53, 76, 77]. However it was subsequently discovered that this method is prone to many different artifacts, including structural changes in the plasma membrane induced by the unphysiological extraction temperature and by the detergent itself [78]. For this reason the membrane content which is found to be resistant to the extraction procedure is today referred to as 'detergent resistant membranes' (DRMs), which acknowledges the fact that those fractions may only partly represent a physiologically meaningful component of the membrane. Studies on model membranes in general have shown the ability of bilayers to separate into different phases and form microdomains if the right amounts of cholesterol (20–30 %) and sphingolipids are present [79, 80]. These microdomains have sizes ranging from the nanoscale [81,82] to the microscale [79], depending on their lipid content, and are therefore within the reach of a standard confocal fluorescence microscope. However, domains of this size are not present in cell membranes. This is a remarkable observation because the amount of cholesterol in the plasma membrane would be high enough (30–40 %) for larger stable domains to form. One caveat associated with such model membrane systems is the inherent need to use a simpler molecular composition than is found in a real membrane system of the cell. This is especially true of the protein content of native membranes which, according to theoretical consideration, might be responsible for the absence of such giant 'rafts' in native membrane systems [83].

Investigations of 'rafts' *in vivo* (cell tissue culture) are mostly based on common fluorescence techniques, such as FCS [79, 84], Förster resonance energy transfer (FRET) [85] and FRAP [86,87]. The limitations of FRAP and FCS have been briefly explained in the first chapter. FRAP averages diffusion behavior over large areas of at least the diffraction limit of the light. FRET may be used to probe molecular interactions at very small (nm) distances but delivers little information about the possible wider translational dynamics, such as the path taken by a molecule before and after such an interaction. This technique also requires high non-endogenous label concentrations. Single molecule tracking also has great potential to shed light on the involved molecular processes [63]. However, the previously discussed limitations in spatio-temporal resolution have hampered its successful application to this experimentally demanding problem, especially for small non-invasive dye labels.

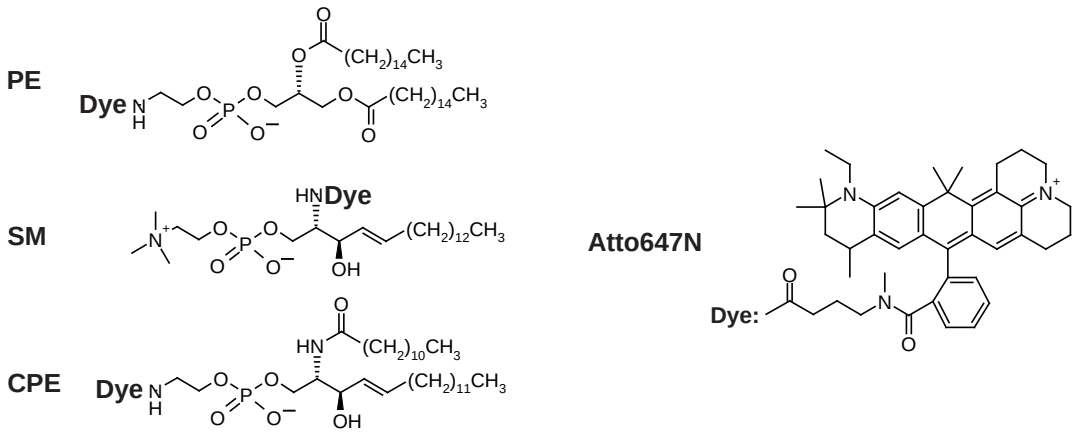

Figure 3.2: Structural details of the different fluorescent lipid analogs and the lipophilic organic dye Atto647N.

Previous studies show contradictory results, ranging from findings of heavily clustered lipid protein domains to totally random-distributed domain components. Even the studies which identified microdomains report widely differing diameters (25–700 nm), which can be merely a side effect of the different spatial resolutions of each of these methods [56]. Further, it was shown that certain types of lipids interact specifically with membrane proteins by forming 'lipid shells' [88]. While the organization and properties of such shells are still unknown, it is highly probable that cholesterol and sphingolipids play an important role in the formation of those entities.

3.2 Tracking lipids and small proteins

Lipid labeling of a phosphoglycero-lipid (phosphoethanolamine, PE) and of a sphingolipid (sphingomyelin, SM) by the hydrophobic organic dye Atto647N was the same as described in [89]. The fluorescent lipid analogs were inserted into the plasma membrane of living PtK2 cells by incubation with lipid-BSA-complexes [89] (Figure 3.3).

Control experiments ensured a concentration of the fluorescent lipids low enough for single-molecule measurements (Figure 3.4). We placed the focus at random positions in the lower plasma membrane facing the cover slip and completed all measure-

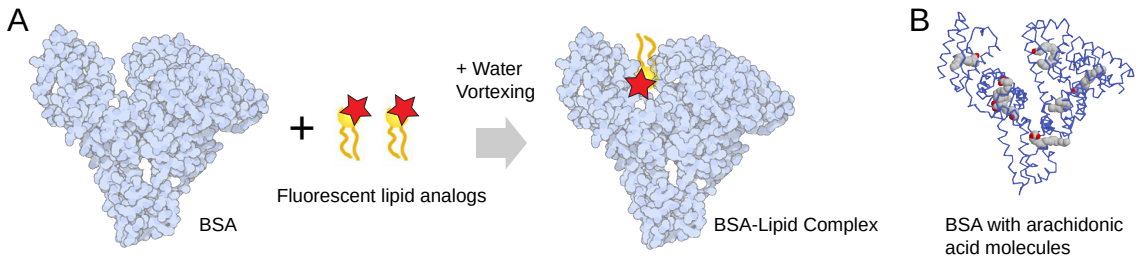

Figure 3.3: (**A**) Membrane incorporation of fluorescent lipid analogues by Bovine Serum Albumin (BSA) complexes. Efficient insertion of fluorescent lipids was verified by BSA washing experiments (to be published). (**B**) Structural information on BSA, to which the lipid analog attaches.

ments so swiftly (<30 minutes) that no significant internalization or morphological changes in the cell could take place. Flat membrane regions remote from the central nucleus and discernible organelles were chosen to minimize the unwanted background. The present experiments were performed in cell medium at ∼23 degrees centigrade. Lowering of the plasma membrane's cholesterol content was realized by cholesterol oxidase (COase) treatment [89]. For free diffusion controls we measured PE in a supported lipid bilayer (SLB) model. Excellent signal-to-background ratios of 200 and above were obtained for the single-lipid transits (Figure 2.3A). Having count rates of up to 1 MHz for molecules passing the center of the excitation spot, we chose $N = 250$ photons as a good compromise between experimental localization error and temporal resolution. Instantaneous count rates directly determine the effective temporal resolution, which is thus <1 ms and for much of the trajectory <0.5 ms.

3.2.1 Experimental details

We immobilized fluorescent crimson beads of mean diameters 24 nm and 40 nm (Invitrogen) for testing the localization accuracy and for recording the reference map. The beads were immobilized on coverslips with poly-L-lysine (0.1 % wt/vol in water) solution and embedded in Mowiol. Sparse bead preparation enabled the imaging (localization) of individual beads. Supported lipid bilayers were prepared as in Chiantia et al [94]. We used the lipophilic organic dye Atto647N (excitation and

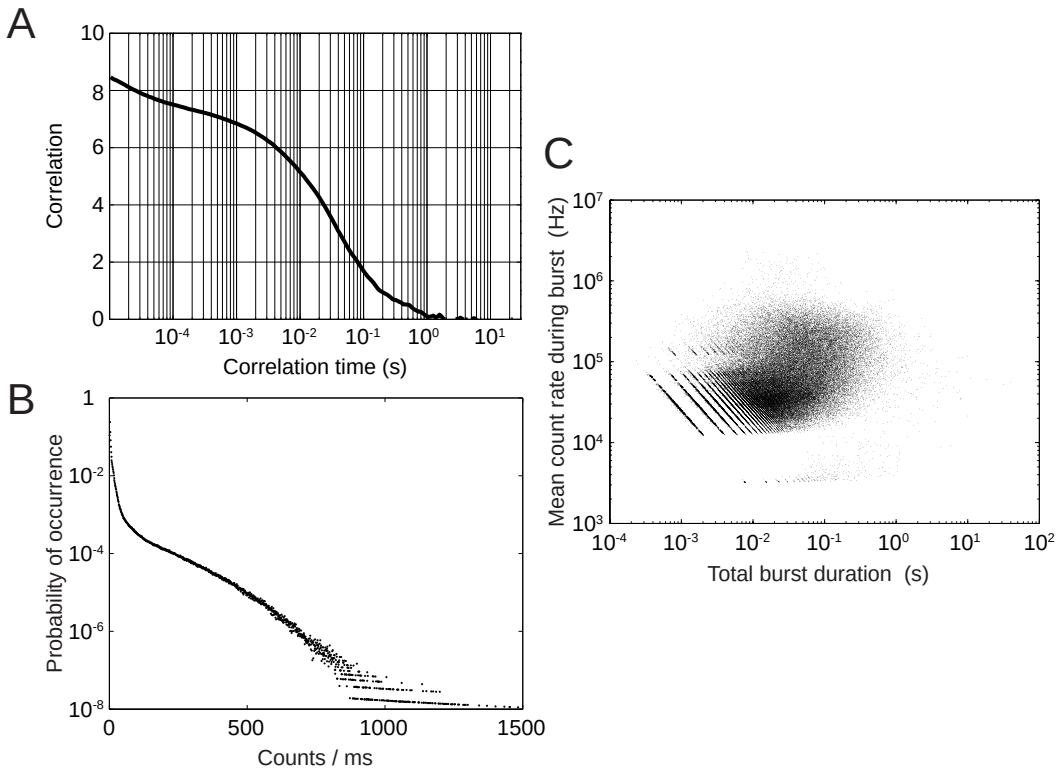

Figure 3.4: Control of the true single-molecule measurement as required for the fast tracking method. (**A**) Typical auto-correlation [90] of a time-trace of single photon data from SM diffusion in the plasma membrane of living cells (excitation power of 15–20 μW). The characteristic diffusion time ($\sim$30 ms) is similar to previous measurements [89]. The correlation amplitude demonstrates that the average number $M \approx 0.13$ of molecules in the focal volume is significantly below unity; i.e., the probability to detect more than one molecule at a time is very low ($< 1\%$) [91]. (**B**) Probability distribution of photon counts of the same photon data. An analysis based on fluorescence intensity distribution analysis (FIDA) [92] results in $M \approx 0.07$ (i.e., a probability of 0.6 % to detect more than one molecule at a time) and demonstrates an excellent signal-to-noise ratio of $\sim$40 (averaged over all large and many small fluorescence bursts). While FIDA takes any background signal due to, for example, laser scattering into account, the background signal leads to a reduction of the correlation amplitude [93]. Consequently, the value of M determined by FCS is slightly larger than that determined by FIDA. (**C**) Scatter plot of the value pairs of burst brightness (mean count rate during burst) vs. burst duration for 109,417 lipid transits (PE, SM, SM-COase, CPE) in living cells. No significant signature of multimolecular events or events stemming from bright vesicles is observed, such events would be characterized by larger values of burst brightness. Note that the mean count rates shown here are obtained over the entire duration of the bursts, including the initial and final segments where the signal is small. For the central portion of trajectories [in the region of analysis (diameter of typically 240 nm), the count rates are higher and reach 600–1,000 kHz]. The pattern emerging for small value pairs of count rate and burst duration stems from the burst selection criteria. (Bursts contain integer multiples of 25 photons).

emission maxima at 645 and 670 nm, respectively; Atto-Tec) as a marker in all experiments, whose structure has been determined in [89]. We applied the fluorescent lipid analogs phosphoglycero-lipid N-(Atto647N)-1,2-dipalmitoyl-sn-glycero-3-phosphoethanolamine (PE, Atto-Tec) and the sphingolipid N-(Atto647N)-sphingosyl-phosphocholine (N-Atto647Nsphingomyelin, SM, Atto-Tec). While PE is labeled at the head group, i.e., in the water phase, SM is labeled at the water-lipid interface, by replacing the native long acyl chain with a short acyl chain carrying the dye. We also applied a head-group labeled sphingomyelin (N-dodecanoylsphingosyl-[N0-(Atto647N)-phosphoethanolamine] (Atto647N-ceramide-phosphoethanolamine, CPE, Atto-Tec). The structures are given in Figure 3.2.

Photostability of the fluorophore

Plotting the entry and exit points of ∼20,000 trajectories shows that most points reside on the periphery of the observation area (Figure 3.5). However, because of the burst selection criteria, some of the entering molecules are first localized well on their way toward the center and some will not leave the observation area at the very edge. Comparing the number of nonperipheral localizations upon entry and exit reveals that about 2–3 % of the fluorophores are bleached during the transit. Consequently, we have chosen a low enough excitation power so that the influence of bleaching is sufficiently small, allowing a bias-free statistical analysis of molecular diffusion and trapping.

3.2.2 Statistical trajectory analysis: The distribution function of square displacements

The statistical analysis of the sets of trajectories we obtained by our method is designed to take into account the nontrivial diffusion behavior expected for membrane constituents in a living cell. Notably, an earlier dynamical study by STED nanoscopy [89,95] revealed non-Brownian behavior for sphingolipids, with indications of much lower anomaly for phospholipids and for sphingolipids in cholesterol-depleted (COase-treated) membranes. This is fully confirmed by the mean squared displace-

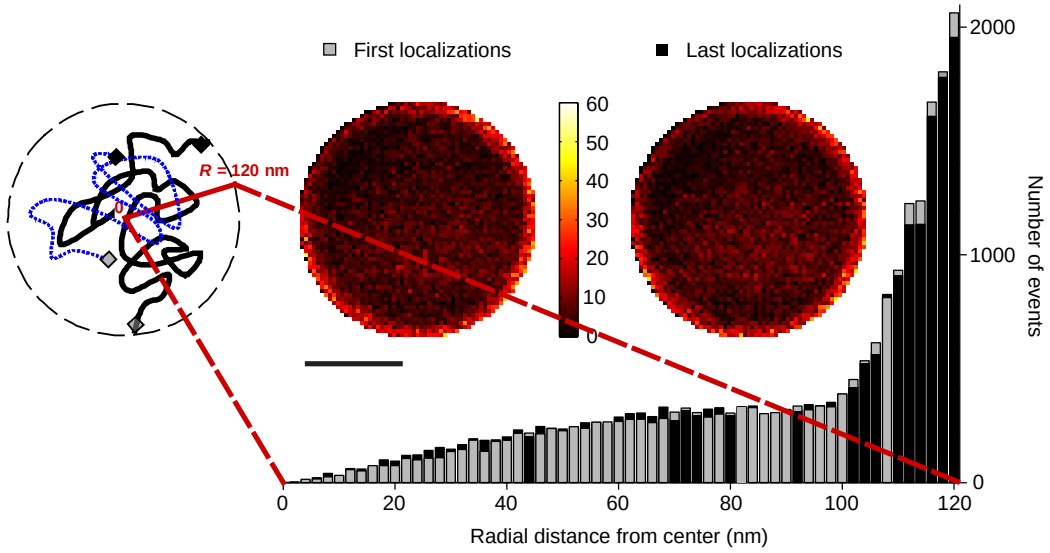

Figure 3.5: Photostability of the fluorophore. The large majority of first and last points localized for $\sim$ 20,000 trajectories (SM lipids in living cells, excitation power of 15–20 μW) lie on the periphery (Insets). However, as a result of the burst selection criteria, some of the entering and leaving molecules are localized near the center. A slightly higher number left the observation area near the center. This small fraction (2–3 %), most probably stemming from molecules lost from the observation due to irreversible photobleaching, is low enough to exclude a significant biasing effect of photobleaching on our single-molecule tracking data. (Scale bar, 100 nm.)

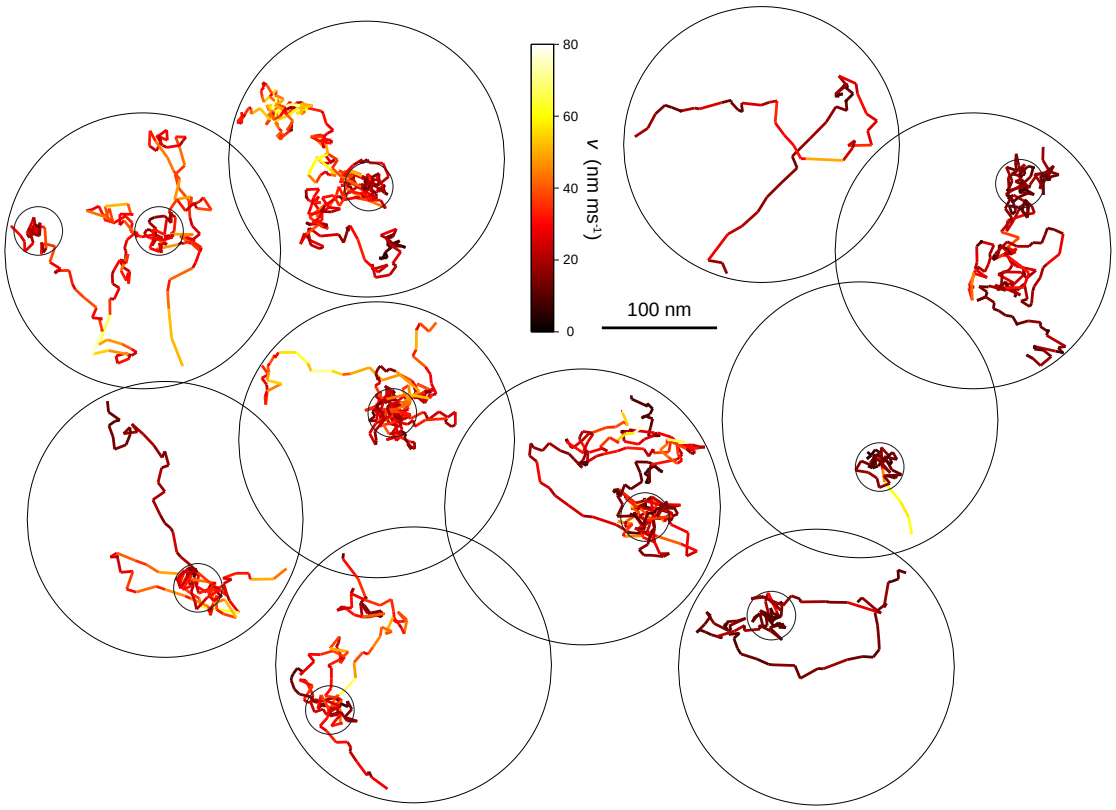

Figure 3.6: The live-cell trajectories (examples of sphingomyelin (SM) are shown) reveal complex and highly heterogeneous behavior. Many hundred up to > 1000 trajectories are obtained in a typical 10-minute recording. Their combined analysis allows statistical evaluation and assessment by diffusion models.

ment (MSD) of our tracking data (Figure 3.9).

Rather than relying on the MSD, we build our analysis on the cumulative probability of square displacements [96]. This approach allows us to superpose several, here two, regimes of diffusion and to determine their relative presence in the translational motion of the molecules. The lateral diffusional motion of a particle in a medium characterized by a diffusion constant D is described by Fick's second law:

$$\frac{\partial}{\partial t}p(r,t) = D \cdot \nabla^2 p(r,t) \tag{3.1}$$

with the two-dimensional Laplacian operator ∇^2. $p(\vec{r},t)d\vec{r}$ describes the probability that a particle will be detected within the area $[\vec{r}, \vec{r}+d\vec{r}]$ at a time t. For a particle

that starts at the origin at time 0, the solution of Equation 3.1 in r^2 yields

$$p(r^2,t)\,\mathrm{d}r^2 = \frac{1}{r_0^2}\exp\left(-\frac{r^2}{r_0^2}\right)\mathrm{d}r^2 \tag{3.2}$$

with $r_0^2(t) = 4Dt$ [88]. By integration, the cumulative distribution function for the square displacements r^2 is calculated:

$$P(r^2,t) = \int_0^{r^2} p(\rho^2,t)\mathrm{d}\rho^2 = 1-\exp\left(-\frac{r^2}{r_0^2}\right) \tag{3.3}$$

We will assemble histograms of the steplength-vs-time statistics and therefore count pairs of steplengths and time separations between localizations over defined intervals Δt and Δr^2. $P(\Delta r^2, \Delta t)$ shall thus denote the probability that a single-molecule will be found within a circle of radius Δr from its starting point after a time Δt. Typically, 300–3,000 trajectories are identified from a photon trace recorded for 5–10 min. Each trajectory represents a sequence of spatial positions $\vec{r}(t)$ localized for N= 250 consecutive detected photons of a selected single-molecule burst. From $\vec{r}(t)$, a set of values for the square displacements,

$$\Delta r^2(\Delta t) = \left(\vec{r}(t+\Delta t) - \vec{r}(t)\right)^2$$

between two localizations separated by variable time lags Δt is obtained. With the corresponding set of time lags Δt, we may then construct a discrete probability density $p(\Delta r^2, \Delta t)$ by counting the number of square displacements between Δr^2 and $\Delta r^2 + \Delta(\Delta r^2)$ and Δt to $\Delta t + \Delta(\Delta t)$. Single-photon information allows us to shift the time observation window in steps that are smaller than the temporal resolution, yielding more points and thus improved statistical significance. We can rule out bias by this 'sliding-scale' analysis because we obtained similar results with an analysis including discrete time-resolution increments only.

As a result of the finite observation radius R, in our implementation typically 120 nm, short step-lengths are reproduced more often than long ones. Naturally, the longest trackable step goes across the entire region with length $2R$. We account for this reduced probability of observing long steps by correcting with the probability

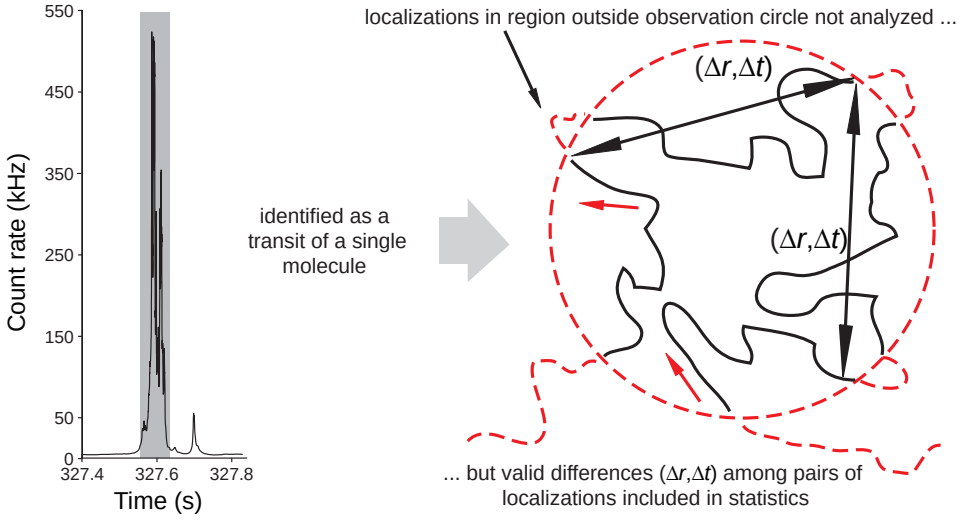

Figure 3.7: Trajectory analysis for a circular observation area. A molecular trajectory identified from a single-molecule fluorescence burst (left) may reach the border of our observation area (the central circle of 240 nm diameter), briefly exit from it and return (schematic). Given the prior assumption that the burst contained one molecule and that the molecule has not left the more widely interpreted focus, displacement vectors and longer time lags $(\Delta r, \Delta t)$ to the localizations upon return may still be included in the steplength-vs-time statistics.

$P_{track}(\Delta r, R)$ of detecting a step of length Δr for which both the initial and the end point lie within the circle of radius R. P_{track} is equivalent to the convolution (overlap integral) of two circles with radius R and center-to-center distance Δr (Figure 3.8), that is

$$P_{track}(\Delta r, R) = \frac{2}{\pi} \arccos\left(\frac{\Delta r}{2R}\right) - \frac{\Delta r \cdot \sqrt{4R^2 - (\Delta r)^2}}{2\pi R^2} \tag{3.4}$$

We divide the probability density $p(\Delta r^2, \Delta t)$ by $P_{track}(\Delta r, R)$ before cumulation and normalization of the distribution. Trajectories leaving the central 240 nm diameter area for a short time may still contribute displacements at longer time lags to the analysis as they stem from one and the same molecule (Figure 3.7).

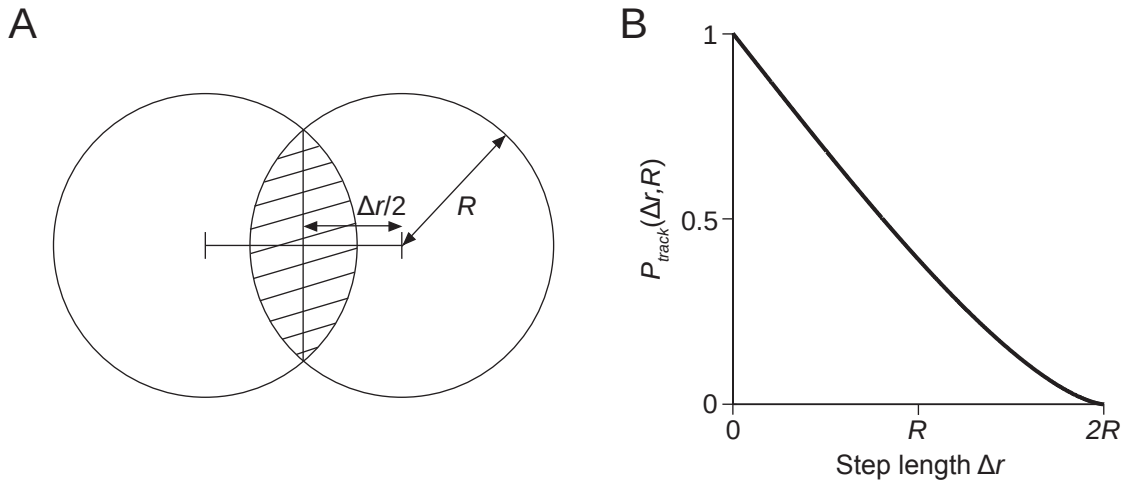

Figure 3.8: Calculation of the correction factor for a finite observation area πR^2. We compute the probability $P_{track}(\Delta r, R)$ of detecting a step of length Δr for which both the initial point and the end of the displacement vector lie within the circle of radius R. This probability is equivalent to the convolution (overlap integral) of two circles with radius R and center-to-center distance Δr, as depicted in (**A**). We therefore determine the proportion of the joint area segment to the area of one of the circles. By simple trigonometry, we obtain the expression of Equation 3.4, which is plotted in (**B**) for $0 \leq \Delta r \leq 2R$. We correct the probability density $p(\Delta r^2, \Delta t)$ by $1/P_{track}(\Delta r, R)$ before cumulation and normalization along Δr^2 to yield the cumulative probability $P(\Delta r^2, \Delta t)$.

Detailed description of the analysis

Definition of accuracies. Throughout this thesis, we applied the conventional definition of the standard deviation σ of a distribution of n values x_i: $\sigma = \left(\frac{1}{n-1}\sum_{i=1}^{n}(x_i - \bar{x})^2\right)^{1/2}$, where $\bar{x} = \frac{1}{n}\sum_{i=1}^{n} x_i$. In the case of normally distributed values the diameter of the distribution may be estimated by the full-width-at-half-maximum $FWHM = \sigma\sqrt{(8\ln 2)}$, which is the diameter of the area containing 50% of all localizations.

Our single-molecule tracking analysis resulted in the physical characterization of lipid diffusion in a given system by extracting the diffusion constant D, the time-fraction of free diffusion α and an estimate of the radius r_{trap} of the trapping area. The analysis programs were implemented in MATLAB, with a few C subroutines.

The analysis steps were as follows.

- For each detected photon i we recorded a value pair $\{t_i, c_i\}$ of the photon arrival time t_i (absolute time with respect to the start of the measurement) and of the detector channel c_i.

- The photon events were consecutively binned into windows of $N = 250$ (or 1,000) photons, and the windows were advanced in steps of $N/10 = 25$ (or 100) photons. A set of four parameters $\{t_j, I_j, x_j, y_j\}$ was obtained for each photon window j: the time t_j is the average time $\langle t_i \rangle$ of the arrival times t_i of all N included photons; the average signal intensity

$$I_j = \frac{N}{t_N - t_0}$$

  (where t_0 and t_N are the times before the first and of the last included photon, respectively); and the spatial position (x_j, y_j) determined from three photon count values S_1, S_2 and S_3 in channels 1 to 3. This triple $\{(S_1, S_2, S_3)\}$ is compared to the reference map to find the coordinates (x_j, y_j) where it best matches the reference triple $\{(R_1, R_2, R_3)\}$ encoding the relative detection efficiencies. The best agreement of (S_1, S_2, S_3) with respect to $\{(R_1, R_2, R_3)\}$ is determined by the maximum-likelihood scheme outlined in Section 2.3.1.

- The bursts (i.e., molecular transits) were identified as those elements of the set $\{t_j, I_j, x_j, y_j\}$ for which

$$I_j > \text{threshold} = 5\mathrm{B} + 5\frac{\mathrm{B}}{\sqrt{\mathrm{N}}},$$

  where B is the uncorrelated offset signal (background) during the measurement, which was determined from the intensity distribution (see Figure 3.4).

- For each burst, the sequence of all positions within a confidence circle, i.e, within the central focal diameter of typically 240 nm make up the molecular trajectory $\vec{r}(t) = \{x_j, y_j\}\,(t_j)$.

- All statistically independent (nonoverlapping) mutual differences $\{\Delta r^2, \Delta t\}$ were calculated from $\vec{r}(t)$.

- Counting the numbers of $(\Delta r^2, \Delta t)$ falling within increments $\Delta(\Delta t) = 0.1$ ms and $\Delta(\Delta r^2) = 50$ nm^2 up to $\Delta t = 10$ ms yielded the probability density $p(\Delta r^2, \Delta t)$. Each count is weighted by the inverse intensity $1/I_j$, i.e., the time between adjacent localizations, to account for the variable time steps.
- Correcting of $p(\Delta r^2, \Delta t)$ by $1/P_{track}(\Delta r, R)$ (Figure 3.8), cumulating and normalization along Δr^2 yielded the cumulative distribution $P(\Delta r^2, \Delta t)$.
- Global fit to a model function in order to extract the diffusion parameters.

The mean-square displacement (MSD) was computed as the expectation value of the square displacement $\langle \Delta r^2 \rangle$ for lag times Δt from $p(\Delta r^2, \Delta t)$. The deviation from linear behavior starting at $\sim (95\text{nm})^2$ (seen for SLB, Figure 3.9) is due to the finite area of observation ($R = 110$ nm in this case).

3.2.3 Experimental results: Hindered diffusion

Computing the cumulative probability $P(\Delta r^2, \Delta t)$ in this way, with increments $\Delta(\Delta t) = 0.1$ ms and $\Delta(\Delta r^2) = 50$ nm^2, reveals marked differences for both lipid classes (Figure 3.9B). While PE diffuses and thus explores space quickly, i.e., $P(\Delta r^2)$ flattens with longer lag time, SM shows a clear signature of dominant trapping interactions and much less development of the spatial part of the distribution with growing lag time. Depletion of cholesterol by COase treatment reduces the trapping of SM, rendering its diffusional behavior similar to PE. The supported lipid bilayer control measurements exhibit free diffusion without obstacles as expected.

In assessing our data further, we chose the simplest possible physical model. It contains a mobile regime, represented by free Brownian motion with a characteristic diffusion coefficient D and a stationary regime during which the particle merely stays trapped at a fixed location.

The cumulative probability $P(\Delta r^2, \Delta t)$ then takes the form [96, 97]

$$\begin{aligned} P(\Delta r^2, \Delta t) &= \alpha \left[1 - \exp\left(\frac{-\Delta r^2}{4\sigma_r^2 + 4D\Delta t} \right) \right] \\ &\quad + (1-\alpha) \left[1 - \exp\left(\frac{-\Delta r^2}{4\tilde{r}_{trap}^2} \right) \right], \end{aligned} \tag{3.5}$$

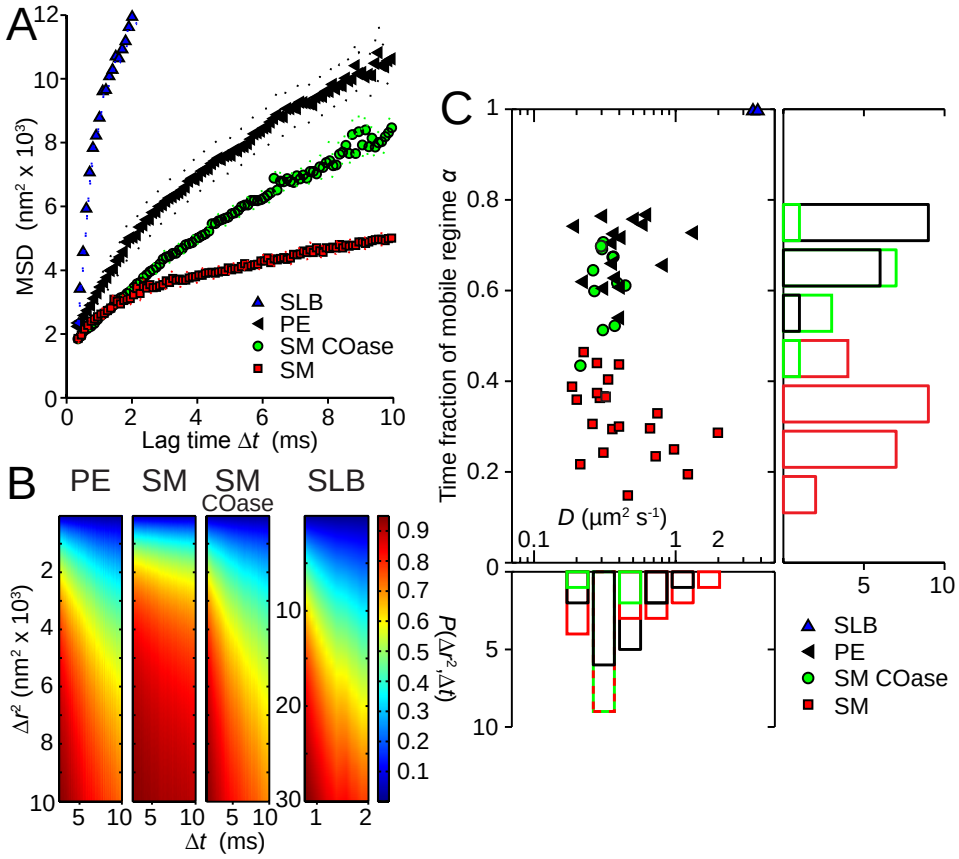

Figure 3.9: Diffusion of small organic dye labeled lipids in the plasma membrane of living mammalian cells. (**A**) Mean-square displacement (MSD) vs. time lag Δt along trajectories for Atto647N-labeled lipids diffusing in a supported lipid bilayer (SLB) and in the plasma membrane of live mammalian PtK2 cells. The examples show PE, SM and SM after COase treatment. The deviation from a linear dependence $MSD(\Delta t)$, indicating non-Brownian motion, is lowest for PE and largest for SM. The deviation from linear behavior starting at $\sim(95\text{ nm})^2$ for SLB is due to the finite observation area (of radius $R = 110$ nm in this case). (**B**) Typical examples of the cumulative probability $P(\Delta r^2, \Delta t)$ as a function of time lag Δt and squared displacement Δr^2 for all cases. Number of trajectories: 972 (PE), 2518 (SM), 2879 (SM-COase), and 1764 (SLB). The faster the lipid diffuses, the quicker it explores space, i.e., the more $P(\Delta r^2)$ flattens with longer lag time. SM shows a clear signature of dominant trapping, which is substantially reduced after COase treatment. (**C**) Results of global fits to $P(\Delta r^2, \Delta t)$ to a model containing a freely diffusing and a strictly stationary regime. The fraction of time a spent in the mobile regime differed substantially between PE and SM. PE was largely mobile, though did show short trapping, while SM was frequently trapped and remained in the stationary regime for most of the time. Cholesterol depletion by COase treatment led to higher mobility of SM. Values of SM-COase vary more strongly as the COase impact is somewhat variable.

where α is the (time-)fraction of the free diffusion regime, σ_r is the experimental localization error, and $\tilde{r}_{trap}$ is a parameter allowing an estimate of the radius

$$r_{trap} = \left(\tilde{r}_{trap}^2 - \sigma_r^2\right)^{1/2}$$

of the area within which the trapping interaction takes place. The molecule in this model can, at any time, either be stationary or mobile. The results of global fits to the cumulative distribution of each dataset yielded the values as shown in Figure 3.9C. In agreement with the previous STED data [89, 95], D varies in the range of 0.3–0.5 μm^2/s, and the time fractions of the two regimes differ significantly for the two classes of lipids. SM is dominated by the trapped regime ($\alpha \approx 0.3$), while PE is largely mobile ($\alpha \approx 0.7$) and SM under cholesterol depletion by COase nearly reaches PE characteristics ($\alpha \approx 0.65$); i.e., trapping is strongly reduced. The supported lipid bilayer measurements yielded the result for free diffusion: $\alpha \approx 1$, as anticipated.

The values of $\tilde{r}_{trap} = 20$ (SM), 22 (PE), and 21 nm (SM-COase) extracted from the global fits help us to give an estimate of the maximum range over which the molecule moves during the trapping. They are in the same range as the localization accuracy $\sigma_r = 19$ nm, which was consistently found for our experiments on the moving objects. This demonstrates very localized trapping interactions with crude estimations of $r_{trap} \leq 10$ nm (Table 3.1). The inferred trapping radii r_{trap} may contain either a true lateral degree of freedom within a finite-sized trap, but more likely reflect – at least in part – motion of the trap-lipid complex during trapping. In any case, they reveal that trapping occurs on macromolecular scales and is possibly caused by transient molecular complexes such as lipid-protein interactions.

To ensure that the dye label had no observable influence on the dynamic behavior of the lipids, two types of sphingomyelin were tested. The first one was labeled by replacing the native long acyl chain with a short acyl chain carrying the dye (see SM). The second type was labeled at the head group, i.e., in the water phase (Figure 3.2). Both types were characterized by the same diffusion constant D, the same time fractions α as well as the same trapping radius r_{trap}. These findings are in line with the observations of the previous STED-FCS measurements [89]. One could speculate that an elevated excitation power may result in increased photobleaching,

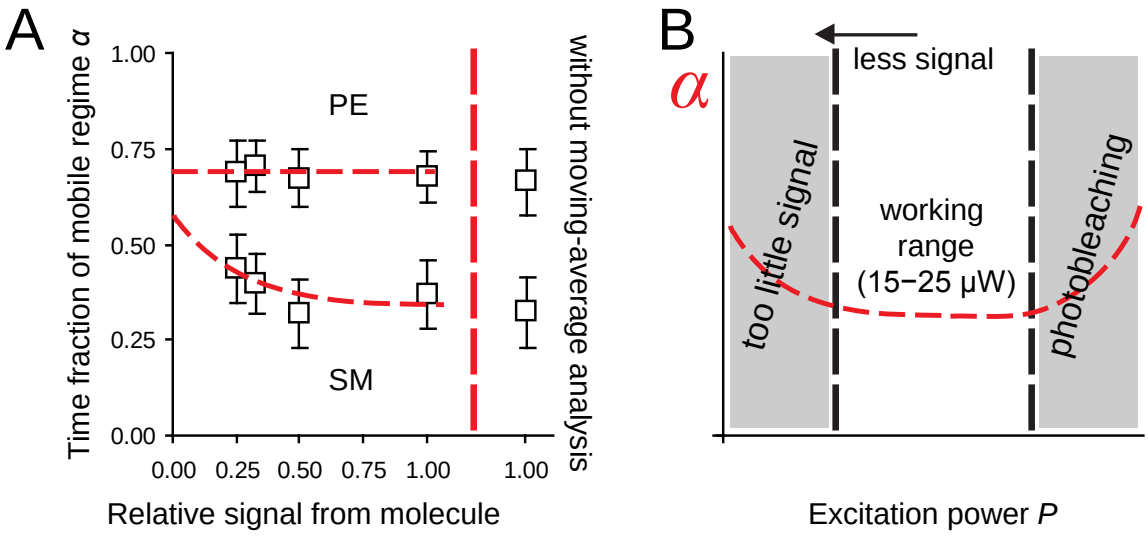

Figure 3.10: Detection of diffusion anomaly at lower signal. (**A**) A certain fraction of photons were discarded from the photon stream at a uniform probability (computationally imitating a neutral density filter – this is as if the photons had never reached the detector). At smaller signal, the time-fraction of free diffusion α for sphingomyelin (SM) increases (red lines are a guide to the eye), as the localized trapping is no longer well resolved due to a lack of molecular signal. Performing the analysis without the sliding scale did not noticeably alter α. (**B**) Tracking experiments with single molecules, which may irreversibly photobleach and be lost from observation, must operate in the right range of excitation power. Too low an excitation power P and thus signal leads to a decrease of spatio-temporal resolving capability and therefore a loss of information. The expected behavior of the extractable α is schematically shown. On the other hand, increasing the signal by increasing P is challenged by photobleaching. α is expected to increase.

which should compromise the recording of long traces of trapped lipids [95]. This may lead to an overestimation of the (time-)fraction α of the free diffusion regime. We have tested our method at various levels of excitation power (5–20 μW, i.e., intensities of 5-20 kW/cm^2) and applied other approaches, such as FCS, to ensure that our results are not notably altered by photobleaching.

On the other hand, as for single-particle tracking in general [30, 46–49], too low a brightness of the single molecules, which in our case may result from too low an excitation power, also leads to an overestimation of the values of α because short traps can no longer be discerned from free diffusion (compare Figure 3.10). Consequently,

we have chosen a laser power of 20 μW to elicit strong fluorescence response whilst keeping photobleaching at a minimum. Since the values of α gained with our method in any case represent upper bounds, one can be confident that trapping occurs to at least the measured degree and that major differences between SM and PE diffusion are present.

3.2.4 Nanoscale trapping

We performed an alternative ('magnifying') analysis based on the direct examination of individual trajectories. For free Brownian diffusion, as the lag time increases, it becomes increasingly unlikely that a molecule has not left a small circular domain. For a domain of diameter d = 60 nm, more than 97 percent of all molecules will have left the domain after Δt = 15 ms by Brownian motion, given the known diffusion constant D of the membrane lipids (alternatively, Δt = 3.7 ms for d = 30 nm).

Focusing on the spatial extent of long traps (Figure 3.11), we declared those instances where the lipid still resided inside the circular domain after Δt as transient traps and approximated the extent of the trapping area by determination of the radial standard deviation $\tilde{r}^*_{trap} = (\sigma_x \cdot \sigma_y)^{1/2}$ of the set of all localizations during this time. Potential traps were identified by moving a circular subdomain of diameter d (the "magnifying glass") over the trajectories (step size $d/2$ in the x- and y-direction). Each time the criterion "lipid remains within the domain area $\pi(d/2)^2$ for longer than Δt" was satisfied, we recentered the circular subdomain in two iterations on the center of mass of the localizations, so as to ensure that the trap is roughly centered and that traps are not cut into parts. The standard deviation $\tilde{r}^*_{trap} = (\sigma_x \cdot \sigma_y)^{1/2}$ of the present trap was then saved and its section of the trajectory excluded from further analysis to avoid multiple counting of the identical trapping event. An advantage of concentrating only on trapped events is that it allows us to increase the number of photons used for spatial localization to N = 1,000 and thus to increase the localization accuracy to σ^*_r = 4.2 nm. The histogram in Figure 3.12A shows the distribution of determined values of $\tilde{r}^*_{trap}$ of 8,724 selected trajectories of SM for a photon binning with N = 1000 photons (d = 30 nm). From the average value of

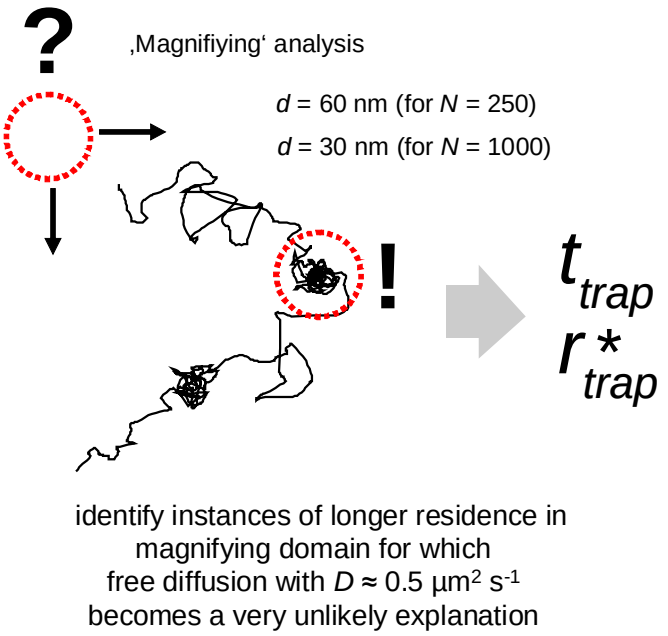

Figure 3.11: Traps (schematic) may be identified directly by a computer program searching for instances where the molecule remained unusually long in one place. The spatial extent and durations of trapping events may be assessed (Figure 3.12).

$\tilde{r}^*_{trap} = 5.2$ nm we can, taking into account the localization accuracy σ^*_r, again estimate the area on which the trapping interaction takes place, with an average radius $r^*_{trap} = (\tilde{r}^{*\,2}_{trap} - \sigma^{*2}_r)^{1/2} < 5$ nm, which is even slightly lower than the trapping radius r_{trap} determined before. We determined similar values of r^*_{trap} for PE and for SM in cholesterol-depleted cells (Table 3.1).

Note that:

1. This analysis cannot claim any completeness; i.e., not all of the trapping events are identified (not even all instances where the lipid does dwell for longer than Δt within the domain area $\pi(d/2)^2$, obviously shorter traps cannot be found as there is no way to disentangle them from normal Brownian motion).

2. Random localizations (without trapping) within a domain $\pi(d/2)^2$ would yield $\tilde{r}^*_{trap} = d/4 = 15$ nm for $N = 250$ and 7.5 nm for $N = 1000$, i.e., significantly above the value found for our traps. This indicates a true clustering of the localizations on the smaller length scale.

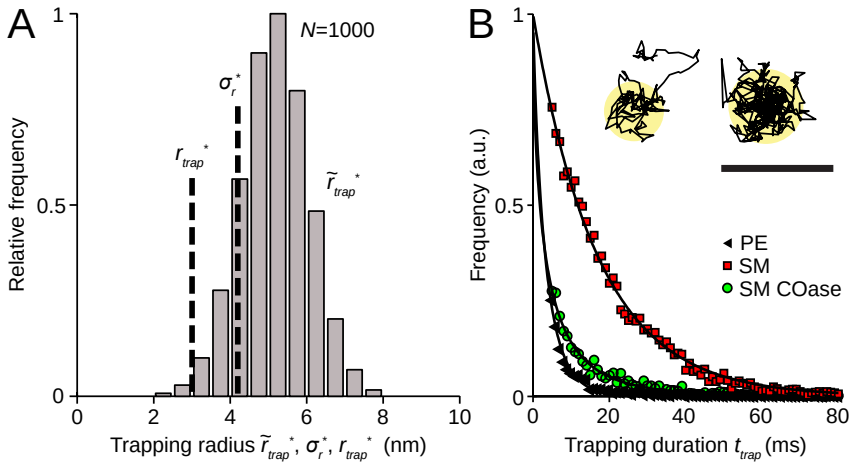

Figure 3.12: The direct examination of trajectories with prolonged residence within small regions (magnifying analysis) provided another estimate of the trapping area with radius r^*_{trap}, as well as estimates of the trapping time. (**A**) Radial standard deviation $\tilde{r}^*_{trap}$ of the set of all localizations during a selected trajectory and localization accuracy σ^*_r of the magnifying analysis resulted in $r^*_{trap} < 5$ nm for $N = 1000$; i.e., trapping occurs on the macromolecular scale (data shown: SM). (**B**) Trapping durations t_{trap} ($N = 1000$) for PE, SM-COase and SM with exponential fits yielding characteristic decay times of 3 (PE), 3 (SM-COase), and 17 ms (SM). The histograms were normalized to the amplitudes of the exponential fit. Insets show two examples of sets of all localizations during a selected trajectory. (Scale bar, 100 nm.)

We subsequently found that a related approach was described in the literature, following the same physical idea [98]. The value of σ^*_r has been determined as the spread of 500 localizations of a stationary bead with the subdomain at the center of mass of the localizations, where each localization stems from photons within a 20 ms time window (i.e., a time on the order of our trap durations): $\sigma^*_r = 10.3$ nm ($N = 250$) and 4.2 nm ($N = 1000$). We determined an average radius $r^*_{trap} = (\tilde{r}^{*}_{trap}{}^2 - \sigma^{*2}_r)^{1/2}$ of the trapping area. Note that for the analysis with $N = 250$, it was not possible to extract r^*_{trap} as the average $\tilde{r}^*_{trap}$ was even slightly lower than σ^*_r. Due to the greater number of photons N employed, the localization accuracy of the magnifying analysis ($N = 1000$) is higher and thus the values of the trap radius r^*_{trap} slightly smaller than the values of r_{trap} from the global fit analysis ($N = 250$).

The trajectories selected for this refined analysis represent the longest, most prominent traps, which potentially take up the largest area. This strongly suggests that

Results of single-molecule tracking of diffusion

	D (μm²/s)	α	r_{trap} (nm)	r^*_{trap} (nm)	$\bar{t}_{trap}$ (ms)
SLB	3.6	1	–	–	–
PE	0.35	0.75	7	5	3
SM	0.35	0.35	9	4	17
SM+COase	0.3	0.65	10	5	3
GM1	0.26	0.52	12	5	15
Ceramide	0.54	0.38	9	4	13
PI-head	0.15	0.51	5	3	8
GPI-acp	0.3	0.41	13	3	6
GPI-biotin	0.2	0.39	14	3	6

Table 3.1: Results of single-molecule tracking of diffusion. SLB: supported lipid bilayer; PE: Atto647N-phosphoethanolamine (live cell); SM: Atto647N-sphingomyelin (live cell); COase: SM diffusion after cholesterol depletion by COase treatment (live cell). D: free diffusion constant; α: time-fraction of free diffusion; r_{trap}: radius of trapping area determined by fitting $P(\Delta r^2, \Delta t)$ ($N = 250$); r^*_{trap}: radius of trapping area determined by the magnifying analysis ($N = 1000$); $\bar{t}_{trap}$: trapping time determined by the magnifying analysis ($N = 1000$). Standard deviations of values are approximately 10–30 %.

the trapping occurs on the macromolecular scale. Based on the set of traps identified as described above, we also histogrammed their duration and fitted the distribution with an exponential decay to obtain estimates of the characteristic trapping times $\bar{t}_{trap}$.

Inferring trapping times

Next, we plotted the distribution of trapping times t_{trap} of the trajectories selected from the magnifying analysis ($N = 1000$), as shown for all three cases in Figure 3.12. Two results became obvious. First, the number of selected trajectories was lower for PE and SM-COase, stemming from the much lower extent of trapping. Second, the distribution of t_{trap} was shifted to shorter times in the case of PE or SM-COase, reflecting a much shorter trapping time than for SM. Fitting an exponential decay to the distribution of t_{trap} resulted in characteristic trapping times $\bar{t}_{trap} \approx 3$ ms for PE, 17 ms for SM and 3 ms for SM after COase treatment (Table 3.1). Because of

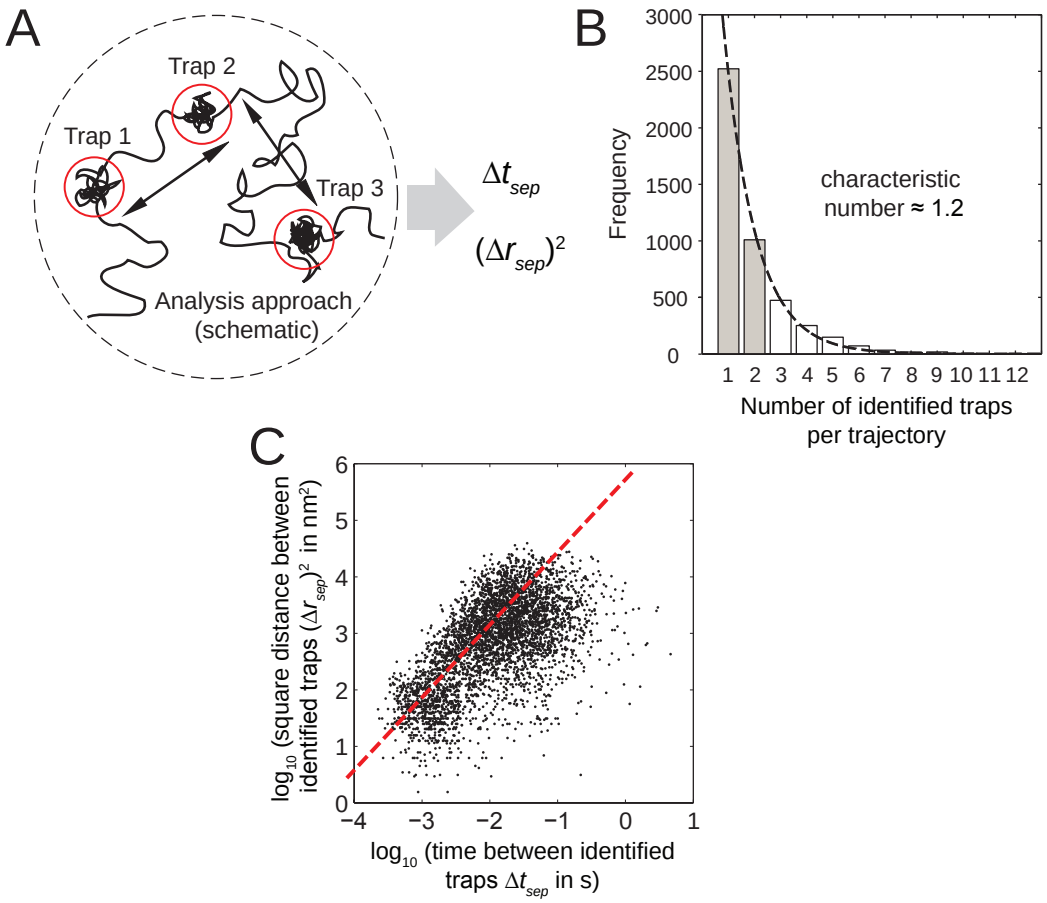

Figure 3.13: Examination of spatial and temporal inter-trap separations for sphingomyelin (SM). (**A**) Schematic of the analysis approach: trajectories with ≥ 2 traps as identified by the 'magnifying' analysis ($d = 30$ nm, $t > 3.7$ ms) can be analyzed to give the distance and time between instances of molecular trapping. (**B**) Histogram of relative frequency of multiple trapping during confocal transit. The median of the distribution lies at 1–2 traps, corresponding well with an earlier estimate from the difference in transit times between PE and SM by FCS [89]. (**C**) Scatter plot of value pairs $(\Delta r_{sep})^2$ vs. Δt_{sep}. The differences were computed between directly consecutive trapping events (8,724 traps analyzed in total). The dependence can be accounted for by diffusion at a rate of $D \approx 0.1 - 0.3 \mu\text{m}^2/\text{s}$.

the minimum accessible time of <4 ms of the alternative magnifying analysis, these values are, especially in the case of PE and of SM with COase treatment, only an estimation (Figure 3.12B).

Ceramide vs. glycerol?

The trapping affinity may be determined by the presence or absence of functional chemical groups. The ceramide group (highlighted in Figure 3.14C) could be the decisive element and responsible for trapping. By contrast, molecules without it seem to lack this affinity. Ceramide may thus account for the difference between the phosphoglycerolipid PE and sphingomyelin, which contains the ceramide group. The individual polarity of the head groups may serve for a gradation of the binding affinity and could be influential for a hierarchical ordering in molecular assemblies in a very general way (compare Figure 3.1). A full picture about the trapping interaction and its responsible binding partners will only become available once this can be assessed by means of co-localization (tracking) or cross-correlation analyses (two-color STED-FCS).

3.3 Appraisal of results in light of STED fluorescence fluctuation spectroscopy data

3.3.1 Fast nanoscale dynamics by STED

As outlined in the Introduction, appropriate spatial and temporal accuracy are essential for the study of millisecond-timescale processes on the nanometer spatial scale. The lateral mobility of membrane constituents such as lipids and proteins can be assessed by fluorescence fluctuation spectroscopy (FFS). In these methods, the fluctuations in fluorescence intensity due to molecules diffusing in and out of the observation volume are measured. Quantitative analysis through calculation of the autocorrelation function (fluorescence correlation spectroscopy, FCS) [90] provides information regarding the average residence time, and therefore the mobility

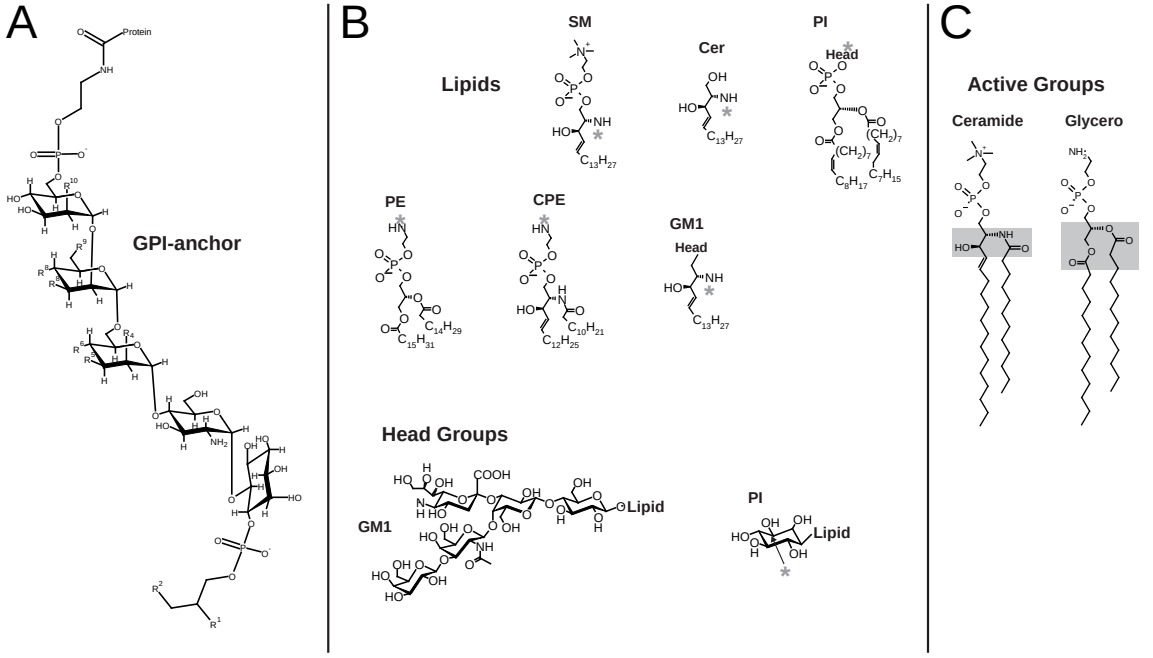

Figure 3.14: Structural details of the studied membrane constituents. (**A**) The glycosyl-phosphatidylinositol (GPI) anchor. R^1: fatty acid or OH, R^2: fatty acid or alkyl or alkenyl chain, $R^{4,9}$: ethanolamine phosphate or OH, $R^{5,6,8,10}$: carbohydrate substituents or OH. (**B**) The lipids PE, SM, CPE, PI (head-labeled), ceramide and the ganglioside GM1 with details of their head group. The asterisk denotes the position of the dye label. (**C**) Active chemical groups.

of the labeled molecules in that volume. In particular, FCS features the high temporal resolution required for studying fast membrane dynamics. [99] Yet standard FCS, implemented in a confocal microscope, suffers from a lack of spatial resolution. The 200 nm diameter focal spot dictated by diffraction averages over details of the nansocale motion of lipids and proteins. The autocorrelation of fluorescently labeled phosphoethanolamine (PE) and sphingomyelin (SM) in a confocal microscope shows no substantial difference, with perhaps a slight hint that SM may be marginally slower [89].

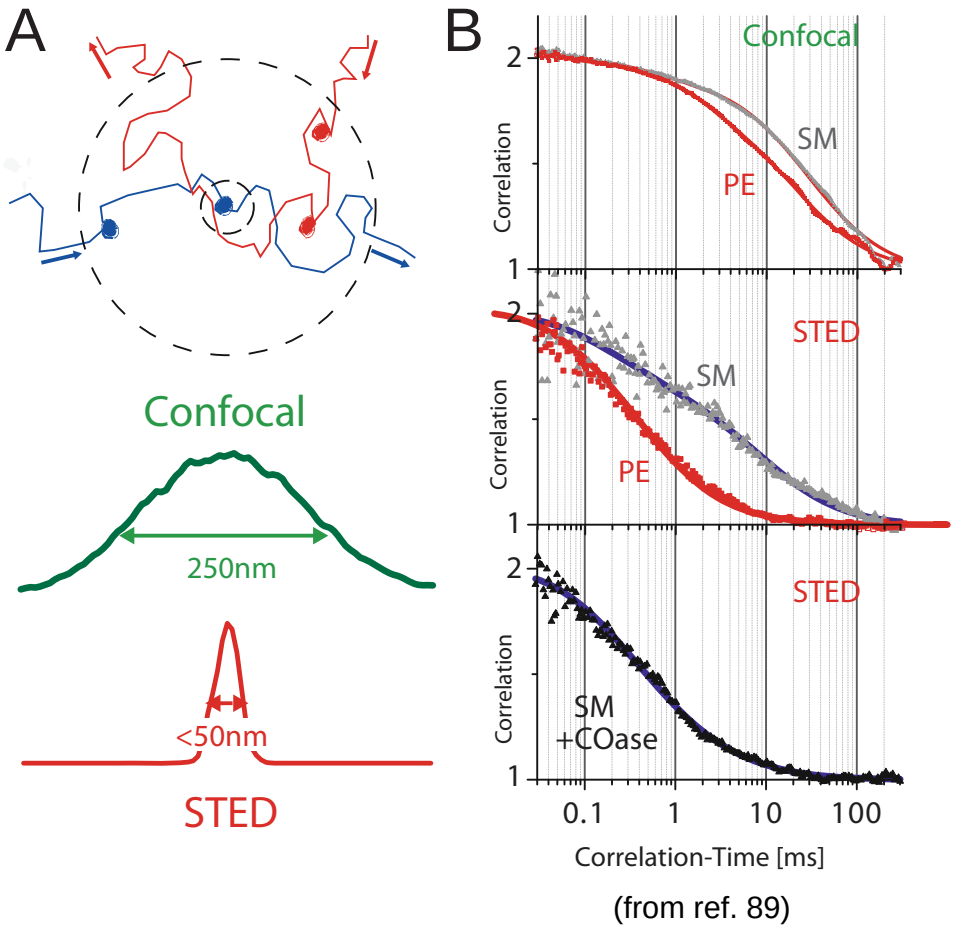

Figure 3.15: (**A**) STED can create nanoscale focal observation volumes, with which fluorescence fluctuation spectroscopy can be performed. Molecules diffuse in the membrane, in which focal spots are placed. By tuning the intensity of the STED light, effective focal volumes of varying size may be created and the diffusion behavior measured down to nanometer length scales. (**B**) The diffusion of PE and SM lipids is quantified using fluorescence correlation spectroscopy. STED nanoscopy discriminates the dynamics of single sphingo- and phosphoglycero-lipid molecules in a living cell membrane: dye-labeled sphingomyelin (SM) vs. phosphoethanolamine (PE), illustrating that freely moving molecules may be transiently trapped in the membrane due to interaction with another molecule. The passage time of freely diffusing molecules through the small spot created by STED is substantially reduced compared to the wide focal spot of a confocal microscope.

Confining the observation volume

Stimulated emission depletion (STED) nanoscopy – the first viable physical concept to overcome the diffraction barrier in far-field light microscopy – is not only a powerful method for the imaging of fluorescently labeled structures at close to molecular resolution [5,7,100]. The nanoscale effective focal volume, defined by suppressing the capability of molecules to fluoresce in the periphery of the focus, can also be put to great use in correlation spectroscopy. By tuning the intensity of the STED light, which keeps the molecules dark, Eggeling et al. [89] created foci of varying diameter down to ∼30 nm and started mapping out the diffusion law down to nanometer length scales.

They discovered that while PE exhibited largely free diffusion even on the small spatial scale, diffusion of the sphingolipid SM was much more heterogeneous at small length scales. Analysis of the anomaly in the autocorelation allowed them to conclude that SM lipids frequently undergo trapping on areas of <20 nm diameter for short periods of ∼10–20 milliseconds. This 'trapping' was no longer observed after the membrane had been depleted of cholesterol, suggesting that some form of short-term integration into molecular complexes (or potentially 'rafts' or raft precursors) occurs in a cholesterol-mediated fashion. It is interesting to note that only the spatial resolution enhancement could provide this information. This is because, for smaller foci, the difference between an unhindered transit and a transit involving the prolonged dwelling in a small area becomes obvious (Figure 3.15A), while the large diffraction-limited focus averages over nanoscale details of the motion.

3.3.2 Direct comparison of fast tracking with STED measurements

Here, we compare results obtained by fast confocalized single molecule tracking with those by STED-FCS. A variety of species were characterized in PtK2 membranes by both methods, including PE, SM, SM after COase treatment, ceramide, the ganglioside GM1, phosphatidyl inositol (PI) and two-labeling strategies for the glycosyl

phosphatidyl inositol anchor (GPI). Ceramide, GM1 and PI were prepared by lipid-BSA complex incubation [89]. GPI labeled by the acp tag was prepared according to [89], and preparation of GPI with a biotin-avidin label followed [97]. Figure 3.14 shows structural details of all studied membrane constituents.

For tracking, we have quantified the degree of nanoscale anomaly in our spatio-temporal data by the time-fraction of trapping α as introduced in Section 3.2.3 of this thesis. We assert two ways of quantifying this diffusion anomaly in the STED experiment.

1. The inverse of the anomalous diffusion exponent, which shall be denoted β: It is obtained from fits of the autocorrelation curve (in the STED case with a focal diameter of ∼40 nm) to an anomalous diffusion model given by

$$G(\tau) = \frac{1}{N}\left(1 + \left(\frac{\tau}{\tau_D}\right)^{\frac{1}{\beta}}\right)^{-1} \tag{3.6}$$

   where $\beta = 1$ in the case of free diffusion and $\beta > 1$ for hindered diffusion.

2. Characterizing diffusion at both the confocal diameter and a small diameter defined by STED (40 nm) according to

$$D = \frac{d^2}{8 \ln 2 \tau_D} \tag{3.7}$$

   where τ_D is gained from fitting of the correlation curve. Then $D_{STED} \approx D_{conf}$ implies free diffusion, as no difference can be perceived by probing with a large or a small focal area (in other words, the hallmark of Brownian diffusion is obeyed: $\tau_D \propto d^2$). On the other hand, $D_{STED} < D_{conf}$ is interpreted as hindered diffusion. Diffusion is slower through the small focus than can be accounted for merely by the geometrical shrinkage in the focal area.

Both ways of analysis of the STED data agree in their relative attribution of nanoscale anomaly with the determinations by fast molecule tracking (Figure 3.16A and B). The diffusion coefficient $D_{conf} \simeq D_{free}$ estimated from confocal FCS also correlates well with the values of D_{free} extracted from fast tracking (Figure 3.16C). Both methods are equally valid approaches – at present the only ones, to our knowledge – to gain measurement access to these detailed fast dynamics in membranes of living cells.

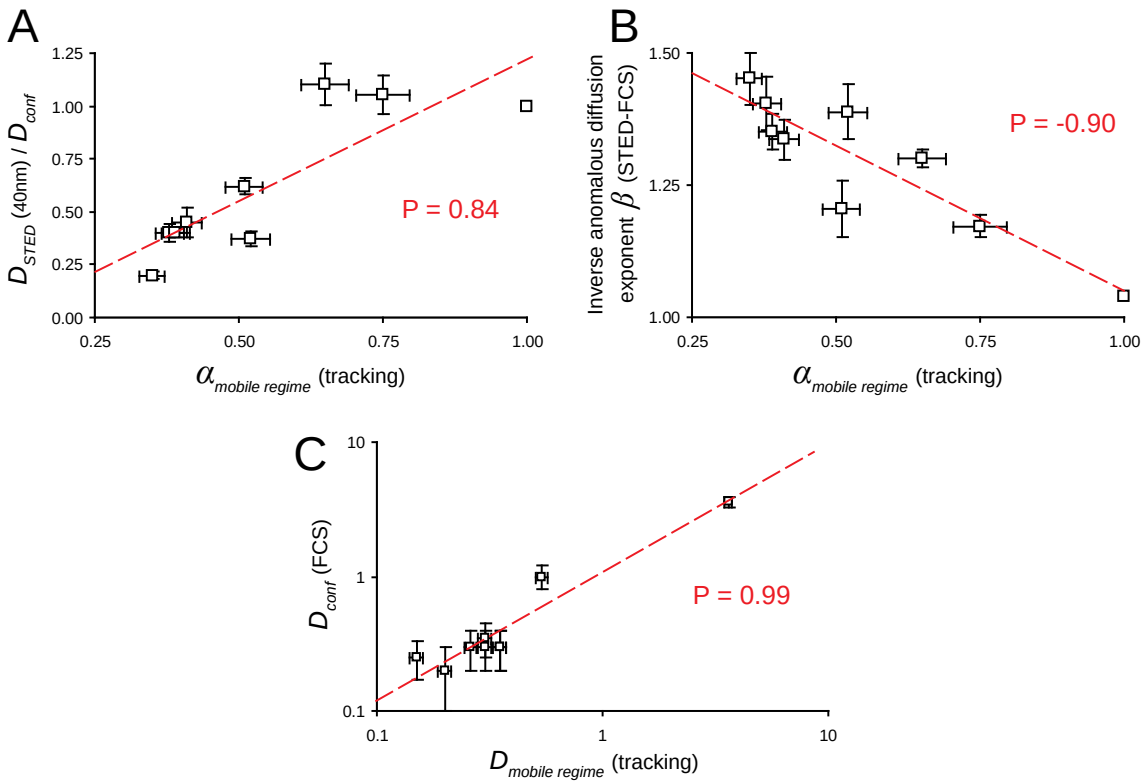

Figure 3.16: The nanoscale diffusion anomaly (deviation from free diffusion), quantified in STED-FCS as (**A**) the ratio of diffusion coefficients inferred from measurements with nanoscale STED focal area to that in a confocal focus or (**B**) the inverse of the anomalous diffusion exponent correlate with the time-fraction of trapping α found by single-molecule tracking for the lipids, ceramide and the ganglioside GM1, as well as head-labeled PI and two labeled variants of the GPI anchor. (**C**) Good agreement is observed for diffusion coefficients extracted from tracking to those estimated from confocal FCS. Pearson product moment correlation coefficients, representing a normalized measure of the strength of linear relationship between variables (computed as $\rho_{X,Y} = \mathrm{corr}(\mathrm{X}, \mathrm{Y}) = \mathrm{cov}(\mathrm{X}, \mathrm{Y})/\sigma_{\mathrm{X}}\sigma_{\mathrm{Y}}$), are 0.84 (A), -0.90 (B) and 0.99 (0.86 when excluding the fast-diffusing supported lipid bilayer) (C), respectively.

3.4 Dynamics of lipids and binding partners: Monte Carlo experiments

3.4.1 Ab-initio simulation of lipid motion and transient binding

The physical model and its implementation

Our described physical model is motivated by a view of the plasma membrane as a non-ideal mixture of diverse molecules with differing mutual miscibilities in the fluid state, i.e., it contains dynamic meso-scale (2–200 nm) molecular complexes and domains, forming and dispersing continually within the plasma membrane on various timescales. A particular focus here is on rationalizing the observed molecular trajectories with the help of first-principles simulations (Monte Carlo experiments), based on a model of Brownian diffusion and transient attachment to quasi-stationary binding partners.

Molecular kinematics

The object we observe experimentally is the isolated fluorescent lipid analog, of which we gain spatiotemporal trajectories $\vec{r}(t) = \{(x, y)\}$. By itself, the lipid diffuses in the membrane, which is assumed as a homogeneous medium characterized by a diffusion coefficient for the lipid, D_{lipid}. Diffusion can be implemented in a simulation as a random walk with steps of Gaussian-distributed steplengths Δs taken in arbitrary directions for finely sampled increments in time Δt. In parallel, a finite number of potential binding partners (proteins or molecular complexes, henceforth referred to as 'traps'), exist in this membrane. As a consequence of their size (and possibly their interaction with the cytoskeleton meshwork), they may be assumed to diffuse significantly slower (*at least* by an order of magnitude) than the rapid lipids, with a diffusion coefficient D_{trap}. Upon random encounters with such a 'trap' (modeled as occuring for a spatial approach closer than a radius of encounter r_{in}, the lipid is attached with a certain probability (energy barrier) to the trap and follows with the

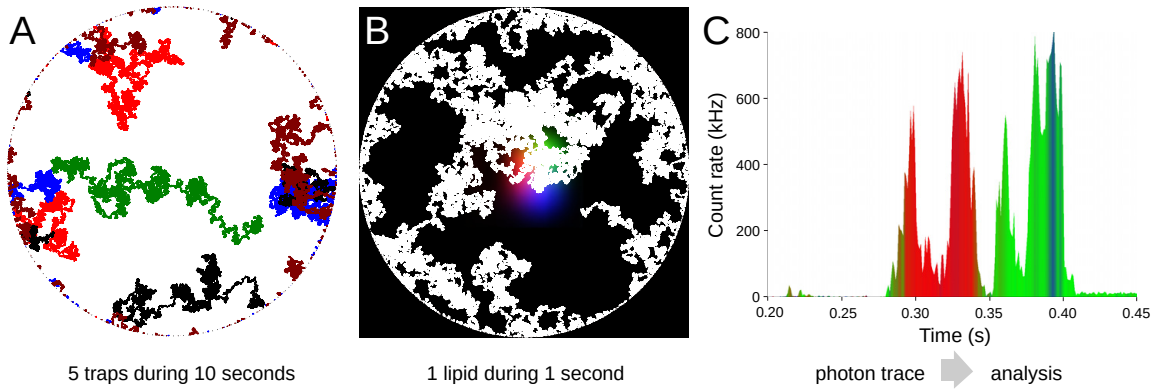

Figure 3.17: (**A**) 5 traps over the course of 10 seconds. The diffusion of on average just one lipid over the same time covers the area so densely that nothing could be perceived in the plot. (**B**) 1 s of diffusion of 1 lipid in the sandbox. (**C**) The generated photon trace as detected by the fibers allows calculation of the resulting trajectories and thus a complete simulation of the tracking experiment.

trap's trajectory for a duration distributed exponentially around an average value $\bar{t}_{trap}$. The lipid can escape the trap if it exceeds the dissociation energy barrier (by exceeding a minimal internal steplength Δs which it would perform if free). Upon escape, free diffusion at D_{lipid} is resumed. Multiple trapping upon random return to the same trap is not prohibited.

Figure 3.17A shows an example of five traps over ten seconds. The diffusion of on average just one lipid over the same time course covers the area so densely that nothing could be perceived in the plot. Just one second of lipid diffusion is therefore displayed in panel B.

All lipid and trap kinematics were simulated within a circular simulation sandbox. Its size was chosen to be at least three times the diameter of the extent of the detection elements (∼500 nm for our present confocalized tracking scheme) to avoid border effects. If a particle (lipid or trap) reached the border of the sandbox, it was placed at a new point randomly chosen on the circumference circle of the sandbox. Thus spatial correlation among leaving and entering particles was avoided. Nonetheless, a small build-up of effective dwelling of the lipid may be noticed at the peripherey of the sandbox, where it both leaves and enters, as the probability of leaving yet again and then entering on some other point of the circumference is as high as making its

way towards the center – where it can cross the excitation and detection area and emit fluorescence photons.

From simulated kinematics to photon traces to 'experimental' lipid trajectories

We described how the temporary interaction with traps modified the path taken by the lipid. In the experiment, only the resultant position of the individual lipid is detected. The simulation therefore includes the fluorescence emission. When the lipid moves over the central region defined by the projected pinholes, photon counts are generated in the appropriate channels c_i based on the excitation light intensity distribution and relative detection efficiency of the three detectors. The required information is contained in a typical localization reference map obtained by a small bead scan (Chapter 2). A photon trace containing t_i and c_i is thus obtained, which can be analyzed exactly like an experimental data trace.

3.4.2 Results for the transient binding picture

The observed histograms of the cumulative probability of square displacements $P(\Delta r^2, \Delta t)$ could be approximately reproduced for the expected parameters (Figure 3.18). The diffusion of the potential binding partners (traps) was assumed to be at least an order of magnitude slower than that of the lipid ($D_{lipid} \approx 0.1 - 0.5 \mu\mathrm{m}^2/\mathrm{s}$). As D_{lipid} was varied as an input parameter, this was accurately reflected in the resulting fits, leaving the time-fraction of trapping, $1 - \alpha$, largely unaffected.

The Monte Carlo simulations also served for verifying the localization accuracy by comparing the simulated trajectories with the observed trajectory. Simulated trajectories may be directly compared to the trajectory which results upon counting the generated photons and carrying out our localization routines. This is a good measure as the simulation includes the Poissonian noise of fluorescence detection and non-uniformity of the reference map owing to the true fiber shapes. These simulations again suggest that the physical picture of binding to a stationary or comparatively slow-moving object (a molecular complex) for on average a certain duration is ade-

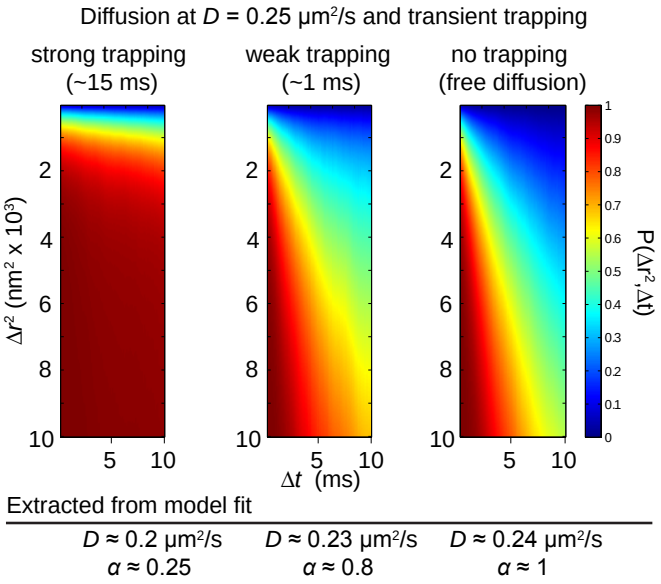

Figure 3.18: Simulated examples of the cumulative probability $P\left(\Delta r^2, \Delta t\right)$ as a function of time lag Δt and squared displacement Δr^2 for (i) diffusion at $D = 0.3\mu\mathrm{m}^2/\mathrm{s}$ and interaction with traps that bind the molecule for an exponentially distributed time around a characteristic $\bar{t}_{trap} \approx 15$ ms (strong trapping), (ii) as in (i) but with only little trapping: $\bar{t}_{trap} \approx 1$ ms and (iii) free diffusion at $D = 0.3\mu\mathrm{m}^2/\mathrm{s}$. Results of global fits to the data by our two-component model are indicated.

quate for the description of our data.

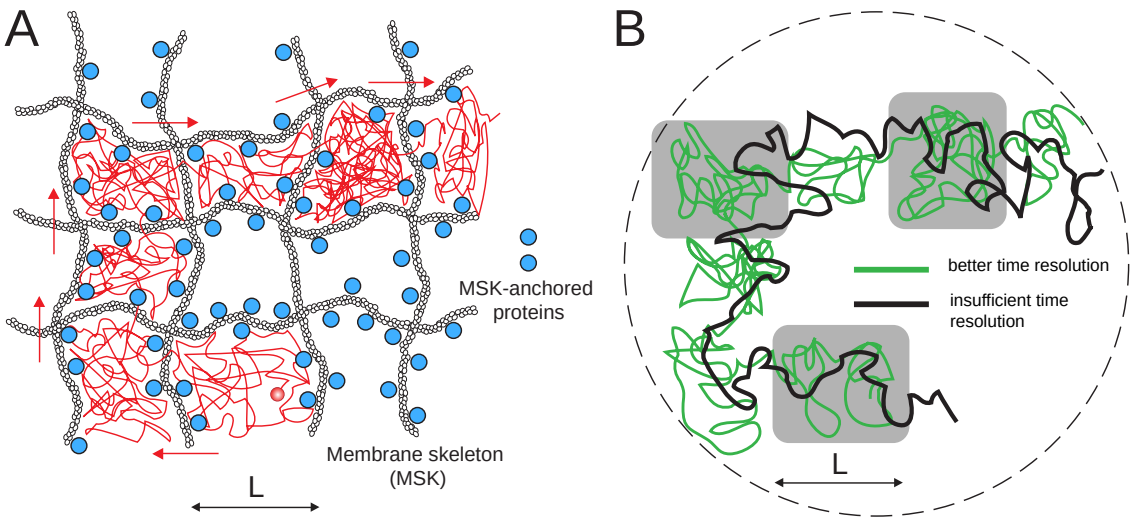

Figure 3.19: Model of hop diffusion. The plasma membrane is parceled up into compartments (corrals) of a typical size L. Within this model, all molecules are thought to undergo short-term confined diffusion within a compartment and long-term hop diffusion between the compartments. (**A**) A hyptothetical lipid path taken. (**B**) Its trajectory sampled with limited spatio-temporal resolution resembles largely free diffusion. The confining nature of the boundaries is only perceived – and such compartments and hops among them may then be tentatively identified by a computer program [30, 98] – if a sufficient number of trajectory points sample the intra-corall movement.

3.5 Relation to the hop-diffusion model

A different model of the plasma membrane assumes that it is parceled up into apposed domains for both lipids and proteins. In this view [101], the membrane may be partitioned or compartmentalized for the translational diffusion of both proteins and lipids: *all* of the molecules incorporated in the plasma membrane undergo short-term confined diffusion within a compartment and long-term hop diffusion between the compartments. This is assumed to be likely due to the filamentous actin meshwork associated with the cytoplasmic surface of the plasma membrane ('membrane skeleton' for short), and to various transmembrane proteins anchored to and aligned along the actin filaments (Figure 3.19), which are thought to form boundaries hindering the diffusion of membrane constituents.

Fast molecular tracking data and the hop diffusion model

While the cholesterol-dependence and the pronounced nature of our observed trapping for the sphingolipid SM ($\bar{t}_{trap} \approx 15$ ms) strongly indicate that the interaction with nanoscale complexes should be the major determinant in hindered diffusion, we present here an assessment of our data in the light of the hop diffusion picture of membrane oganization. Diffusion within impermeable square corrals of size L can be described by the mean square displacement $MSD_{conf} = f(L^2, D_{micro}, \Delta t)$ with D_{micro} the short-range diffusion constant of the molecule within the confined area ($MSD_{conf}(t_{lag} \rightarrow 0) = 4D_{micro}t_{lag}$); f has been calculated by Powles et al [102], yielding

$$f = \frac{L^2}{3} - \frac{32L^2}{\pi^4} \sum_{k=1(odd)}^{\infty} \frac{1}{k^4} \exp\left[-\frac{1}{2}\left(\frac{k\pi}{L}\right)^2 2D_{micro}\Delta t\right], \tag{3.8}$$

Its asymptotic behavior for long time-lags is given by

$$MSD_{conf}\,(\Delta t \rightarrow \infty) = \frac{L^2}{3}. \tag{3.9}$$

If the corrals have a nonzero permeability, a molecule can escape and hop from corall to corall. For long observation times, the molecule appears to diffuse freely with a macroscopic diffusion constant

$$D_{macro} = \frac{L^2}{4\tau}, \tag{3.10}$$

where τ describes the residence time within a corral. MSD increases with increasing time-lag and converges to

$$MSD_{hop}\,(\Delta t \rightarrow \infty) = 4D_{macro}\Delta t + CO. \tag{3.11}$$

Wieser at al [103] have provided an interesting discussion on the hop diffusion model and possible approaches to test its applicability by single molecule (camera-based) tracking. An analytical approximation is derived which assigns meaning to quantities that can readily be extracted from the MSD. The confinement offset CO contains information about the size of the confinement zones. CO/L^2 can be regarded as a sole function of the dimensionless variable

$$\hat{\tau} = \frac{\tau}{L^2/4D_{micro}} = \frac{D_{micro}}{D_{macro}}. \tag{3.12}$$

$\hat{\tau}$ sets the residence time of a confined molecule, τ, in relation to the time a freely diffusing molecule would stay in the same region; per definition $\hat{\tau} \geq 1$. As a rule of thumb, $\hat{\tau}$ can be interpreted as the confinement strength. In general, partially permeable corrals will lead to a decrease in the offset, which will vanish when the barriers are totally removed.

Following Wieser et al., the offset CO is given by

$$CO = \frac{L^2}{3}\left(1 - \frac{1}{\hat{\tau}}\right)^2 \frac{1}{1+\hat{t}_{ill}} - \frac{4}{3} D_{macro} t_{ill}. \tag{3.13}$$

where $\hat{t}_{ill} = t_{ill}/\tau_{micro}$ is the normalized illumination time – accounting for movement of the molecule during the illumination time.

Under our experimental conditions (see below), to good aproximation we have that

$$CO \approx \frac{L^2}{3}\left(1 - \frac{1}{\hat{\tau}}\right)^2 \tag{3.14}$$

and thus

$$L \approx \sqrt{\frac{3CO}{\left(1 - \frac{1}{\hat{\tau}}\right)^2}}. \tag{3.15}$$

As discussed earlier, the nonzero localization accuracy has to be further taken into account by

$$MSD_{real} = MSD + \Delta, CO_{real} = CO + \Delta \tag{3.16}$$

with $\Delta = 4\sigma_{xy}^2, \sigma_{xy} \approx \sigma_x \approx \sigma_y$ denoting localization accuracy, i.e., the standard deviation in a data set of positions from consecutive localizations of a single molecule.

Hop diffusion analysis

We analyzed the measured trajectories using this hop diffusion model. The mean-square displacement (MSD) was computed as the expectation value of the square displacement $\langle \Delta r^2 \rangle$ for lag times Δt from $p\left(\Delta r^2, \Delta t\right)$. We show an overview of normalized MSD vs. time-lag Δt for various representative molecules in Figure 3.20B.

By linear fits to the portion of MSD for $\Delta t = 6 \ldots 10$ ms, both the total offset $CO_{uncorrected}$ and from the slope a value for D_{macro} can be extracted. Similarly, we may estimate D_{micro} by fitting the initial linear increase through the first three–five

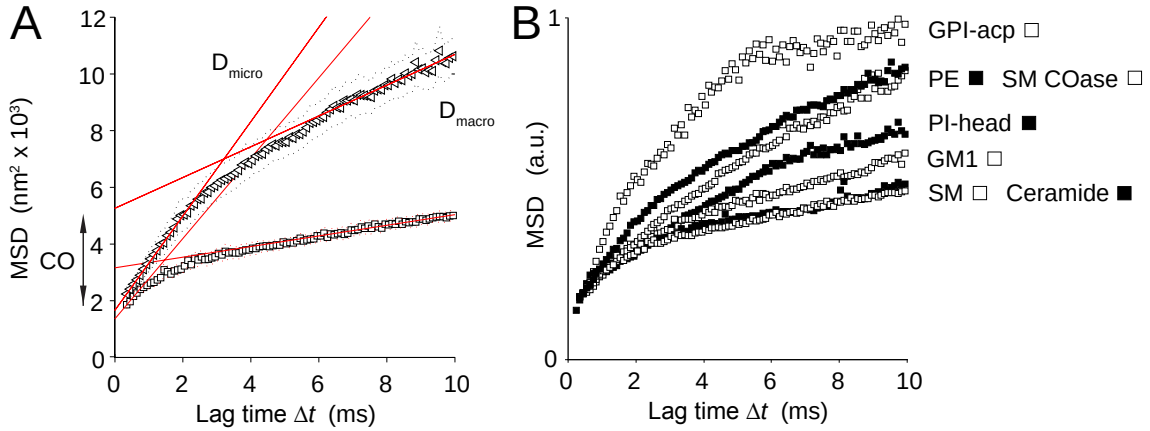

Figure 3.20: (**A**) Extraction of parameters from linear fits to the MSD (see text). (**B**) The mean-square displacement (MSD) normalized to a common start point reveals also a qualitative difference between the GPI anchor and the other membrane molecules.

data points (increments of Δt are 0.1 ms). The corresponding offset stems from the localization accuracy $4\sigma_{xy}^2$. Errors in each of these quantities may be assessed from the fit error and a consideration of steepest / shallowest slope. Evidently, the ordinate intercepts are subject to a larger relative error than are the diffusion coefficients from the slopes. For the approximate values obtained, both correction terms involving the illumination time t_{ill} (which is our effective time resolution, the time to acquire 250 photons) in combination contribute $\leq 2\,\%$ relative to the expression above given for L. A solution of the resulting bi-quadratic equation in L confirmed this approximation and the resulting values of L. Performing Gaussian error propagation analysis yielded for the expected error in the compartment size L

$$\sigma_L = \sqrt{\frac{3}{4CO\left(1-\frac{1}{\hat{\tau}}\right)^2}\sigma_{CO}^2 + \frac{3CO}{\hat{\tau}^4\left(1-\frac{1}{\hat{\tau}}\right)^4}\sigma_{\hat{\tau}}^2}. \tag{3.17}$$

Errors were also propagated for the error in the confinement strength, $\hat{\tau}$.

Hop diffusion or localized interactions?

We can analyze our tracking data in another way to assess whether or not hop diffusion between partially permeable corrals (compartments) may provide a satisfy-

ing explanation for the observed anomaly in the diffusion paths, in particular for the striking example of sphingomyelin (SM). Consider the following argument: Let T be the total duration of analyzed trajectories,

$$T = \sum \text{time windows of analyzed trajectories.} \tag{3.18}$$

For $\bar{A} = L^2$ the average area of a corral and D_{macro} the longterm diffusion coefficient ($\Delta t \to \infty$), it holds that

$$\bar{A} = 4 D_{macro} \bar{\tau}. \tag{3.19}$$

for an average time between hops $\bar{\tau}$.

For an average time $\bar{\tau}$ between hops, the total number of expected hops (or compartments traversed) is then given by

$$N = \frac{T}{\bar{\tau}} = \int_{t=0}^{t=\infty} C \cdot e^{-t/\bar{\tau}} \, \mathrm{d}t. \tag{3.20}$$

It follows that $C = N/\bar{\tau}$ and that the expected number of hops N_i that should be observable within time intervals $t_i \ldots t_{i+1} = \Delta t$ can be calculated as

$$C \left[-\bar{\tau} \cdot e^{-t/\bar{\tau}} \right]_t^{t+\Delta t} = N \left(e^{-t/\bar{\tau}} - e^{-(t+\Delta t)/\bar{\tau}} \right). \tag{3.21}$$

From the recorded SM data, we found $T = 685$ seconds. For a given $\bar{\tau}$, $N = T/\bar{\tau}$ hops would have occurred on average. Figure 3.21A shows the distribution of confinement events ('traps') in the SM trajectories identified by the magnifying analysis. This analysis found instances where the lipid dwelled longer within a small domain than was likely to arise from simple Brownian diffusion. Agreement is observed when the analysis is carried out for $D = 30$ nm domains (white bars) and again for $D = 60$ nm domains (gray bars), binning $N = 1000$ photons in both analyses. This finding in itself supports the idea that the trapping is highly localized.

We now consider the expected distributions for a molecule undergoing hop diffusion over membrane compartments as just derived. They are displayed in Figure 3.21A for various values of $\bar{\tau}$. For small $\bar{\tau}$ (<5 ms), the hop distributions would not account for the tail of long events that were observed. Also, a much higher number of short

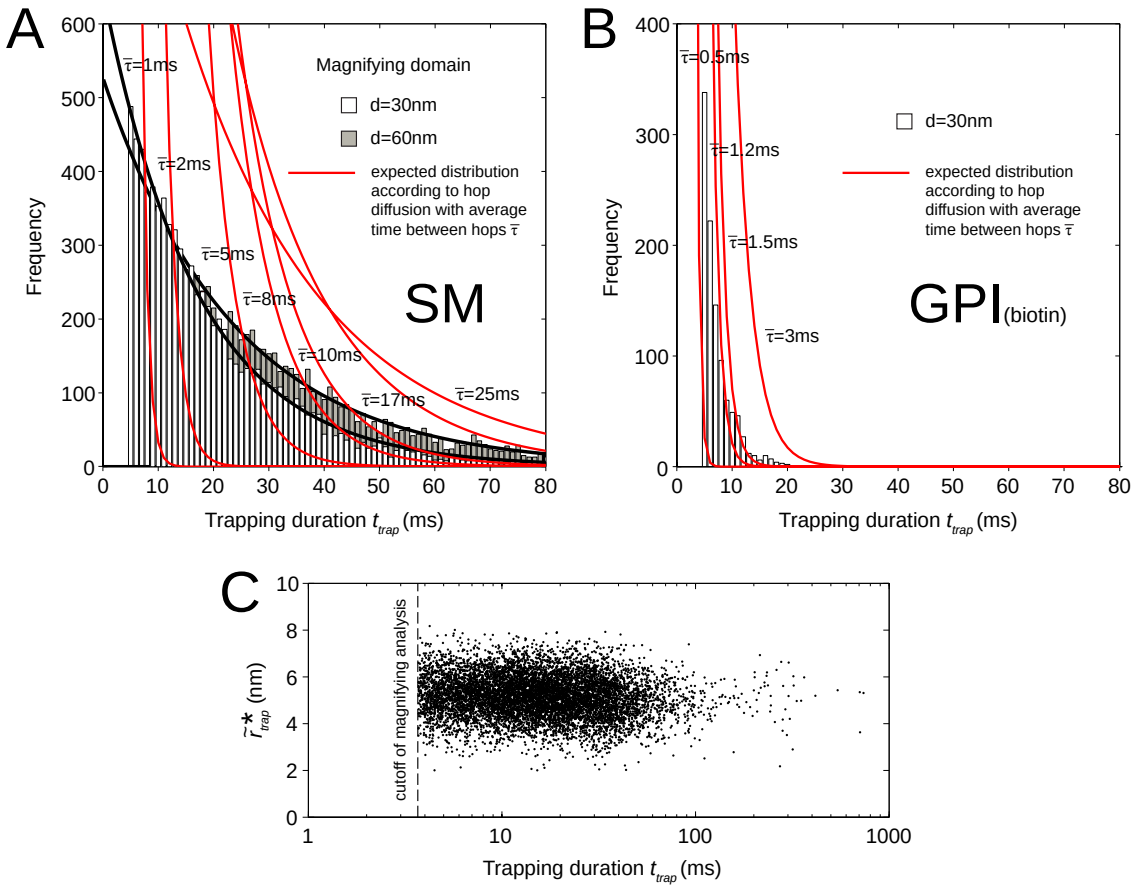

Figure 3.21: The number of identified occurrences of nanoscale confinement ('trapping') for sphingomyelin (SM) cannot be explained by a hop diffusion model. (**A**) Distribution of trap durations t_{trap} as obtaied from the 'magnifying' analysis for a $D = 30$ nm domain (white bars) and a $D = 60$ nm domain (gray bars) with $N = 1000$ photons. The set of curves displays expected distributions for the duration of dwelling within supposed observable compartments ('corrals') with average residence times $\bar{\tau}$ calculated for the total analyzed observation time of the SM trajectories (see text for further description and interpretation). (**C**) Trap size $\tilde{r}^*_{trap}$ vs. trap duration t_{trap}. No dependence is seen, indicating a transient binding interaction on the molecular (< 10 nm) scale. The choice of either diameter of the 'magnifying glass' leads to the same results. (**B**) By contrast to SM, the observed distribution for GPI could largely (but not entirely) be accounted for by confinement of short duration ($\bar{\tau} \approx 1 - 2$ ms with some additional trapping. Likewise, the distributions found for PE and SM-Coase (Figure 3.12) do not exclude (weakly confining) hop diffusion as a mechanism underlying their diffusion.

events should be identified but is not – while there would have been no reason for the 'magnifying' analysis to discard these events. Significantly longer $\bar{\tau}$ (>15 ms) would feature an appropriate decay constant to match the observed distribution – yet the absolute numbers of corrals expected are above (by a factor of ∼2) those actually found. The explanation that perhaps a large number of traps somewhat larger than the domain size were missed by the 30 nm magnifying domain can be excluded since the same numbers of traps were found within a domain four times its area ($D = 60$ nm) and thus comfortably large enough to accommodate bigger traps. More importantly however, such long residence times in small corrals would translate into very slow diffusion coefficients D_{macro} – e.g. <0.002 μm^2/s for $\bar{\tau} = 15$ ms and $\bar{A} = 100$ nm^2, which is more than an order of magnitude below what was guided from the MSD approximation in the previous section. Such long residence times may therefore be excluded as an explanation in conjunction with small confinement zones. Very long residence in significantly larger domains (>60 nm) are not disproved by this analysis, though they certainly do not explain the prolonged residence on nanoscale areas that we have shown by direct inspection.

Conclusions

Rather excitingly, our confocalized tracking approach has advanced into a regime of temporal resolution which was previously inaccessible, at least for small-dye-labelled lipids – that is, *true* molecular, not gold-particle-labelled, lipids. This allowed to determine the MSD for short time lags down to ∼0.3–0.4 ms and at least partially resolve the initial rise in MSD. In this analysis, we fully ascribed the temporal evolution of the MSD to temporary confinement in domains, which manifested itself in an additional offset in the MSD vs. Δt plot.

Our analysis shows compatability with this model only for rather large compartments ($L \approx$ 90–120 nm) and displays a potentially meaningful differentiation among molecular species with respect to their confinement strength $\hat{\tau}$.

We take the view that a more complete understanding can only be gained if the magnifying analysis is included in the discussion. Hop diffusion with a typi-

cal residence time in small (<20 nm) domains of ∼1–2 ms cannot explain the pronounced occurrence of long confinement of many milliseconds' duration. This realization calls into question that the larger pin-pointed domains from the MSD analysis exist. Rather, the considerable proven sub-10-nm anomaly probably alters the shape of the MSD curves to imply a non-existing larger length scale in the trajectories.

However, it is possible that the behavior of the GPI anchor (Figure 3.21B) – measured in this study in two variants, with the acp-tag and avidin – is best described by hop diffusion or more likely by a combination of both confinement (hop diffusion) and molecular interactions (trapping). This interpretation derives from the fact that a high anomaly is seen – a high attribution to the time-fraction α of quasi-stationary behavior in our two-component fit model (Equation 3.5) – while at the same time long localized traps were hardly observed by a 'magnifying analysis' seeking to identify long instances of trapping. The striking qualitative difference (Figure 3.20B) of the mean-square displacement for GPI compared to the other membrane molecules should be a starting point for further investigation. The ability to resolve the steep initial increase in MSD also exemplifies once again the significant advance in time resolution (<0.5 ms) of our experimental approach.

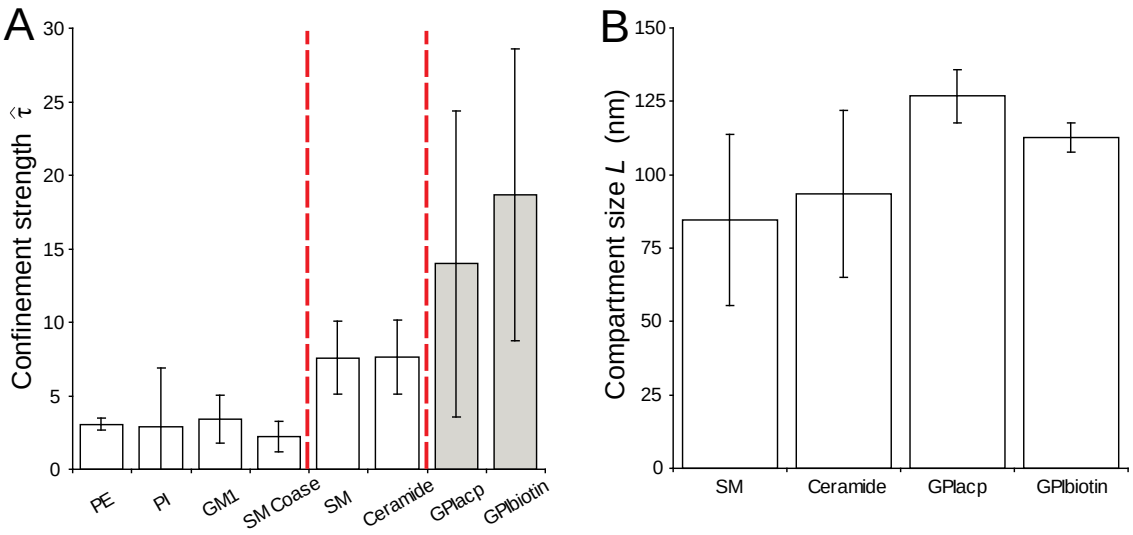

Figure 3.22: (**A**) Confinement strength $\hat{\tau}$ and (**B**) compartment size L estimated from an analysis of the mean-square displacement versus lag time as suggested in [103]. Following this analysis implied that, within the hop diffusion model of corrals of similar size, our data would only be compatible with rather large corral domains. Even so, the confining effect is found relatively moderate ($\hat{\tau} \leq 3$) for PE, PI, GM1, SM COase, and somewhat more pronounced for SM and ceramide. The GPI anchor shows high values of confinement ($\hat{\tau} \approx 15$). The confining domains determined from the described procedure have an estimated size of $L \approx 90 - 120$ nm. The analysis may not be appropriate in our case, as we have shown unambiguously that prolonged dwelling of the molecule on very small lengthscales ($r^*_{trap} \leq 5$ nm) could be identified. In the alternative analysis presented here, this strong non-corral-anomaly is presumably subsumed into the corral picture, which possibly alters the resulting values significantly. As shown in a separate analysis, such a hop diffusion picture cannot account for the long molecular-scale trapping we observed. For the GPI anchor, the analysis points to more complex behavior such as a possible mixture of short localized intercations with hop-diffusion-type dynamics, leaving open the question of what the confining structural elements might be.

Chapter 4

Application: Far-field fluorescence nanoscopy with complete photon statistics of molecular registrations

Ever since the discovery of the diffraction barrier in the nineteenth century [2–4], it was commonly accepted that a lens-based (far-field) optical microscope cannot discern structural details much finer than about half the wavelength of light ($\lambda/2 \geq 200$ nm). This barrier was overcome when it was realized that mechanisms exist which allow the individual registration of structural entities mutually closer than the diffraction limit [5–10]. A race towards three-dimensional far-field optical 'nanoscopy' approaching molecular-scale spatial resolution set off. All viable concepts reported and implemented to date exploit a transition between a bright and a dark state to switch the fluorescence capability of molecules such that adjacent objects or molecules emit sequentially in time. This Chapter describes proof-of-principle experiments on the implementation of fluorescence nanoscopy with access to the complete photon statistics stemming from stochastically read-out molecules that are localized to construct an image. As will be seen, this capability should in principle exhibit favorable features since the additional noise in the measurement due to background may be discarded during idle periods in which the molecule is not emitting and thus conveying information about its location. Related schemes based on detection elements of fast

(nanosecond) response time could allow image recording at much faster frame rates in the future.

4.1 Overcoming the diffraction barrier by molecular transitions

The elements of far-field optical nanoscopy [5–10] are laid out in Figure 4.1A. Objects more proximal than the extent of the diffraction-limited focal region may only be separated if they are made distinguishable by employing a transition between a bright and a dark state to switch the fluorescence capability of molecules. By ensuring that adjacent objects or molecules emit sequentially in time, images with nanoscale resolution can be obtained, even though each individual emitter can only be observed by its diffraction-limited image. The bright state A is either actively confined in space in targeted-readout nanoscopy schemes (typically implemented in a laser-scanning microscope, [5–7]) or by stochastic toggling of the molecules in the sample between the two states and detecting temporally isolated molecules in state A. This chapter focuses on the latter principle.

For some time, it was thought that this toggling should occur in a controlled way, and the focus was therefore on 'genuinely' switchable markers, where the two states correspond to different conformational states or isomers of the molecules. This included photoswitchable proteins such as EosFP [104], PA-GFP [105], etc., as well as organic Cyanine dyes both as activator-emitter-pairs [106] and as single photoactivatable labels [107, 108]. These and other markers require dedicated activation or deactivation schemes, increasing the experimental effort [104–106, 108, 109]. The need for activatable compounds would narrow the available dye types to a small subset of all fluorescent markers.

Fölling and colleagues [110] introduced the application of a broad range of conventional and commercially available organic dyes such as Rhodamine 6G, Atto532, Texas Red, etc., for nanoscopy. These dyes are known to be non-switchable. However, almost every fluorophore and fluorescent protein possesses long-lived electronic

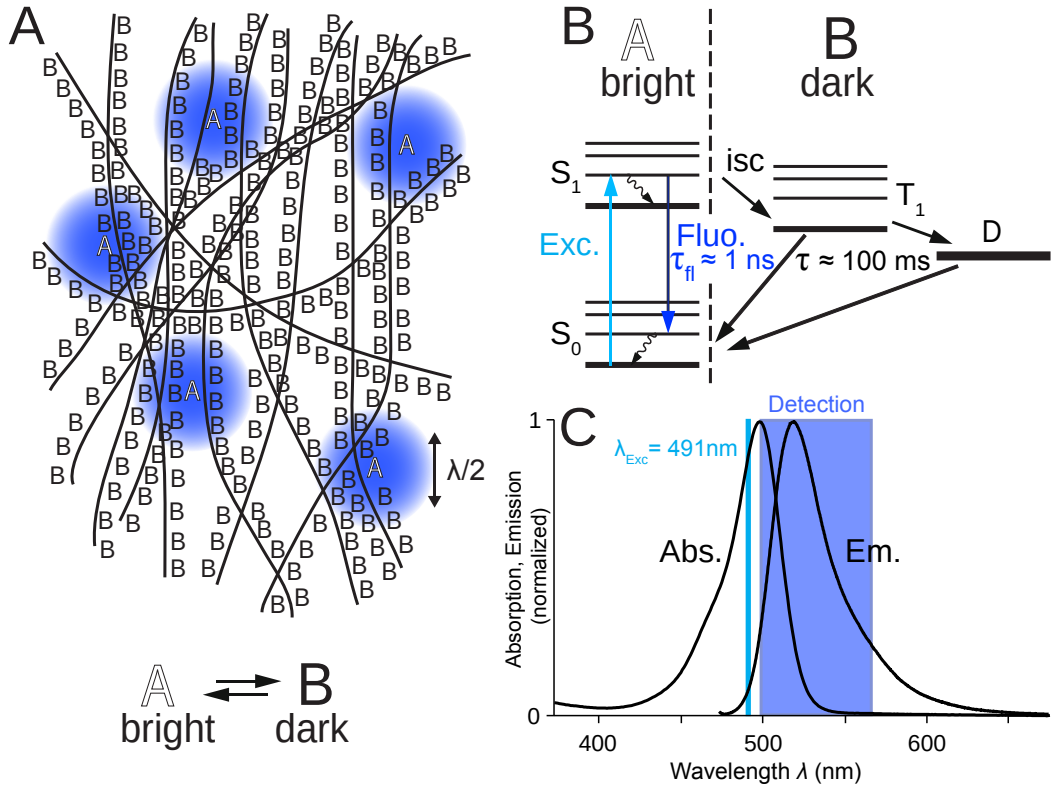

Figure 4.1: Overcoming the diffraction barrier by transferring molecules to either of two distinguishable states (**A**) The stochastic readout mode (utilized in GSDIM nanoscopy in this Chapter) detects single fluorophores from random positions within the diffraction zone. To this end, a molecule is transferred to a state A which is able to emit $m \gg 1$ photons in a row. The neighboring molecules remain in the dark, owing to an inherent inhibition preventing B $\rightarrow$ A. The closest molecule in state A should be further away than the diffraction limit $\lambda/2NA$. The detection of $m \gg 1$ photons allows the calculation of the coordinate of emission from the centroid of the diffraction fluorescence spot (usually formed on a camera). After the recording, the molecule is switched off to B in order to allow the recording of an adjacent molecule. (**B**) Jablonski state model of a conventional dye used in GSDIM. The on-state (A) of the dye is the singlet $S_0 - S_1$-system of the dye (left of dotted line), the off-state (B) is the long lived triplet state T_1 and other dark states populated via T_1 (right of dotted line). (**C**) Normalised excitation and emission spectra of Alexa488 recorded in ethanol.

dark states. This results in a typical blinking behavior of the dyes, well known in single molecule spectroscopy. These inherent long-lived electronic dark states can be exploited and readily render conventional, non switchable dyes applicable for the described variant of nanoscopy. This concept is also known from RESOLFT-microscopy as Ground State Depletion (GSD) [6,111,112]. The conceptual and experimental simplicity of this approach is rather striking. The excitation and switch-off is performed at the same wavelength, and the *spontaneous* return of these dyes to their ground state even makes activation obsolete, rendering the experimental setup very simple. The concept is referred to as GSDIM ('Ground State Depletion with Individual Molecule return'). A multitude of dyes are suitable for this nanoscopy method and have been characterized in detail [113].

Photophysical considerations in GSDIM nanoscopy

Ground state depletion is a fluorescence switch-off mechanism which exploits the long lifetime τ of the first excited triplet state T_1 of the fluorophore or other dark states D populated from T_1 as depicted in the state scheme in Figure 4.1B [6,111,112]. In the dark state, the molecule is excluded from the process of excitation and emission between the ground state S_0 and the first excited singlet state S_1 and thus finds itself in a non-fluorescing off-state (right of dotted line). The corresponding fluorescing on-state is the singlet $S_0 - S_1$-system, in which the fluorophore can be cycled by the excitation light and fluoresce (left of the dotted line). Whenever a fluorophore is excited to S_1 with its lifetime τ_{fl}, it can either relax to S_0 by emitting a photon with quantum yield $q_{fl} < 1$ or it can undergo intersystem crossing (isc) and transfer to T_1 with a probability q_{isc}. Because of its quantum nature, one usually calls these probabilities quantum yields and attributes the symbol 'q'. Return from S_1 yields photons with a probability q_{fl}, that is a photon burst is emitted with the mean number of photons

$$\bar{N} = \frac{q_{fl}}{q_{isc}} \tag{4.1}$$

before the molecule will be taken out of the cycling process by entering T_1.
The population ε_{off} relative to the on-population is proportional to $q_{isc} \cdot \tau$ [114].

Therefore, we require high q_{isc} or high τ. Unfortunately, high q_{isc} is concomitant with a small average photon number $\bar{N}$ (Equation 4.1). Thus we have to increase τ. The lifetime τ of a standard fluorescent dye is usually in the range of $10^{-3} - 100$ ms [6], depending on the dye and notably the environment. Furthermore, T_1 serves as a gateway to other dark states with similar or even longer τ of $1 - 10^4$ ms [115].

4.2 Nanoscale imaging with the 'single-photon camera'

4.2.1 Proof of principle: the single-photon camera

In Chapter 2 we introduced an optical setup capable of precise localization of individual molecules in the focal plane by combining photon count information on distinct detectors. Once emission of individual emitters is temporally separated (unmixed), the resolution of the resulting image reconstructed from many such localizations is determined by the localization accuray for individual molecules.

While the outer region – where signal is largely collected in just one fiber, rendering the identification of position very imprecise because of the high relative noise in the other fiber detectors – should be excluded, Figure 4.2F and G show that positions in the central region of approximately 500–600 nm are reproduced with high fidelity. In this central region (marked in white in Figure 4.2G), the localization accuracy is largely governed by the shot noise limit and follows the expected dependence on the detected number of photons N shown in Figure 4.2F. A fit to

$$\sigma_{eff} = \sqrt{\sigma^2_{shot\,noise} + \sigma^2_{vib,sys}} = \sqrt{\frac{A^2}{N} + \sigma^2_{vib,sys}} \tag{4.2}$$

with fit parameters A and $\sigma_{vib,sys}$ yielded for $A \approx 262$ nm, corresponding to the $FWHM$ of the detection PSF and for $\sigma_{vib,sys}$ (vibrations and systematic effects), in which we subsume other contributions to the localization error such as setup stability or systematic errors due to finite pixel size in the reference map or unfavorable noise from further-away detectors, a value of ≈ 7 nm. Most likely owing to the last influence

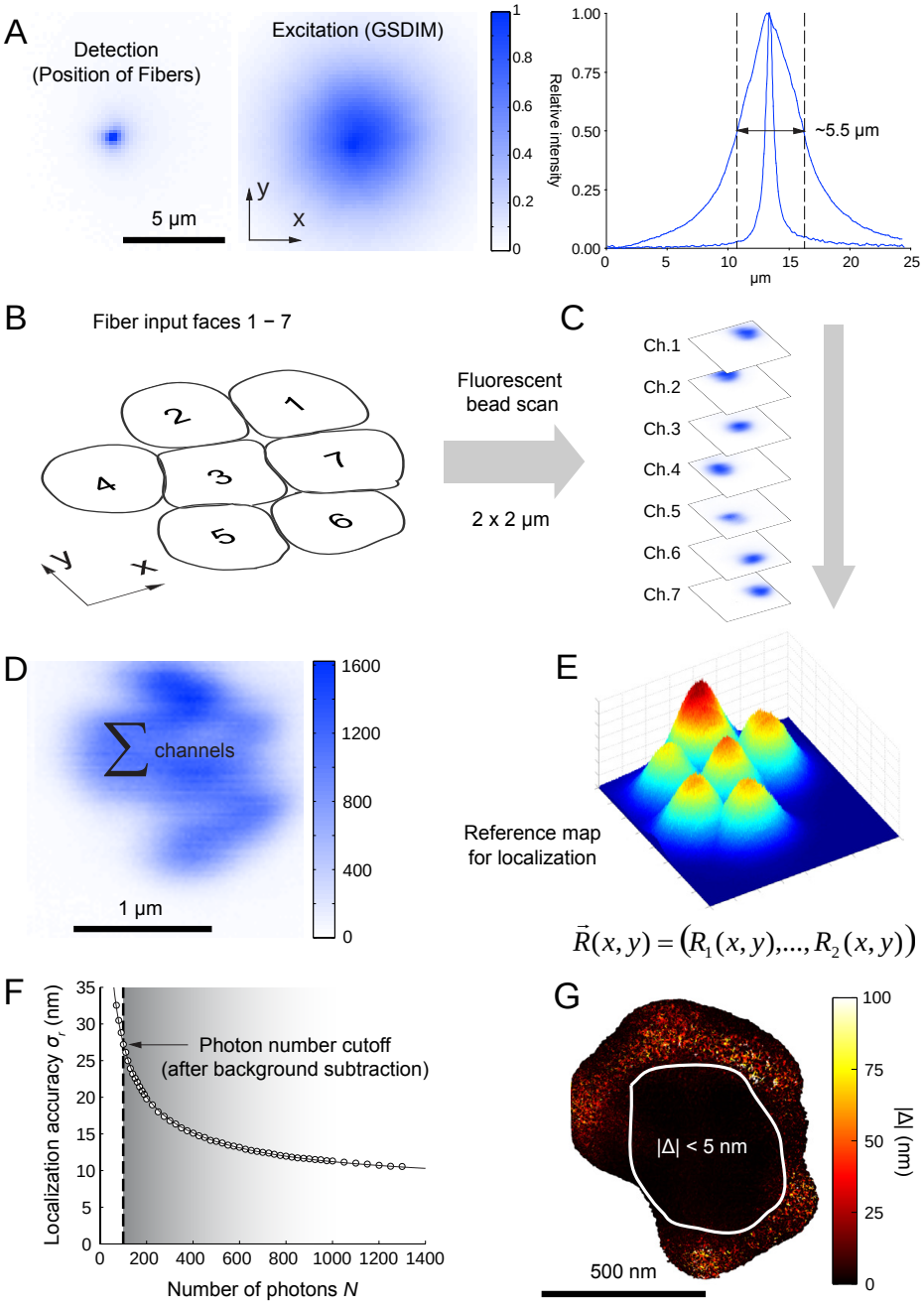

Figure 4.2: Proof of principle experiments with the 'single photon camera' (**A**) To ensure the efficient transfer of a majority of molecules to non-fluorescent dark states over a larger region, a 5 μm (FWHM) focus was created, centered on the position of the fiber bundle for detection (fluorescence recorded from a dilute fluorophore solution). (**B**) The 7-fiber 'single photon camera' detector elements. (**C**) Signals from a fluorescent bead are recorded on all seven channels as a function of position x, y (scanned area: 2x2 μm). (**D**) The sum of counts on all seven detectors varies smoothly over the recorded region, but (**E**) the ratios among detectors uniquely identify a given localization by its count pattern $\vec{R}(x,y) = (R_1(x,y) \ldots R_7(x,y)$ (the reference map). (**F**) Localization accuracy σ_r as a function of photons N employed in the localization is near-shot-noise-limited (determined by 5000 consecutive localizations of a stationary bead in the central region). These values imply a lower bound on the attainable localization accuracy and thus spatial resolution in the image for respective photon numbers in a typical emission event.(**G**) The map self-consistency check (see Chapter 2) shows that localization is reliable (no systematic errors) over the central near-elliptical region of about 500–600 nm.

(noise content only in detectors remote from the imaged lateral emitter position), this value is somewhat worse than for the molecule tracking configuration (Chapters 2 and 3), where we operate only in the region directly between three fibers ($\sigma_{vib,sys} < 2$ nm). Over the central region the setup therefore allows near-shot-noise-limited localization based on spatially resolved single-photon-counting.

Experimental details

Molecules within the 5 μm (FWHM) focus were subjected to blue ($\lambda = 491$ nm) light by a laser source (Calypso, Cobolt) at intensities of $\sim$15 kW/cm^2. This focus was concentric with fiber bundle for detection. TCSPC recording was performed as described in Chapter 2. Two methods for increasing the lifetime τ of the dark states beyond the millisecond range were applied in the present work: Oxygen reduction leads to long triplet lifetimes since oxygen serves as a triplet quencher. Therefore, aqueous media with addition of glucose, glucose-oxidase and catalase were used. Glucose-oxidase is an enzyme which uses glucose to bind oxygen, whereas catalase is an enzyme which decomposes the resulting toxic hydrogen peroxide. The second method was embedding the samples in poly-vinyl-alcohol (PVA). PVA constrains the oxygen diffusion, leading to a prolonged triplet lifetime, and furthermore introduces additional dark states [115]. Both media are standard microscopy mounting media.

For GSDIM nanoscopy, the microtubule network of whole fixed PtK2 cells was immunostained with Alexa488, a commercial dye. The mammalian PtK2 cell line was grown as described in [116]. The cells were then seeded and grown on standard glass coverslips to a confluency of about 50% and fixed with cold methanol for 4 min, followed by incubation in blocking buffer (Phosphate Buffered Saline (PBS) containing 1% Bovine Serum Albumin (BSA)). The microtubules were stained with anti-β-tubulin mouse IgG (Sigma-Aldrich, St. Louis, MO, USA) and the dye Alexa488 conjugated to sheep anti-mouse IgG (Sigma). Imaging of the immunostained cells was performed in PVA (spincoating of 1% PVA in PBS (pH 7.4) solution at 3000 rpm for 30s) or in standard aqueous imaging buffer (50 mM Tris, pH 7.5, 10 mM NaCl, 0.5 mg/mL glucose oxidase (G2133, Sigma), 40 g/mL catalase (106810, Roche Applied

Science) and 10% (w/v) glucose).

4.2.2 GSDIM imaging with tailored fluorescence burst selection

The localization capability is applied for fluorescence nanoscopy (Figure 4.3 and 4.4).

Photon data was recorded for several minutes on all seven detectors. One fiber had negligible transmission but was included in the signal analysis. From the combined photon trace over all seven detetors, individual fluorescence bursts could be identified – now corresponding not to diffusion transits (as in Chapters 2 and 3) but to on-phases of indivudal fluorophores (Figure 4.3A). A recording mode with a fixed integration time (e.g. a camera) cannot adequately match the duration of individual bursts and inevitably comprises periods devoid of molecular signal during a frame (a time bin) (Figure 4.3B). The single-photon-based burst selection can be limited to the photons stemming only from the time interval of the emission event (Figure 4.3C). Thus virtually none of the avoidable background periods are contained in a chosen time segment which produces a localization. Figure 4.4 shows examples of single-photon-counting GSDIM images (insets) of the tubulin network as compared to a quasi-confocal scan with one of the detection fibers. A resolution of $FWHM \approx 60$ nm is estimated from the shown line profiles, in accordance with the threshold on the photon number $N = 100$ employed, which should guarantee a localization accuracy of that order over the small central region. Images produced by localizing events from the same photon stream based on time bins of 5 ms and 10 ms, respectively, exhibit effectively the same width within errors (not shown). Frame times of 5 or 10 ms would be chosen for a camera recording to closely match the characteristic burst times ($\Delta t_{burst,ch} \approx 2.5$ ms extending to several milliseconds. More uncertainty should conceptually be introduced in individual localizations for the latter cases as a result of the unwanted background periods, slightly reducing the resolution in the images. The last presumption needs further testing, as background – while fairly substantial in the described recordings – is always present in microscopic applications and its partial eliminition for the photon window yielding molecular registrations should in

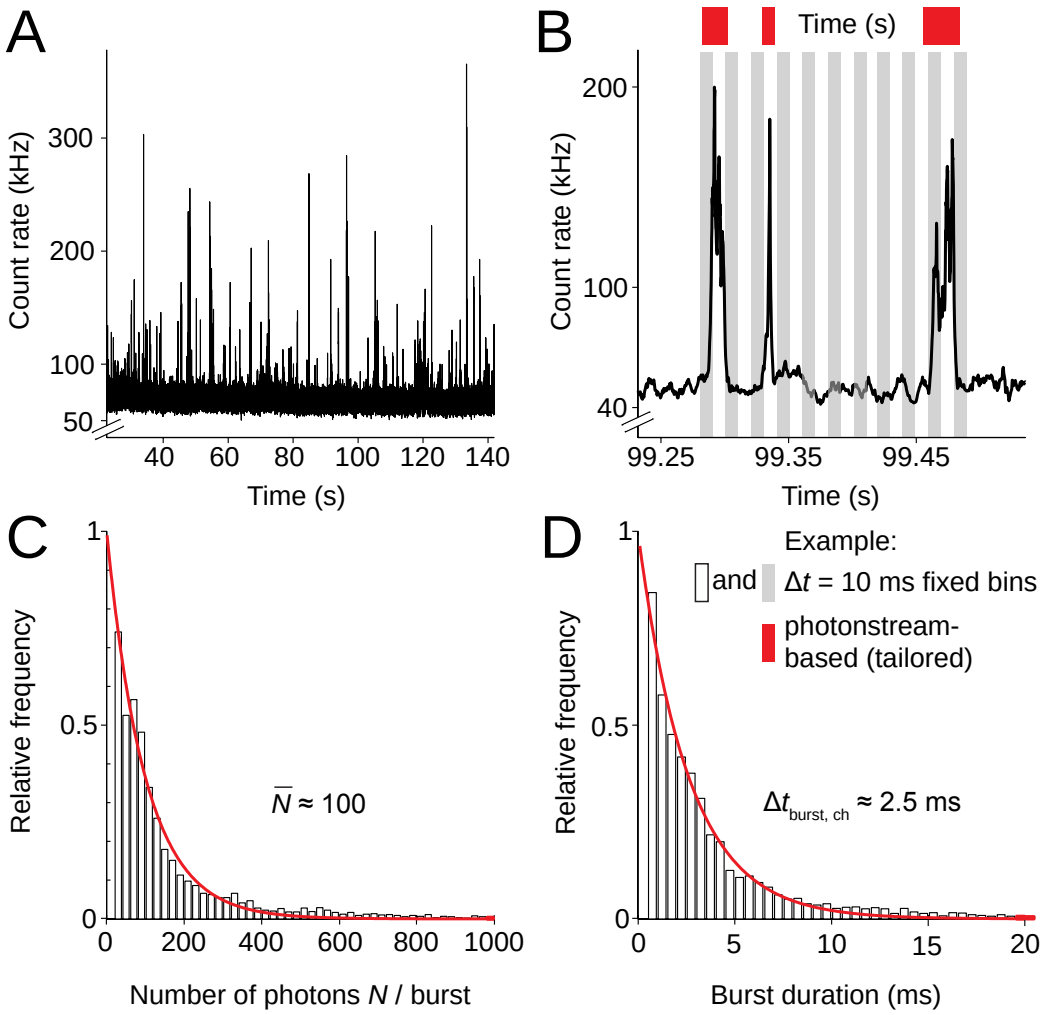

Figure 4.3: Assessment of the burst selection based on complete photon statistics (**A**) Count rate vs. time (photonbinned). Individual peaks in signal correspond to photon bursts of individual molecules in the on-state. They are rare enough so as not to overlap in time. (**B**) Fluorescence bursts of variable duration from individual emitting molecules can be accurately identified from a photon-binned intensity trace. Timebinning (shown at $\Delta t = 10$ ms) inevitably combines bursts occasionally (or cuts them in half) since the exact burst duration is a stochastic outcome and the bin intervals are fixed. (**C**) Distribution of photon number N / burst in a typical trace ($\bar{N} \approx 100$). (**D**) Distribution of burst durations (characteristic duration $\Delta t_{burst,ch} \approx$ 2.5 ms).

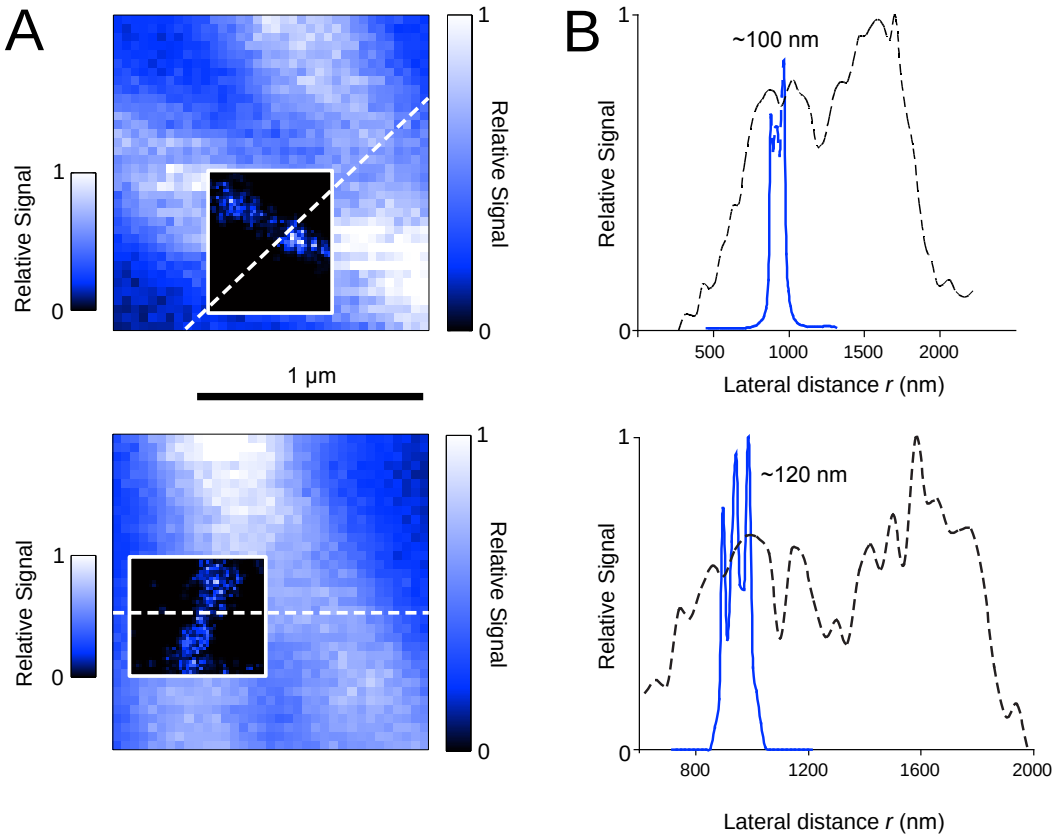

Figure 4.4: Examples of GSDIM nanoscopy with the 7-fiber single-photon camera (field of view 500–600 nm). The ratios among the seven detection channels uniquely determine each emitter's position, which is identified from each identified burst by comparing a 7-tupel of signals $(S_1 \dots S_7)$ to the calibration reference map $\{(R_1 \dots R_7)\}$ by a maximum likelihood estimator. (**A**) and(**B**) show examples of imaged portions of the microtubular network (β-tubulin) in whole fixed PtK2 cells, immunolabeled with Alexa488 antibody. Line profiles across strands suggest an image resolution of $\sim$ 60 nm in agreement with the photon cutoff of $N = 100$ photons (antibody-labeled microtubules are $\geq$60 nm in diameter). The confocal scan for comparison has a resolution of about 250 nm. The scale bar is 1000 nm.

principle benefit localization accuracy and image resolution.

Summary - Advantages of complete photon statistics for far-field fluorescence nanoscopy

The presented single-photon-counting approach to nanoscopy features:

- an accurate identification of a molecular emission event ('burst') based on the photon trace and avoids unwanted separation of one, or merging of several, event(s), which is presumed to lead to fewer mis-localizations and an improved localization estimate, because all relevant photons are harnessed.

- image resolution at conceptually its absolute limit for a given molecular signal of $\bar{N}$ photons, as was attempted to show by proof-of-principle experiments. The effect on resolution with a time-binned acquisition mode (camera) may be small depending on the signal-to-background ratio and details of the background distribution. But conceptually, a fixed frame rate can *never* do justice to the stochastic nature of the photon emission process and the concomitant distribution found in the duration of bursts. Even for exposure times that are well-matched to the average photon burst duration, there inevitably exist time-segments (idle or void periods) for many events for which unwanted background is acumulated and included in the signal to yield a molecule localization.

- A detection scheme employing full photon statistics and the nanosecond response-time of single-photon detectors should in the future enable imaging at much faster rates. At present however, the on-off switching dynamics of molecules are a limiting factor in the quest for faster nanoscopy by this stochastic read-out modality.

- at the expense of a small image size in this proof-of-principle experiment

Chapter 5

Conclusions and Outlook

5.1 Single molecules at the limit

The dynamical localization of individual fluorescent molecules in two dimensions with simultaneous high spatial localization accuracy ($\sigma_r = \ 10 - 20$nm) and temporal resolution ($\sim$0.5 ms) constitutes a substantial improvement in *in-vivo* single-molecule-tracking. A major factor contributing to the high spatio-temporal resolution of our tracking approach is the state-of-the-art single-photon detection and recording that allows us to adjust the spatial and temporal resolution. In addition, we envisage that the single-photon mode will give access to other spectroscopic parameters such as fluorescence lifetime (e.g., via time-correlated single-photon counting), color, or polarization anisotropy. This is different from conventional camera-based tracking approaches, whose time resolution is linked to the camera's frame rate and for which access to spectroscopic parameters is more difficult. Compared to the large field of view of a camera, our observation area is currently limited to $\sim$250 nm in diameter, also limiting the length of the trajectories observed. Yet, we collect many hundreds of single-molecule transits through the focal area in a single measurement. The potential of revisiting features of interest with matched spatio-temporal resolution was illustrated in this work by characterizing the spatial extent of molecular trapping with increased localization accuracy.

Our method offers flexibility when it comes to choosing appropriate spatial and

temporal accuracies to track the molecular motion of interest. Evidently, there are limits to achieving both equally well. When using groups of N photons from our photon stream to yield positions, the effective temporal resolution Δt, i.e., the time between two consecutive localizations, is given by $\Delta t \approx N/Q$. The localization is subject to a similar uncertainty of $\Delta A \approx A_{PSF}/N$, where A_{PSF} is the area of the detection PSF. It follows that

$$\Delta A \cdot \Delta t \approx \frac{A_{PSF}}{Q},$$

i.e., the product of spatial localization accuracy and temporal resolution, is roughly constant in the experiment. $\Delta A \cdot \Delta t$ varies slightly over the observation area as the count rate from the molecule is highest at the center of our excitation profile. It is interesting to note that similar considerations apply to single-molecule-switching-based far-field optical nanoscopy schemes. By choosing an appropriate N, it is thus possible to balance the spatial and the temporal accuracy as required.

Single-molecule tracking is inherently challenged by the fact that too large ΔA or Δt result in an averaging out of strongly confined and/or short trapping events [30]. Since the detection PSF (A_{PSF}) can hardly be reduced anymore, future improvements of the spatio-temporal resolution will mainly rely on higher detection rates Q. This can be achieved by brighter fluorophores (currently, Atto647N with $Q \leq 1$ MHz), as implemented in numerous single-particle tracking experiments by applying large signal markers [30, 46–49], and/or an increased collection efficiency afforded by one or two opposing objectives of high NA, such as provided by a 4Pi microscope [117]. Increasing Q by increasing the excitation power may be challenged by bleaching.

We highlight that our approach of using a localization reference map deals with point-like detectors in arbitrary relative configurations (the fibers need not be equidistant from each other). Arrays of more than three detectors may be used, covering a larger observation area, and axial (z) sensitivity could be achieved by a tetrahedral arrangement [45–47] or similar.

Effects of molecular orientation were not observed in this study. We cannot exclude them, but we anticipate that they should average out over the timescale of individual localizations (typically 0.5 ms) because of fast rotational diffusion in the

molecular environment given.

Applied to rapidly diffusing plasma membrane lipids in living cells, our single-molecule tracking method revealed transient trapping on the macromolecular scale ($r_{trap} < 10$ nm). This is in agreement with the reported confinement to 20 nm diameter regions observed by STED-FCS [89, 95]. Trapping of the sphingolipid SM is cholesterol-assisted and much more pronounced than that of the phosphoglycero-lipid PE. In contrast to PE, which exhibits a trapping for <30 % of the time, SM shows a deviation from free diffusion for about 70 % of the time. This difference mainly stems from the pronounced trapping duration of >15 ms for SM compared to <4 ms for PE. As for the previous STED-FCS measurements [89, 95], our findings support the notion that a single lipid interacts only locally with other membrane components, potentially by transiently forming complexes with membrane proteins. While the complex (of several lipid and protein molecules) of which the trapped lipid is part may (temporarily) be larger, our data indicates that the lipid itself dwells only within <20 nm diameter areas. External induction may amplify such domains [118].

The present method of quantifying molecular dynamics is complementary to STED-FCS [89, 95]. The direct access to the spatio-temporal information of single-molecule trajectories is essential to infer the location and the time of transient molecular complex formation. However, the association and dissociation rates of complex formation are more difficult to assess because most short-lived complexes cannot be untangled from normal Brownian motion. Conversely, STED-FCS measures these rates quite easily, especially because it allows the observation of anomalous lipid diffusion through nanoscale foci of variable size. As a method operating with molecular ensembles, STED-FCS certainly has a series of advantages such as its ease of use, its ability to deal with various experimental conditions, and its short acquisition time. Gaining information about individual complexes clearly is the realm of the present method. Studying the behavior of individual molecules means that there must not be more than a single molecule in the detection area at a given point in time. The experimental price to pay is the requirement of an adjusted label concentration and a longer acquisition time. Because the label concentration is about two orders of magnitude lower than with STED-FCS, the acquisition time (∼5–10 min) grows by about this

factor to achieve comparable reliability. The agreement between the single-molecule tracking and STED-FCS results is remarkable, because the two methods employ different methodology and operate under different parameter conditions. In particular, the single-molecule tracking experiments were performed at much lower light levels ($\sim$5–20 kW/cm^2) than are found for the STED irradiation (10–100 MW/cm^2). However, one must bear in mind that the low light levels are applied at a wavelength at which the dye absorbs light, whereas the more intense STED beam features a longer wavelength, i.e., a lower photon energy that is not really absorbed by the dye or the cell.

Fast molecular tracking at arbitrary label concentration

A challenging aspect in this tracking approach is that the experimenter must achieve single-molecule concentration of the label when preparing cells for measurement. Depending on the labeling strategy, this is often difficult to accomplish and requires patience. Because the uptake of label molecules by the membrane is a complicated process, large variation may also be seen among cells as to the exact concentration (surface density) attained. Employing photoswitchable probe molecules within this method to control the density of fluorescing entities could be helpful in this respect and enable the study of dynamics of individual molecules at comparatively high concentrations [44, 120–122]. Keeping the surface density of fluorescing molecules low by tuning apparent concentrations with a novel class of caged dyes [119] may be a successful avenue in this regard (see Figure 5.1).

5.2 Towards co-localization of molecular interaction events on the millisecond-timescale

In this thesis, we have demonstrated the potential of confocalized molecular tracking by spatially resolved single-photon-counting for the investigation of fast-diffusing molecules at nanometer length scales. Our scheme [123] beats previously reported tracking experiments of small-organic-dye or fluorescent-protein labelled objects by

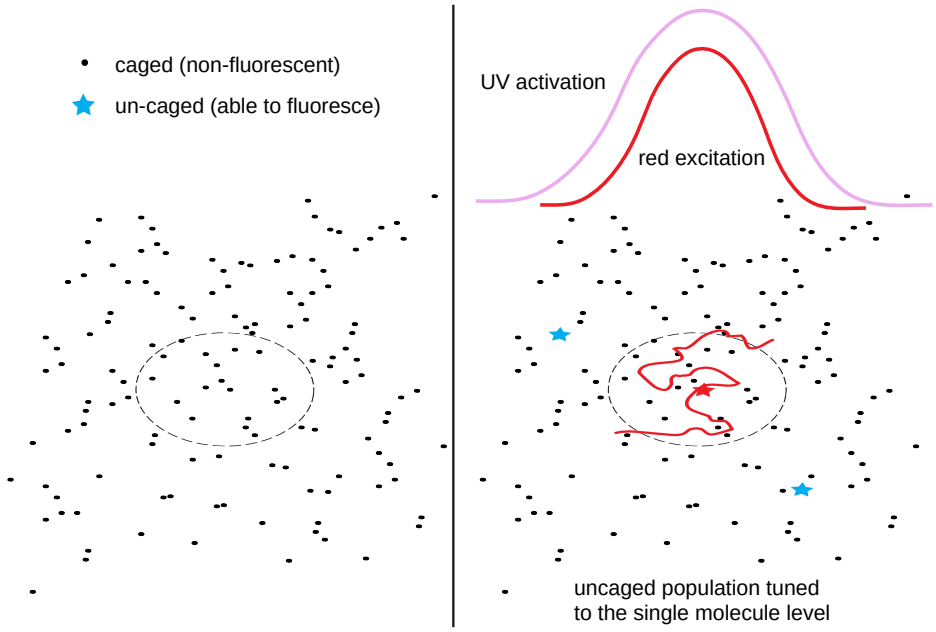

Figure 5.1: A novel class of caged rhodamine NN dyes [119] may provide quick and simple access to single-molecule concentrations that are a prerequisite in the present molecular tracking approach. Overlaying the excitation focus (red) with a somewhat enlarged spot of ultraviolet (UV) light could allow tuning of the portion of caged-dye-labeled lipid or protein analogs found in their uncaged state (i.e. a state capable of fluorescing). As the observation volume is an open volume, a number of molecules should be replenished from the periphery and already be uncaged (ready to fluoresce) in some instances when entering the excitation focus. The z position of the membrane is also identified more straightforwardly at elevated cocentration ahead of the actual tracking recording. The equilibrium population of uncaged labels is controlled by the intensity of UV light. An occasional pulse of UV may be sufficient to provide occasional uncaged single molecules.

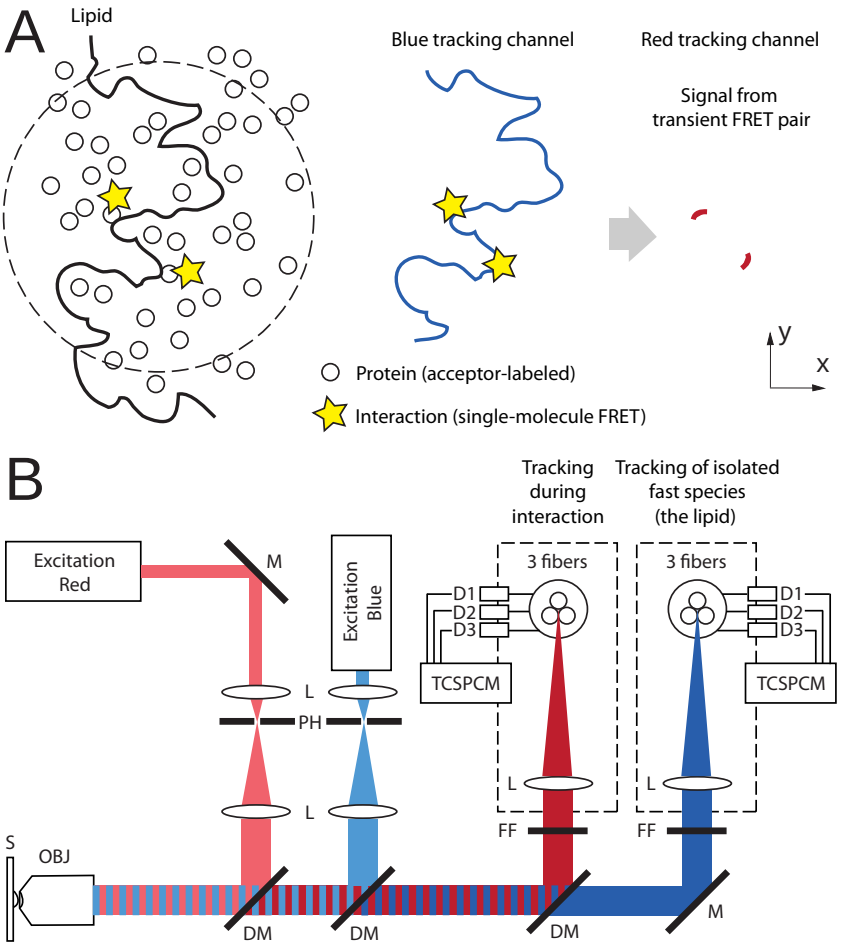

Figure 5.2: (**A**) Fast tracking in two color channels may directly visualize nanoscale molecular interactions. (**B**) Extension of the optical setup to two colors. Fluorescence is detected separately on two fiber bundles. One species (the faster diffusing one, the lipid) is tracked in the blue channel. If binding to a labelled interaction partner (a 'raft' candidate protein) occurs, energy is transferred non-radiatively by single-molecule Förster resonance energy transfer (sm-FRET) and the pair will be traceable in the other (red) color channel while bound. The scheme would, at the same time, directly prove both the close nature of the interaction (significant FRET occurs on very short lengthscales (sub-5 nm) and allow the systematic characterization of lipid-binding proteins. By separating orthogonal polarizations, this setup would also allow to monitor the fluorescence anisotropy during selected phases of the trajectory (such as nanoscale lateral confinement) at the single-molecule level. This could potentially reveal orientational fixing during intercations ('trapping').

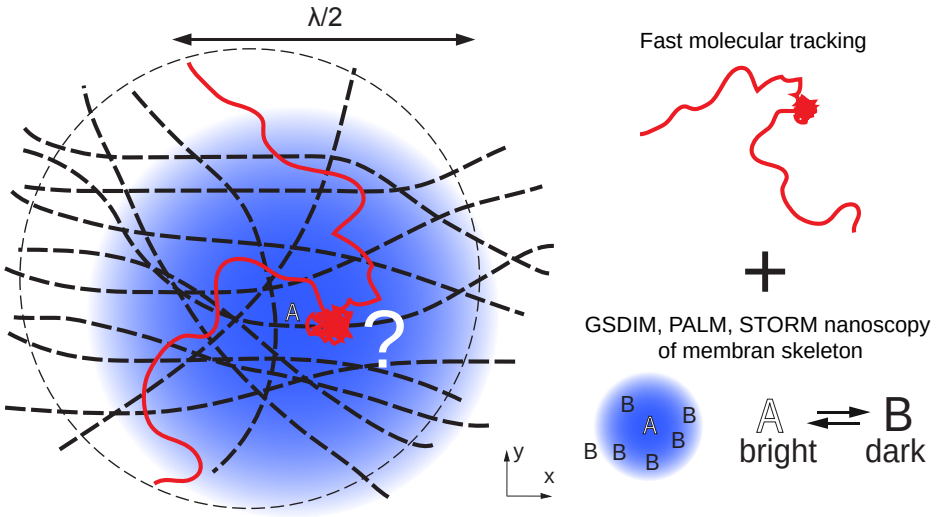

Figure 5.3: Nanoscopy paired with fast molecular tracking (schematic trajectory) could provide a structural context of trapping at the nanoscale. While one color channel records molecular trajectories, this spatiotemporal information could be correlated with nanoscale structural information about the cellular context (such as location of the membrane skeleton), generated in the other channel (by PALM, STORM, GSDIM nanoscopy etc).

an order of magnitude in temporal resolution while maintaining the high spatial localization accuracies of those experiments. Fast-diffusing single molecules were thus detected for the first time at this high time resolution and with very high sensitivity. This methodological advance has been recognized [124] and its discovery potential highlighted, especially for dynamical membrane processes occuring at the nanometer scale. An intriguing consequence of this work is that we envisage its extension to two- or multicolor observation. Thus it should be feasible not only to dissect the individual paths taken by a given molecular species but also the molecular context in which this occurs, that is to say, we could study specific interactions of molecules in their native and often highly dynamical environment (Figure 5.2 and Figure 5.3). Current views of membrane organization stress the need for experimental approaches to visualize both at the nansocale (spatially) and at fast timescales (temporally). STED-FCS was the first tool to combine both of these desired features. Fast molecular tracking – which has the advantage that access to spatiotemporal information is direct and would in principle require no further model assumptions – has been demonstrated to

be fully complementary for the biological problems already studied. In our laboratory, we currently take the view that an excellent assessment of the diffusion behavior can be gained with STED-FCS and points of interest re-assessed by tracking. The combination and careful interpretation of data from both methods have proven to be key for a deeper understanding.

Bibliography

[1] R. P. Feynman, *Miniaturization* (Reinhold Publishing Corporation, New York, 1961).

[2] E. Verdet, "Leçons d'optique physique," *Victor Masson et fils, Paris* (1869).

[3] E. Abbe, "Beiträge zur Theorie des Mikroskops und der mikroskopischen Wahrnehmung," *Arch Mikroskop Anat* **9**, 413 (1873).

[4] Lord Rayleigh, "On the theory of optical images, with special reference to the microscope," *Philos Mag* **XLII**, 167 (1896).

[5] S. W. Hell and J. Wichmann, "Breaking the diffraction resolution limit by stimulated emission: stimulated-emission-depletion fluorescence microscopy," *Opt Lett* **19**, 780 (1994).

[6] S. W. Hell and M. Kroug, "Ground-state-depletion fluorescence microscopy: a concept for breaking the diffraction resolution limit," *Appl Phys B* **60**, 495 (1995).

[7] T. A. Klar, S. Jakobs, M. Dyba, A. Egner, and S. W. Hell, "Fluorescence microscopy with diffraction resolution barrier broken by stimulated emission," *Proc Natl Acad Sci USA* **97**, 8206 (2000).

[8] S. W. Hell, "Toward fluorescence nanoscopy," *Nat Biotechnol* **21**, 1347 (2003).

[9] S. W. Hell, "Far-field optical nanoscopy," *Science* **316**, 1153 (2007).

[10] S. W. Hell, "Microscopy and its focal switch," *Nature Methods* **6**, 24 (2008).

[11] Moerner and Kador, "Optical detection and spectroscopy of single molecules in a solid.," *Phys Rev Lett* **62**, 2535 (1989).

[12] Orrit and Bernard, "Single pentacene molecules detected by fluorescence excitation in a p-terphenyl crystal," *Phys Rev Lett* **65**, 2716 (1990).

[13] E. B. Shera, N. K. Seitzinger, L. M. Davis, R. A. Keller, and S. A. Soper, "Detection of single fluorescent molecules," *Chem. Phys. Lett.* **174**, 553 (1990).

[14] R. M. Dickson, D. J. Norris, Y. L. Tzeng, and W. E. Moerner, "Three-dimensional imaging of single molecules solvated in pores of poly(acrylamide) gels," *Science* **274**, 966 (1996).

[15] T. Funatsu, Y. Harada, M. Tokunaga, K. Saito, and T. Yanagida, "Imaging of single fluorescent molecules and individual ATP turnovers by single myosin molecules in aqueous solution," *Nature* **374**, 555 (1995).

[16] P. Tinnefeld and M. Sauer, "Branching out of single-molecule fluorescence spectroscopy: challenges for chemistry and influence on biology.," *Angew Chem Int Ed Engl* **44**, 2642 (2005).

[17] W. J. Greenleaf, M. T. Woodside, and S. M. Block, "High-resolution, single-molecule measurements of biomolecular motion," *Annu Rev Biophys Biomol Struct* **36**, 171 (2007).

[18] M. A. Ditzler, E. A. Alemn, D. Rueda, and N. G. Walter, "Focus on function: single molecule RNA enzymology," *Biopolymers* **87**, 302 (2007).

[19] W. E. Moerner, "New directions in single-molecule imaging and analysis," *Proc Natl Acad Sci USA* **104**, 12596 (2007).

[20] P. R. Selvin and T. Ha, editors, *Single-Molecule Techniques: A Laboratory Manual* (Cold Spring Harbor Laboratory Press, Cold Spring Harbor, New York, 2008).

[21] J. R. Moffitt, Y. R. Chemla, S. B. Smith, and C. Bustamante, "Recent advances in optical tweezers," *Annu Rev Biochem* **77**, 205 (2008).

[22] K. C. Neuman and A. Nagy, "Single-molecule force spectroscopy: optical tweezers, magnetic tweezers and atomic force microscopy," *Nature Methods* **5**, 491 (2008).

[23] R. Roy, S. Hohng, and T. Ha, "A practical guide to single-molecule FRET," *Nature Methods* **5**, 507 (2008).

[24] A. Pertsinidis, Y. Zhang, and S. Chu, "Subnanometre single-molecule localization, registration and distance measurements.," *Nature* **466**, 647 (2010).

[25] H. Geerts, M. D. Brabander, R. Nuydens, S. Geuens, M. Moeremans, J. D. Mey, and P. Hollenbeck, "Nanovid tracking: a new automatic method for the study of mobility in living cells based on colloidal gold and video microscopy," *Biophys J* **52**, 775 (1987).

[26] J. Gelles, B. J. Schnapp, and M. P. Sheetz, "Tracking kinesin-driven movements with nanometre-scale precision," *Nature* **331**, 450 (1988).

[27] D. A. Schafer, J. Gelles, M. P. Sheetz, and R. Landick, "Transcription by single molecules of RNA polymerase observed by light microscopy," *Nature* **352**, 444 (1991).

[28] T. Schmidt, G. J. Schütz, W. Baumgartner, H. J. Gruber, and H. Schindler, "Imaging of single molecule diffusion," *Proc Natl Acad Sci USA* **93**, 2926 (1996).

[29] M. P. Sheetz, S. Turney, H. Qian, and E. L. Elson, "Nanometre-level analysis demonstrates that lipid flow does not drive membrane glycoprotein movements," *Nature* **340**, 284 (1989).

[30] T. Fujiwara, K. Ritchie, H. Murakoshi, K. Jacobson, and A. Kusumi, "Phospholipids undergo hop diffusion in compartmentalized cell membrane," *J Cell Biol* **157**, 1071 (2002).

[31] G. M. Lee, A. Ishihara, and K. A. Jacobson, "Direct observation of brownian motion of lipids in a membrane," *Proc Natl Acad Sci USA* **88**, 6274 (1991).

[32] W. E. Moerner and M. Orrit, "Illuminating single molecules in condensed matter," *Science* **283**, 1670 (1999).

[33] W. P. Ambrose, P. M. Goodwin, J. H. Jett, A. V. Orden, J. H. Werner, and R. A. Keller, "Single molecule fluorescence spectroscopy at ambient temperature," *Chem Rev* **99**, 2929 (1999).

[34] X. S. Xie and J. K. Trautman, "Optical studies of single molecules at room temperature," *Annu Rev Phys Chem* **49**, 441 (1998).

[35] C. Joo, H. Balci, Y. Ishitsuka, C. Buranachai, and T. Ha, "Advances in single-molecule fluorescence methods for molecular biology," *Annu Rev Biochem* **77**, 51 (2008).

[36] M. Minsky, "Microscopy apparatus," *US Patent* , 3,013,467 (1961).

[37] W. Heisenberg, *The physical principles of the quantum theory* (Chicago Univ Press, Chicago, 1930).

[38] R. E. Thompson, D. R. Larson, and W. W. Webb, "Precise nanometer localization analysis for individual fluorescent probes," *Biophys J* **82**, 2775 (2002).

[39] A. Yildiz, J. N. Forkey, S. A. McKinney, T. Ha, Y. E. Goldman, and P. R. Selvin, "Myosin V walks hand-over-hand: single fluorophore imaging with 1.5-nm localization," *Science* **300**, 2061 (2003).

[40] E. Toprak and P. R. Selvin, "New fluorescent tools for watching nanometer-scale conformational changes of single molecules," *Annu Rev Biophys Biomol Struct* **36**, 349 (2007).

[41] H. Park, E. Toprak, and P. R. Selvin, "Single-molecule fluorescence to study molecular motors," *Q Rev Biophys* **40**, 87 (2007).

[42] J. R. Lakowicz, *Principles of Fluorescence Spectroscopy*, 3rd edn. ed. (Springer, New York, 2006).

[43] T.-H. Lee, L. J. Lapidus, W. Zhao, K. J. Travers, D. Herschlag, and S. Chu, "Measuring the folding transition time of single RNA molecules," *Biophys J* **92**, 3275 (2007).

[44] S. W. Hell, "German Patent No DE102006021317B3," (2006).

[45] G. A. Lessard, P. M. Goodwin, and J. H. Werner, "Three-dimensional tracking of fluorescent particles," *Proc SPIE* **6092**, 609205 (1 (2006).

[46] G. A. Lessard, P. M. Goodwin, and J. H. Werner, "Three-dimensional tracking of individual quantum dots," *Appl Phys Lett* **91**, 224106 (2007).

[47] N. P. Wells, G. A. Lessard, and J. H. Werner, "Confocal, three-dimensional tracking of individual quantum dots in high-background environments," *Anal Chem* **80**, 9830 (2008).

[48] C. Hellriegel and E. Gratton, "Real-time multi-parameter spectroscopy and localization in three-dimensional single-particle tracking," *J R Soc Interface* **6**, Suppl 1 S3 (2009).

[49] K. McHale, A. J. Berglund, and H. Mabuchi, "Quantum dot photon statistics measured by three-dimensional particle tracking," *Nano Lett* **7**, 3535 (2007).

[50] M. Leutenegger, R. Rao, R. A. Leitgeb, and T. Lasser, "Fast focus field calculations.," *Opt Express* **14**, 11277 (2006).

[51] D. S. Martin, M. B. Forstner, and J. A. Käs, "Apparent subdiffusion inherent to single particle tracking," *Biophys J* **83**, 2109 (2002).

[52] T. Savin and P. S. Doyle, "Static and dynamic errors in particle tracking microrheology," *Biophys J* **88**, 623 (2005).

[53] K. Simons and E. Ikonen, "Functional rafts in cell membranes," *Nature* **387**, 569 (1997).

[54] D. A. Brown and E. London, "Structure and function of sphingolipid- and cholesterol-rich membrane rafts," *J Biol Chem* **275**, 17221 (2000).

[55] C. J. Fielding, *Lipid Rafts and Caveolae* (Wiley-VCH, Weinheim, Germany, 2006).

[56] K. Jacobson, O. G. Mouritsen, and R. G. W. Anderson, "Lipid rafts: at a crossroad between cell biology and physics," *Nat Cell Biol* **9**, 7 (2007).

[57] M. F. Hanzal-Bayer and J. F. Hancock, "Lipid rafts and membrane traffic," *FEBS Lett* **581**, 2098 (2007).

[58] S. Munro, "Lipid rafts: elusive or illusive?," *Cell* **115**, 377 (2003).

[59] P. H. M. Lommerse, H. P. Spaink, and T. Schmidt, "In vivo plasma membrane organization: results of biophysical approaches," *Biochim Biophys Acta* **1664**, 119 (2004).

[60] J. F. Hancock, "Lipid rafts: contentious only from simplistic standpoints," *Nat Rev Mol Cell Biol* **7**, 456 (2006).

[61] A. S. Shaw, "Lipid rafts: now you see them, now you don't," *Nat Immunol* **7**, 1139 (2006).

[62] L. J. Pike, "Rafts defined: a report on the Keystone Symposium on Lipid Rafts and Cell Function," *J Lipid Res* **47**, 1597 (2006).

[63] G. J. Schütz, G. Kada, V. P. Pastushenko, and H. Schindler, "Properties of lipid microdomains in a muscle cell membrane visualized by single molecule microscopy," *EMBO J* **19**, 892 (2000).

[64] M. Vrljic, S. Y. Nishimura, W. E. Moerner, and H. M. McConnell, "Cholesterol depletion suppresses the translational diffusion of class II major histocompatibility complex proteins in the plasma membrane," *Biophys J* **88**, 334 (2005).

[65] J. C. Holthuis, T. Pomorski, R. J. Raggers, H. Sprong, and G. V. Meer, "The organizing potential of sphingolipids in intracellular membrane transport," *Physiol Rev* **81**, 1689 (2001).

[66] I. Pascher, "Molecular arrangements in sphingolipids. Conformation and hydrogen bonding of ceramide and their implication on membrane stability and permeability," *Biochim Biophys Acta* **455**, 433 (1976).

[67] G. van Meer, "Lipid traffic in animal cells," *Annu Rev Cell Biol* **5**, 247 (1989).

[68] Y. Lange, M. H. Swaisgood, B. V. Ramos, and T. L. Steck, "Plasma membranes contain half the phospholipid and 90cholesterol and sphingomyelin in cultured human fibroblasts.," *J Biol Chem* **264**, 3786 (1989).

[69] K. Simons and G. van Meer, "Lipid sorting in epithelial cells," *Biochemistry* **27**, 6197 (1988).

[70] M. S. Bretscher, "Membrane structure: some general principles," *Science* **181**, 622 (1973).

[71] K. Balasubramanian and A. J. Schroit, "Aminophospholipid asymmetry: A matter of life and death," *Annu Rev Physiol* **65**, 701 (2003).

[72] P. Müller and A. Herrmann, "Rapid transbilayer movement of spin-labeled steroids in human erythrocytes and in liposomes," *Biophys J* **82**, 1418 (2002).

[73] T. E. Thompson and T. W. Tillack, "Organization of glycosphingolipids in bilayers and plasma membranes of mammalian cells," *Annu Rev Biophys Biophys Chem* **14**, 361 (1985).

[74] P. Sharma, R. Varma, R. C. Sarasij, Ira, K. Gousset, G. Krishnamoorthy, M. Rao, and S. Mayor, "Nanoscale organization of multiple GPI-anchored proteins in living cell membranes," *Cell* **116**, 577 (2004).

[75] D. Lingwood and K. Simons, "Lipid rafts as a membrane-organizing principle," *Science* **327**, 46 (2010).

[76] C. Dietrich, L. A. Bagatolli, Z. N. Volovyk, N. L. Thompson, M. Levi, K. Jacobson, and E. Gratton, "Lipid rafts reconstituted in model membranes," *Biophys J* **80**, 1417 (2001).

[77] M. Edidin, "The state of lipid rafts: from model membranes to cells," *Annu Rev Biophys Biomol Struct* **32**, 257 (2003).

[78] H. Heerklotz, "Triton promotes domain formation in lipid raft mixtures," *Biophys J* **83**, 2693 (2002).

[79] K. Bacia, D. Scherfeld, N. Kahya, and P. Schwille, "Fluorescence correlation spectroscopy relates rafts in model and native membranes," *Biophys J* **87**, 1034 (2004).

[80] J. L. Thewalt and M. Bloom, "Phosphatidylcholine: cholesterol phase diagrams," *Biophys J* **63**, 1176 (1992).

[81] R. F. M. de Almeida, L. M. S. Loura, A. Fedorov, and M. Prieto, "Lipid rafts have different sizes depending on membrane composition: a time-resolved fluorescence resonance energy transfer study," *J Mol Biol* **346**, 1109 (2005).

[82] Y.-W. Hsueh, K. Gilbert, C. Trandum, M. Zuckermann, and J. Thewalt, "The effect of ergosterol on dipalmitoylphosphatidylcholine bilayers: a deuterium NMR and calorimetric study," *Biophys J* **88**, 1799 (2005).

[83] A. Yethiraj and J. C. Weisshaar, "Why are lipid rafts not observed in vivo?," *Biophys J* **93**, 3113 (2007).

[84] L. Wawrezinieck, H. Rigneault, D. Marguet, and P.-F. Lenne, "Fluorescence correlation spectroscopy diffusion laws to probe the submicron cell membrane organization," *Biophys J* **89**, 4029 (2005).

[85] D. A. Zacharias, J. D. Violin, A. C. Newton, and R. Y. Tsien, "Partitioning of lipid-modified monomeric GFPs into membrane microdomains of live cells," *Science* **296**, 913 (2002).

[86] T. J. Feder, I. Brust-Mascher, J. P. Slattery, B. Baird, and W. W. Webb, "Constrained diffusion or immobile fraction on cell surfaces: a new interpretation," *Biophys J* **70**, 2767 (1996).

[87] E. Yechiel and M. Edidin, "Micrometer-scale domains in fibroblast plasma membranes," *J Cell Biol* **105**, 755 (1987).

[88] R. G. W. Anderson and K. Jacobson, "A role for lipid shells in targeting proteins to caveolae, rafts, and other lipid domains," *Science* **296**, 1821 (2002).

[89] C. Eggeling, C. Ringemann, R. Medda, G. Schwarzmann, K. Sandhoff, S. Polyakova, V. N. Belov, B. Hein, C. von Middendorff, A. Schönle, and S. W. Hell, "Direct observation of the nanoscale dynamics of membrane lipids in a living cell," *Nature* **457**, 1159 (2009).

[90] D. Magde, E. Elson, and W. W. Webb, "Thermodynamic fluctuations in a reacting system – Measurement by fluorescence correlation spectroscopy," *Phys Rev Lett* **29**, 705 (1972).

[91] J. R. Fries, L. Brand, C. Eggeling, M. Kollner, and C. A. M. Seidel, "Quantitative identification of different single molecules by selective time-resolved confocal fluorescence spectroscopy," *J Phys Chem A* **102**, 6601 (1998).

[92] P. Kask, K. Palo, D. Ullmann, and K. Gall, "Fluorescence-intensity distribution analysis and its application in biomolecular detection technology," *Proc Natl Acad Sci USA* **96**, 13756 (1999).

[93] D. E. Koppel, "Statistical accuracy in fluorescence correlation spectroscopy," *Phys Rev A* **10**, 1938 (1974).

[94] S. Chiantia, J. Ries, N. Kahya, and P. Schwille, "Combined AFM and two-focus SFCS study of raft-exhibiting model membranes," *ChemPhysChem* **7**, 2409 (2006).

[95] C. Ringemann, B. Harke, C. v. Middendorff, R. Medda, A. Honigmann, R. Wagner, M. Leutenegger, A. Schönle, S. W. Hell, and C. Eggeling, "Exploring single-molecule dynamics with fluorescence nanoscopy," *New J Phys* **11**, 103054 (2009).

[96] G. J. Schütz, H. Schindler, and T. Schmidt, "Single-molecule microscopy on model membranes reveals anomalous diffusion," *Biophys J* **73**, 1073 (1997).

[97] F. Pinaud, X. Michalet, G. Iyer, E. Margeat, H.-P. Moore, and S. Weiss, "Dynamic partitioning of a glycosyl-phosphatidylinositol-anchored protein in glycosphingolipid-rich microdomains imaged by single-quantum dot tracking," *Traffic* **10**, 691 (2009).

[98] R. Simson, E. D. Sheets, and K. Jacobson, "Detection of temporary lateral confinement of membrane proteins using single-particle tracking analysis," *Biophys J* **69**, 989 (1995).

[99] P. Schwille, J. Korlach, and W. W. Webb, "Fluorescence correlation spectroscopy with single-molecule sensitivity on cell and model membranes," *Cytometry* **36**, 176 (1999).

[100] G. Donnert, J. Keller, R. Medda, M. A. Andrei, S. O. Rizzoli, R. Lührmann, R. Jahn, C. Eggeling, and S. W. Hell, "Macromolecular-scale resolution in biological fluorescence microscopy," *Proc Natl Acad Sci USA* **103**, 11440 (2006).

[101] A. Kusumi, Y. M. Shirai, I. Koyama-Honda, K. G. N. Suzuki, and T. K. Fujiwara, "Hierarchical organization of the plasma membrane: investigations by single-molecule tracking vs. fluorescence correlation spectroscopy.," *FEBS Lett* **584**, 1814 (2010).

[102] J. G. Powles, M. J. D. Mallett, G. Rickayzen, and W. A. B. Evans, "Exact analytic solutions for diffusion impeded by an infinite array of partially permeable barriers," *Proc R Soc London* **436**, 391 (1992).

[103] S. Wieser, M. Moertelmaier, E. Fuertbauer, H. Stockinger, and G. J. Schtz, "(Un)confined diffusion of CD59 in the plasma membrane determined by high-resolution single molecule microscopy.," *Biophys J* **92**, 3719 (2007).

[104] E. Betzig, G. H. Patterson, R. Sougrat, O. W. Lindwasser, S. Olenych, J. S. Bonifacino, M. W. Davidson, J. Lippincott-Schwartz, and H. F. Hess, "Imaging intracellular fluorescent proteins at nanometer resolution," *Science* **313**, 1642 (2006).

[105] S. T. Hess, T. P. Girirajan, and M. D. Mason, "Ultra-high resolution imaging by fluorescence photoactivation localization microscopy," *Biophys J* **91**, 4258 (2006).

[106] M. J. Rust, M. Bates, and X. Zhuang, "Sub-diffraction-limit imaging by stochastic optical reconstruction microscopy (STORM)," *Nature Methods* **3**, 793 (2006).

[107] H. Bock, C. Geisler, C. A. Wurm, C. Von Middendorff, S. Jakobs, A. Schonle, A. Egner, S. W. Hell, and C. Eggeling, "Two-color far-field fluorescence nanoscopy based on photoswitchable emitters," *Appl Phys B* **88**, 161 (2007).

[108] M. Heilemann, S. van de Linde, M. Schttpelz, R. Kasper, B. Seefeldt, A. Mukherjee, P. Tinnefeld, and M. Sauer, "Subdiffraction-resolution fluorescence imaging with conventional fluorescent probes.," *Angew Chem Int Ed Engl* **47**, 6172 (2008).

[109] J. Fölling, V. Belov, R. Kunetsky, R. Medda, A. Schönle, A. Egner, C. Eggeling, M. Bossi, and S. W. Hell, "Photochromic rhodamines provide nanoscopy with optical sectioning," *Angew Chem Int Ed Engl* **46**, 6266 (2007).

[110] J. Fölling, M. Bossi, H. Bock, R. Medda, C. A. Wurm, B. Hein, S. Jakobs, C. Eggeling, and S. W. Hell, "Fluorescence nanoscopy by ground-state depletion and single-molecule return," *Nature Methods* **5**, 943 (2008).

[111] S. Bretschneider, C. Eggeling, and S. W. Hell, "Breaking the diffraction barrier in fluorescence microscopy by optical shelving," *Phys Rev Lett* **98**, 218103 (2007).

[112] E. Rittweger, D. Wildanger, and S. W. Hell, "Far-field fluorescence nanoscopy of diamond color centers by ground state depletion," *EPL* **86**, 14001 (2009).

[113] J. Bierwagen, "Charakterisierung von Fluoreszenzfarbstoffen für die ultrahochauflösende Weitfeld-Mikroskopie (Diploma Thesis)," (2009).

[114] J. Fölling, V. Belov, D. Riedel, A. Schönle, A. Egner, C. Eggeling, M. Bossi, and S. W. Hell, "Fluorescence nanoscopy with optical sectioning by two-photon induced molecular switching using continuous-wave lasers," *ChemPhysChem* **9**, 321 (2008).

[115] R. Zondervan, F. Kulzer, S. B. Orlinskii, and M. Orrit, "Photoblinking of Rhodamine 6G in Poly(vinyl alcohol): Radical Dark State Formed through the Triplet," *J Phys Chem A* **107**, 6770 (2003).

[116] K. Weber, T. Bibring, and M. Osborn, "Specific visualization of tubulin-containing structures in tissue culture cells by immunofluorescence. Cytoplasmic microtubules, vinblastine-induced paracrystals, and mitotic figures.," *Exp Cell Res* **95**, 111 (1975).

[117] S. W. Hell and E. H. K. Stelzer, "Properties of a 4Pi-confocal fluorescence microscope," *J Opt Soc Am A* **9**, 2159 (1992).

[118] D. Lingwood, J. Ries, P. Schwille, and K. Simons, "Plasma membranes are poised for activation of raft phase coalescence at physiological temperature," *Proc Natl Acad Sci USA* **105**, 10005 (2008).

[119] V. N. Belov, C. A. Wurm, V. P. Boyarskiy, S. Jakobs, and S. W. Hell, "Rhodamines NN: a novel class of caged fluorescent dyes.," *Angew Chem Int Ed Engl* **49**, 3520 (2010).

[120] C. Eggeling, M. Hilbert, H. Bock, C. Ringemann, M. Hofmann, A. C. Stiel, M. Andresen, S. Jakobs, A. Egner, A. Schönle, and S. W. Hell, "Reversible photoswitching enables single-molecule fluorescence fluctuation spectroscopy at high molecular concentration," *Microsc Res Tech* **70**, 1003 (2007).

[121] S. T. Hess, T. J. Gould, M. V. Gudheti, S. A. Maas, K. D. Mills, and J. Zimmerberg, "Dynamic clustered distribution of hemagglutinin resolved at 40 nm in living cell membranes discriminates between raft theories," *Proc Natl Acad Sci USA* **104**, 17370 (2007).

[122] S. Manley, J. M. Gillette, G. H. Patterson, H. Shroff, H. F. Hess, E. Betzig, and J. Lippincott-Schwartz, "High-density mapping of single-molecule trajectories with photoactivated localization microscopy," *Nature Methods* **5**, 155 (2008).

[123] S. J. Sahl, M. Leutenegger, M. Hilbert, S. W. Hell, and C. Eggeling, "Fast molecular tracking maps nanoscale dynamics of plasma membrane lipids," *Proc Natl Acad Sci USA* **107**, 6829 (2010).

[124] N. de Souza, "Watching single lipids move (Research Highlight)," *Nature Methods* **7**, 428 (2010).

Scientific contributions

Parts of this thesis have been or will be published as follows

1. S.J. Sahl, M. Leutenegger, M. Hilbert, S.W. Hell, and C. Eggeling. Fast molecular tracking maps nanoscale dynamics of plasma membrane lipids. *Proc. Natl. Acad. Sci. USA* 107(15): 6829-6834 (2010)

2. S.J. Sahl, M. Leutenegger, S.W. Hell, and C. Eggeling. Single molecule tracking by continuous fluorescence photon read-out: aspects of the method (in preparation)

Further research articles and an invited review article will describe a number of recent results obtained with the fast molecular tracking method.

Talks given at international conferences

1. S.J. Sahl, M. Leutenegger, C. Ringemann, V. Mueller, M. Hilbert, S.W. Hell, and C. Eggeling. STED nanoscopy and single molecule tracking map the nanoscale dynamics of plasma membrane lipids. *BiOS Symposium, SPIE Photonics West, San Francisco, CA, USA* (24 January 2010) *Young Investigator Award, Single Molecule Imaging and Spectroscopy Conference

2. S.J. Sahl, M. Leutenegger, M. Hilbert, C. Eggeling, and S.W. Hell. Single molecule tracking by spatially resolved single photon counting as a tool for far-field optical nanoscopy. *BiOS Symposium, SPIE Photonics West, San Francisco, CA, USA* (26 January 2010)

3. S.J. Sahl, M. Leutenegger, M. Hilbert, S.W. Hell, and C. Eggeling. Nanoscale lateral dynamics of single molecules by counting single photons with spatial distinction. *15th International Workshop on Single Molecule Spectroscopy and Ultrasensitive Analysis in the Life Sciences, Berlin Adlershof, Germany* (16 September 2009)

Poster Presentations

1. S.J. Sahl, M. Leutenegger, M. Hilbert, S.W. Hell, and C. Eggeling. Following lipid membrane dynamics by spatially resolved single photon counting. *Annual meeting of the German Biophysical Society 2010* (4 October 2010)

2. S.J. Sahl, M. Leutenegger, M. Hilbert, S.W. Hell, and C. Eggeling. Following lipid membrane dynamics by spatially resolved single photon counting. *16th International Workshop on Single Molecule Spectroscopy and Ultrasensitive Analysis in the Life Sciences, Berlin Adlershof, Germany* (16 September 2010)

Acknowledgments

This thesis was carried out in the Department of NanoBiophotonics at the Max Planck Institute for Biophysical Chemistry, Göttingen. I would like to extend my thanks to everyone who has directly or indirectly contributed to the success of this thesis.

First of all, I would like to thank Prof. Dr. Dr. h.c. Stefan W. Hell for the opportunity to perform research in an outstanding and highly motivating scientific environment. He not only offered the fascinating and challenging project of pushing the observation of single fluorescent molecules to its limits. His continuous interest and inspiring support in the project have significantly contributed to the success of this work.

I would like to thank Prof. Dr. Dirk Dubbers (Physikalisches Institut, Ruprecht-Karls-Universität Heidelberg) for his interest in my work and his willingness to be the second referee of my thesis.

The study of single molecules in biological membranes of living cells by optical methods is an interdisciplinary effort. It would not be possible without the expertise and dedication of other members of our Department and collaborators.

- I am very grateful to Dr. Christian Eggeling. Without his continuous support and help this work would not have been possible, and I always have greatly appreciated the collaborative spirit of our scientific discussions. Christian has been largely responsible in our Department for the recent research effort in nanoscale membrane dynamics using STED-FCS and, with his experience in the field, has been an excellent mentor on all aspects of single molecule spectroscopy.

- I am also extremely fortunate to have had Dr. Marcel Leutenegger collaborating on the project, who is always prepared and happy to share his great insight into all questions of fluorescence, optics, electronics and computer science, to name but a few. I have learned a great deal from Marcel. I further specifically acknowledge his kind contributions of analysis and simulation programs (Chapter 3), which were implemented with a keen eye for possible improvements in calculation speed.

My thanks also to

- Veronika Mueller and Dr. Christian Ringemann for stimulating discussions on our biological system and experimental approaches to it

- Tanja Gilat and Dr. Ellen Rothermel for technical assistance with cell culture

- Jens Ehrig and Prof. Dr. Petra Schwille (TU Dresden) for advice on supported lipid bilayer creation

- Dr. Rebecca Medda for a lot of discussions on biology and much more, and for teaching me how to be a 'biologist' myself

- Dr. Fabien Pinaud (Laboratoire Kastler Brossel, Ecole normale supérieure, Paris) for discussions on single particle tracking
- Dr. Günter Schwarzmann (Kekulé-Institut für Organische Chemie und Biochemie, Bonn) for fruitful discussions pertaining to lipid membrane insertion
- Daniel Aquino, Jakob Bierwagen and Dr. Claudia Geisler for helpful discussions on GSDIM imaging
- Dr. Birka Hein for help in the labeling of the GPI anchor
- Dr. Michael Hilbert for important preliminary experiments leading to this project
- Dr. Andreas Schönle for providing his software 'Imspector'
- the mechanical and optical workshop for their services
- Jaydev Jethwa and Harald Meyer for their technical assistance and helpful advice
- all other members of the Department for providing a really nice and comfortable working atmosphere
- Sarah Aschemann, Josephine Stadler and Alena Stephan for their friendly help with various kinds of organisational issues
- Dr. Marcel Leutenegger and Dr. Christian Eggeling for proof-reading parts of this thesis
- Veronika Mueller, Dr. Giuseppe Vicidomini and Dr. Mark Bates for special encouragement when it was most needed

I am grateful for funding of this work by the Max Planck Society and the Deutsche Forschungsgemeinschaft (through a Leibniz Prize to S.W.H.).

At the end of my formal education in the natural sciences, I would like to say my thanks to all my teachers of physics during school and university for showing me that science is a very worthwhile undertaking and for always encouraging me – especially among them: Jürgen Reiner and Hans Dietrich (Theodor-Heuss-Gymnasium Aalen), Frank Norton (Cranbrook Kingswood Upper School, Bloomfield Hills, MI, USA), Dr. David Hasko, Prof. Richard Phillips, Prof. Dame Athene Donald FRS, Prof. Peter Littlewood FRS, Prof. Tony Bland (†) and Prof. Sir Michael Pepper FRS (all of the Cavendish Laboratory, University of Cambridge).

Finally, I would like to thank my parents and my brother, my girlfriend and all other friends in Göttingen and elsewhere for their love and constant support.

Göttingen, 12$^{\text{th}}$ of September, 2010